Improving Electromagnetic Shielding with Metallic Nanoparticles

Mohsen Jalali

A Thesis
In the Department
of
Mechanical and Industrial Engineering

Presented in Partial Fulfillment of the Requirements
For the Degree of
Doctor of Philosophy (Mechanical and Industrial Engineering) at
Concordia University
Montreal, Quebec, Canada

June 2013

CONCORDIA UNIVERSITY
SCHOOL OF GRADUATE STUDIES

This is to certify that the thesis prepared

Entitled: **Improving Electromagnetic Shielding with Metallic Nanoparticles**

and submitted in partial fulfillment of the requirements for the degree of

DOCTOR OF PHILOSOPHY (Mechanical Engineering)

complies with the regulations of the University and meets the accepted standards with respect to originality and quality.

Signed by the final examining committee:

_____Chair
Prof. A. Kishk

_____External Examiner
Prof. F. Rachidi

_____External to Program
Prof. R. Paknys

_____Examiner
Prof. M. Medraj

_____Examiner
Prof. M. Paraschivoiu

_____Thesis Supervisor
Dr. R. Wuthrich

Approved by
Dr. A. Dolatabadi, Graduate Program Director

June 28, 2013 _____
Prof. C. Trueman, Dean
Faculty of Engineering & Computer Science

ABSTRACT

Improving Electromagnetic Shielding with Metallic Nanoparticles

Mohsen Jalali

For the Degree of Doctor of Philosophy (Mechanical and Industrial Engineering) at Concordia University, June 2013

Due to major advantages (e.g. weight saving, maintenance advantages), the airframe manufacturers use more and more Polymer Matrix Composites (PMCs) in different parts of aircraft structures. But PMCs have the substantial disadvantage of low conductivity and therefore low Electromagnetic (EM) Shielding. Electromagnetic Interference (EMI) sources are all around and inside aircraft and can potentially threaten the immunity of the aircraft. Metallic meshes have been used to overcome this deficiency. However at high frequencies (UHF, SHF), most of the metallic mesh loses the performance. Regrettably most of the present and upcoming systems onboard of aircraft are functional in the mentioned range of frequencies. Furthermore, passengers are using more and more Personal Electronic Devices (PEDs) onboard of aircraft. Interference caused by PEDs are also in the same range of frequencies. Measured susceptibility caused by PEDs is higher in composite aircraft comparing to metallic one. To develop this disadvantage of composite aircrafts, design of a new lightweight shield, particularly for aeronautic applications, is needed. Metallic nanoparticles have a great potential to be used as new EM shields for aerospace applications. The promising results of this work encourage the designers to use metallic nanoparticles as a new shield for protection of composite aircrafts.

Acknowledgements

I want to thank my supervisor at the department of Mechanical and Industrial Engineering, Dr. Rolf Wuthrich, for the opportunity to join his research group, for giving me the chance of choosing and working on this project, for his professional and competent support, and for the constructive discussions and meetings I had with him. As an extension of my PhD on Electromagnetic Shielding of Composites with Metallic Nanoparticles, I started to work at Bombardier Aerospace in 2009, joining the Core Systems Engineering group under the supervision of Dr. Fidele Moupfouma. I would like to thank him for his support. Moreover, I'd like to thank all the members of the Electrocatalytic Green Engineering Group at Concordia for their inspiring collaboration, as well as Sven Dauterstedt from Technische Universitaet Muenchen (Germany), Cedric Leynaert, Antoine Banieres, Eric Antoine, Lotfi Larhrissi, Robin Ledantec from Université Paul Sabatier - Institut Universitaire de Technologie de Toulouse Département Génie Mécanique et Productique - Techniques Aérospatiales (France) and Timothée Molière from Université de Poitiers (France). I also acknowledge the support of Dr. Alain Michaud of the Institute of National Measurement Standards, NRC, Ottawa for performing electromagnetic characterization.

Finally, I want to thank my wife, Lamia Ziadi and, of course, my mother, Assieh Ahamdi, for supporting me through the entire course of my studies.

This dissertation is dedicated to my son, Jad Jalali

Table of Contents

List of Figures

List of Tables

List of Acronyms

ASRS	Aviation Safety Reporting System
ASTM	American Society for Testing and Materials
CFNC	Carbon Fiber Nanocomposite
CFC	Carbon Fiber Composite
CNS	Communication, Navigation and Surveillance
CNT	Carbon Nanotubes
CVD	Chemical Vapor Deposition
DME	Distance Measuring Equipment
DSC	Differential Scanning Calorimetry
EDM	Electro Discharge Machining
EDS	Energy Dispersive X-ray
EM	Electromagnetic
EMI	Electromagnetic Interference
EMIS	Electromagnetic Interference Shielding
EMS	Electromagnetic Shielding
FAA	Federal Aviation Administration
FWHM	Full Width at Half Maximum
GPS	Global Positioning System
GSM	Global System for Mobile Communications
HF	High Frequency
HIRF	High Intensity Radiated Fields
IEEE	Institute of Electrical and Electronics Engineers

ILS	Instrumental Landing System
IPL	Interference Loss Path
LAN	Local Area Network
MIL-STD	Military Standard
NASA	National Aeronautics and Space Administration
NIST	National Institute of Standards and Technology
PED	Passenger Electronic Device
PNA	Portable Network Analyzer
PVD	Physical Vapor Deposition
RF	Radio Frequency
RTCA	Radio Technical Commission for Aeronautics
SE	Shielding Effectiveness
SEM	Scanning electron microscope
TACAN	Tactical Air Navigation
TCAS	Traffic Collision Avoidance System
TEM	Transverse Electromagnetic
TGA	Thermogravimetric Analysis
TRL	Thru Reflect Line
VHF	Very High Frequency
VNA	Vector Network Analyzer
VOR	VHF Omnidirectional Range
WR	Waveguide Rectangular
XRD	X-Ray Diffraction

List of Formula Symbols

A	Absorption	dB
α	Damping parameter	-
B	Multiple Reflection	dB
d_c	Critical diameter	nm
δ	Skin depth	m
θ	Diffraction angle	°
E	Electric field strength	V/m
ε	Permittivity	F/m
ε_0	Vacuum permittivity	F/m
ε_{eff}	Effective permittivity	-
ε'_{eff}	Real part of Effective permittivity	-
ε''_{eff}	Imaginary part of Effective permittivity	-
f	Frequency	Hz
H	Magnetic field strength	A/m
K	Anisotropy Coefficient	-
λ	Wavelength	m
M_s	Saturation magnetization	A/m
μ	Permeability	H/m
μ_0	Permeability of free space	H/m
μ_{eff}	Effective permeability	-
μ_r	Relative Permeability	-

P	Power	VA
R	Reflection	dB
ρ	Volume resistivity	Ωcm
ρ	Density	kg/cm^3
s	Aperture size	m
S	Scattering Parameter	-
σ	Conductivity	S/m
σ_{eff}	Effective Conductivity	S/m
σ_r	Relative Conductivity	-
t	Thickness	m
T	Transition Coefficient	-
ω	Circle speed	1/s
x_p	Volume fraction of particle	-
Z_0	Wave impedance of free space	Ω

Introduction

Improving electromagnetic (EM) shielding of composite structures (mainly for aerospace applications) with metallic nanoparticles is the goal of this work. The following two sections present the motivation behind the research as well as an outline for the thesis.

Following successful small batch production, composite materials are progressively incorporated into large scale manufacturing for lightweight structures by aerospace and aeronautic industries. Both economic and environmental concerns define the goal of achieving high strength and stiffness, while at the same time lowering density, resulting in a significant reduction in weight. The following properties can be achieved as well by using adequate material configurations:

- Low thermal expansion
- High energy absorption capacity
- Corrosion resistance
- Favorable damping and fatigue behavior.

Considering the major properties of these materials, the replacement of metallic parts with composites is becoming more and more commonplace. Particularly polymer matrix composites (PMCs) with embedded high tensile carbon fibers are becoming popular. But using PMCs creates further challenges for airframe manufacturers. Everywhere in the world, the usage of various electrical systems (e.g. communication, entertainment, and surveillance) is growing exponentially. Each of these systems and

pieces of equipment generate electromagnetic waves, creating a harsh EM environment in which aircraft needs to function.

On the other hand, modern aircrafts rely increasingly on electronic flight and engine control systems. Systems such as fly-by-wire (FBW) and full authority digital engine control (FADEC) perform functions that are critical and essential to flight. Such systems execute independently of mechanical and hydraulic backups. Currently, commercial operational transport aircrafts (e.g., Airbus A320, McDonnell Douglas MD-11 and Boeing B747-400) use full authority electronics for engine control and some aspects of flight control.

Thus, each of those sensitive systems in aircraft should work despite generated electromagnetic interference (EMI) outside (ground based transmitters) or inside (personal electronic devices) the airplane. In the past, metallic aircrafts were able to face EMI challenges successfully due to the Faraday cage mechanism. But the new composite planes without major modifications are not able to provide an acceptable level of deflection or absorption of the radiation. Metallic foils, embedded metallic wires and filaments, or conductive coating are methods that are currently used to improve EM shielding. Among them, metallic mesh (aluminum or copper) is the most accepted method of shielding in the industry. However weight, complexity of manufacturing, corrosion, and providing shielding for low frequencies only are the main disadvantages of this method.

The challenge that the threat of most EMI sources as well as nearly all of susceptible systems onboard are both in the same range of frequencies should be responded urgently.

As a result, a lightweight method of shielding for higher frequencies is an urgent need, especially in aerospace and aeronautic industry. Metallic nanoparticles have great potential to be used for this purpose. Particles can be embedded into the polymer phase of composites, which facilitates the process of manufacturing. Even though the potential of nanoparticles has been demonstrated in other publications, a comparison of the different types and sizes of particles in terms of shielding effectiveness is exclusive to this work. The theoretical background required for both the selection of particles and the understanding of the importance of size, density, and type is the main issue covered by this project. The primary goal is to determine the optimal size and type of particles for electromagnetic shielding (EMS) in higher frequencies. However, without multidisciplinary characterization, the onboard application of these particles would be postponed. Therefore, thermal, microscopic, and mechanical tests are needed to accomplish the following goals:

- Achieve a better distribution of particles and prevent agglomerations
- Ensure that shields made of nanoparticles meet industrial thermal safety standards
- Verify the effect of added particles on mechanical properties of epoxy matrix

Special attention has been devoted to the high capacity of particles (inside a polymer matrix) as a potential candidate for the absorption and prevention of re-reflection inside the fuselage from sources of EMI onboard the aircraft, such as PEDs. Ferromagnetic particles of nickel, iron, cobalt, and iron oxide are selected for the theoretical investigation done in this project. The possibilities of increasing the amount of particles inside PMCs up to the agglomeration limit and, consequently, providing very high conductivity and reflection is discussed in Appendix A.

Following the introduction, five chapters are presented in this thesis. Here, a short summary for each chapter is given:

In Chapter 1, basic concepts of electromagnetic waves are discussed as without a good understanding of the phenomenon itself providing a solution would be worthless. Concepts of electromagnetic interferences (EMI), in terms of high intensity radiated fields (HIRF) and low intensity radiated fields (LIRF) are explained. Special attention is dedicated to PEDs. With respect to the threats that electromagnetic interference poses to the avionic system of an aircraft, the concept of interference path loss (IPL) is defined, and composite and metallic aircrafts are compared. Furthermore, the results of EM penetration studies for composite and metallic aircrafts are provided. The physical mechanism of EMS against interferences is explained. The concept of EMS effectiveness is presented. Explanations for absorption, reflection, and multiple reflection correction factors are given. Metallic mesh, electroless coating, vacuum metalizing, and conductive paint as the main industrial technologies are demonstrated. The limits of these methods are discussed and an introduction to the loss mechanism of microwave absorbers is provided. More detailed explications about microwave absorber materials are provided. Resonant (Dallenbach, Salisbury, Jaumann), graded dielectric (pyramidal, tapered loading, and matching), and cavity damping are the major absorbers that are shown. The shortages of these materials for aeronautics applications as well as an introduction to the application of metallics are explained.

In Chapter 2, the topic is materials and fabrication, but a theoretical background of selection of the size and type of particles as the main focus of this work is given. Metallic nanoparticles are introduced, and their techniques of production are shown. The

three categories of gases, liquids, and solids of particle manufacturing are demonstrated. Spark discharge generation, electrochemical discharge generation (as well as chemical process) and mechanical alloying milling from each category are illustrated. Explanations on the magnetic properties of metallic particles are provided. The theoretical background based on the Maxwell equations is presented. The relationship between shielding effectiveness, magnetic loss and the size and type of nanoparticles is shown. Compositions of nanocomposites containing particles and polymers are explained. The selection of particles (and fabricated samples) based on types and sizes are discussed.

In Chapter 3, different methods of electromagnetic characterization (coaxial holder, dual transverse, free space, and rectangular waveguide) are compared and a relevant method for this work is given. The required thermal and mechanical tests for EM shields are presented. The microscopy characterization and verification by X-ray diffraction (XRD) are provided. The details regarding the experimental setup are presented.

Chapter 4 presents the test results. EM measurements for nickel, iron, cobalt, and iron oxide are given. The comparison of different sizes of particles for iron and nickel are given. The experimental data is compared with the calculated model. Shielding can be applied in different parts of the composite structure. In this chapter, mixing the particles with the polymer phase and fabrication of nanocomposites are presented. The microscopic investigation of nanocomposites, (scanning electron microscope [SEM], optical microscope), thermal analysis (differential scanning calorimetry [DSC], thermogravimetric analysis [TGA]), and mechanical testing (flexion, 4 points) are presented.

Chapter 5 summarizes the present work, identifies the results, and provides suggestions for future investigations.

Appendix A covers the possibility of using the metallic nanoparticles to improve the conductivity and to achieve a better reflection. The fabrication process, characterization, and results are presented in Appendix A. In Appendix B, the estimation of the particle volume fraction is presented. Finally, in Appendix C, the possibilities of using iron-nickel and iron with coated carbon particles are investigated.

The following is a list of innovations presented in this work:

1. Integration of Electromagnetic Shielding (30MHz-1.5GHz) of Polymer Matrix Composites (PMCs) to Process of Nanoarticle (Nickel) Fabrication of Electro Chemical Discharge (ECD). Observation of Formation of Carbon Nanotubs on Nickel nanoparticles (deposited on Carbon Fiber).
2. Integration of Electromagnetic Shielding (30MHz-1.5GHz) of Polymer Matrix Composites (PMCs) to:
    - Process of Nanoparticle (Silver/Copper) Fabrication of Spark Discharge Generation
    - Process of Nanoparticle (Iron Oxide) Fabrication of Chemical Reaction
3. Electromagnetic Shielding of Composite Aircraft with Ferromagnetic Metallic Nanoparticles
4. Integration of Nanoparticle Production by Mechanical Alloying/Milling to Waste Production of MicroEDM process (saving 10,000 kg/year of waste into environment)

5. Comparative Investigation about Different Type and Size of Ferromagnetic Nanoparticles for Electromagnetic Shielding as well as Shielding of Polymer Matrix Composite containing Carbon Fiber in X-band (8.2GHz to 12.4GHz)

Also, the following is a list of various publications within scientific community presented in the framework of this project (3 journal papers and 14 conferences/workshops):

1. M. Jalali, T. Molière, A. Michaud and R. Wüthrich "Multidisciplinary Characterization of New Shield with Metallic Nanoparticles for Composite Aircrafts" Composites Part B: Engineering, Volume 50, 309–317, July 2013
2. F. Moupfouma, W. Tse, D. Lalonde, M. Jalali, A. C. Ndoye, Impact of Electromagnetic threat on the choice and design of Avionic systems more suitable to composite aircraft, CASI AERO 13, 2013
3. D. Lalonde, F. Moupfouma, A. C. Ndoye, M. Jalali, W. Tse, Proposition of a Certification/Exemption Rationale to Demonstrate PED Tolerance in Support of Bombardier Aerospace Aircraft Operators, CASI AERO 13, 2013
4. M. Jalali, F. Moupfouma, T. Moliere, R. Wuthrich, Electromagnetic Shielding of Composite Aircraft Structure with Metallic Nanoparticles, Aerospace Manufacturing and Automated Fastening Conference & Exhibition September 2012, Texas, USA
5. M. Jalali, F. Moupfouma, S. Dauterstedt A. Michaud R. Wuthrich, Light Weight Electromagnetic Shielding for Composite Aircraft, SAE 2011 AeroTech Congress, 2011, Toulouse, France

6. M. Jalali, S. Dauterstedt, A. Michaud and R. Wüthrich, Electromagnetic shielding of polymer-matrix composites with metallic nanoparticles, Composites Part B: Engineering volume 42, 1420-1426, September 2011
7. M. Jalali, S. Dauterstedt, F. Moupfouma, A. Michaud, R. Wüthrich, Improving Aircraft Safety with Metallic Nanoparticles, Nanotech 2011 Conference, June 2011, Boston, USA
8. M. Jalali, S. Dauterstedt, F. Moupfouma, A. Michaud, R. Wüthrich, More wireless systems onboard of aircraft with metallic nanoparticles, CANEUS Fly By Wireless Workshop, 2011, Montreal, Canada
9. M. Jalali, F. Moupfouma, S. Dauterstedt, R. Wüthrich, Aircraft Design and Development Symposium, Electromagnetic Protection for Avionic Systems on Composite Aircraft, CASI 2011, Implementation of new technologies, May 2011, Montreal, Canada
10. M. Cherkaoui, M. Jalali, F. Moupfouma, Aircraft Design and Development Symposium, Aircraft Skin and Joint Design Parameters Impact on Electrical Resistance and Lightning Damage, CASI 2011, Implementation of new technologies, 2011, Montreal, Canada
11. M. Jalali, A.G. Terpstra, R. Wüthrich, Fabrication of Metallic Nanoparticles through Waste of Micro-EDM, European Society for Precision Engineering and Nanotechnology (EUSPEN), May 2009, San Sebastian, Spain
12. M. Jalali, R. Wüthrich, Improving Electromagnetic Shielding of Composite Structure with Metallic Nanoparticles Synthesized by Electrochemical

Discharges, EMC Europe Workshop, 2009, Materials in EMC Applications, 2009, Athens, Greece

13. M. Jalali, P. Maillard, R. Wüthrich, Toward a better understanding of glass gravity-feed micro-hole drilling with electrochemical discharges, Journal of micromechanics and microengineering, volume 19, issue 4, 045001, 2009
14. M. Jalali, R. Wüthrich, Electromagnetic Shielding of Composite Materials Using Electrochemical Discharge Nanoparticles, EUROEM, 2008, Lausanne, Switzerland
15. M. Jalali, R. Wüthrich, A novel Method for Synthesis of Metallic Nanoparticles by Electrochemical Discharge, 10th Anniversary International Conference of the European Society for Precision Engineering and Nanotechnology (EUSPEN), 2008, Zurich, Switzerland
16. M. Jalali, R. Wüthrich, Modeling Gravity Feed Micro Hole Drilling by Electrochemical Discharge, ICOMM-2007 2nd International Conference on Micro-Manufacturing, Greenville, South Carolina, USA
17. M. Jalali, R. Wüthrich, Low-Cost and Fast Prototyping of Micro-Fluidic Devices by Spark Assisted Chemical Engraving CWMEMS 2007, 5th Canadian Workshop on MEMS and Microfluidics, Montreal, Canada

Chapter 1 Theoretical Background

1.1 Fundamental of Electromagnetic Waves

Whenever an electromagnetic wave strikes a conductive object, electrons are excited and surface current is generated. The surface currents transmit electromagnetic energy, which is temporarily entrapped on the object's surface. The energy will be absorbed or re-radiated by the object.

Electromagnetic waves can be analyzed by solving Maxwell's equations, which are governed by four equations [1]:

$$\nabla x\vec{E} = -\frac{\partial \vec{B}}{\partial t} \qquad \nabla x\vec{H} = \vec{J} + \frac{\partial \vec{D}}{\partial t} \qquad \nabla.\vec{B} = 0 \qquad \nabla.\vec{D} = \rho \qquad (1)$$

where:

E is the Electric Field Intensity (V/m)

D is the Displacement Flux (C/m^2)

B is the Magnetic Induction Flux (T or Wb/m^2)

H is the Magnetic Field Intensity (A/m)

ρ is the Electric Charge Density (C/m^3)

J is the Electric Current Density (A/m^2)

Solutions of all electromagnetic problems incorporate the following material properties related equations:

$$\vec{D} = \varepsilon_r \varepsilon_0 \vec{E} \qquad \vec{B} = \mu_r \mu_0 \vec{H} \qquad \vec{J} = \sigma \vec{E} \tag{2}$$

where:

ε_0 =8.854 x 10-12 F/m is the permittivity of air

μ_0 =0.4 x 10-6 H/m is the permeability of air

ε_r is the complex relative permittivity

μ_r is the complex relative permeability

σ is the conductivity of material (S/m).

The relative complex permittivity and permeability can be written as:

$$\varepsilon_r = \frac{\varepsilon}{\varepsilon_0} = \varepsilon_r^{'} + i\varepsilon_r^{''} \tag{3} \qquad \mu_r = \frac{\mu}{\mu_0} = \mu_r^{'} + i\mu_r^{''} \tag{4}$$

Equation (1) can be written as:

$$\nabla \times \nabla \times \vec{E} + \frac{1}{c^2}\frac{\partial^2 \vec{E}}{\partial t^2} = -\mu_0 \mu \frac{\partial \vec{J}}{\partial t} \tag{5}$$

$$\nabla \times \nabla \times \vec{H} + \frac{1}{c^2}\frac{\partial^2 \vec{H}}{\partial t^2} = \nabla x \vec{J} \tag{6}$$

where *c* is the speed of light:

$$c = \frac{1}{\sqrt{\varepsilon\mu}} \tag{7}$$

In the case the of a harmonic field $E(r,t) = E(r)e^{j\omega t}$, the wave equation of $\boldsymbol{E}$ simplifies to:

$$\nabla^2 \vec{E} + \omega^2 \mu\varepsilon \vec{E} = j\omega\mu \vec{J} + \nabla\nabla \cdot \vec{E} \tag{8}$$

where ω is angular frequency. In the case of free space (or σ=0), the above equation becomes:

$$E(r,t) = E_0 e^{-j(\hat{k} \bullet \hat{R} - \omega t)} \tag{9}$$

Where $\hat{k}$ is the direction vector of wave propagation with wavelength $\lambda = 2\pi/\omega$. The relevant solution for the magnetic field is:

$$\vec{H}(r) = \frac{k}{\omega\mu} \bullet \hat{k} x \vec{E}(r) \tag{10}$$

With $k = (\omega^2 \mu\varepsilon)^{1/2}$. The magnitude ratio of E to H is the wave impedance Z:

$$\frac{E}{H} = \frac{\omega\mu}{k} = \sqrt{\frac{\mu}{\varepsilon}} = Z \tag{11}$$

This shows that the impedance is a function of the permeability and permittivity of the medium that wave propagates in. In the case of normalizing impedance where the wave impedance is divided by the impedance of air, Z_0, the above equation becomes:

$$\frac{Z}{Z_0} = \frac{\sqrt{\frac{\mu}{\varepsilon}}}{\sqrt{\frac{\mu_0}{\varepsilon_0}}} = \sqrt{\frac{\mu_r}{\varepsilon_r}} \tag{12}$$

In summary, the electromagnetic wave equation is derived from Maxwell's equations and demonstrates that an electromagnetic wave has both magnetic and electric components (perpendicular to each other, oscillating in the time and space phase). The ratio of E and H is the wave impedance associated with the permeability and permittivity of medium. The far field is called to the region greater than $\lambda / 2\pi$ (λ is the wavelength as shown in Figure 1). The wave is known to be a plane wave because in the far field, all radiated EMI waves essentially lose their curvature, and the surface containing E and H becomes a plane.

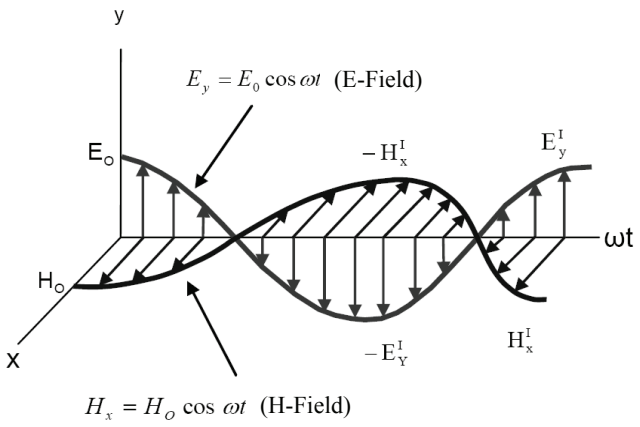

Figure 1 Electromagnetic Wave

When a wave interacts with the surface of an object (one that is semi-infinite), part would be reflected and part would be transmitted. The reflection depends on the material and frequency of propagation. The reflection coefficient (R) for the normal incident would be calculated by the normalized impedance Z/Z_0.:

$$R = \frac{\frac{Z}{Z_0} - 1}{\frac{Z}{Z_0} + 1} \tag{13}$$

R is a complex number (normalized impedance is a function of relative permittivity and permeability). By referring to R, normally a phase angle is neglected and only the amplitude of R in dB is mentioned. The reflection coefficient is then written as

$$|R|(dB) = 20 \log_{10} |R| \tag{14}$$

Wave impedance presents how the relative permeability and permittivity (material properties) can affect the reflection coefficient.

1.2 Concepts of Electromagnetic Interference

EMC and EMI, two concepts developed by IEEE journals and EMC regulations, are defined as [2]:

Electromagnetic Compatibility (EMC) is the ability of a system to be functional in its expected electromagnetic environment within a well-defined level of safety and at design level of efficiency without intolerable degradation because of interferences.

Electromagnetic Interference (EMI) is the process in which electromagnetic disturbance is transferred from one electronic equipment to another through radiation, conducted paths or both. Through shielding (or filtering), EMI energy is reduced/eliminated.

Susceptibility is a relative quantity of the inclination of system to be disturbed or damaged by EMI exposure. It shows the deficiency of protection. Protection is a relative measure of capability of system to resist electromagnetic energy.

Electrostatic Discharge (ESD) is a transmission of electric charge between objects with different electrostatic potential in nearness or by direct contact.

EMI for aircraft are categorized into 2 groups [3]:

- High Intensity Radiated Field
- Low Intensity Radiated Field

In Figure 2, a schema of different EMI sources of aircraft is shown.

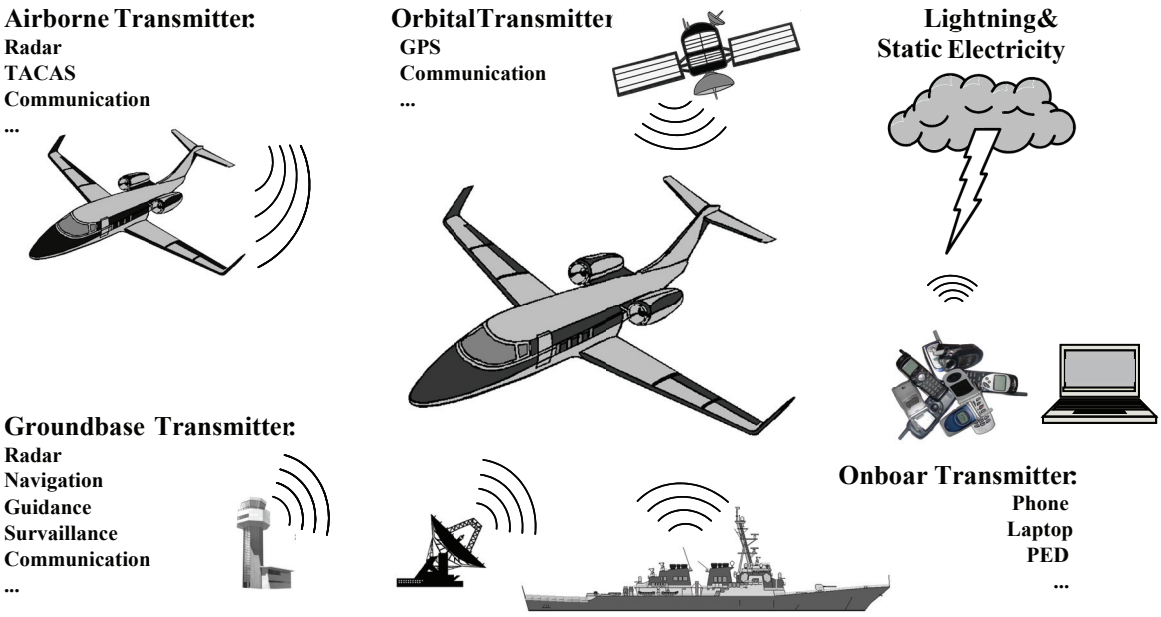

Figure 2 EMI sources of an aircraft

1.2.1 INTERNAL ELECTROMAGNETIC INTERFERENCE

Internal electromagnetic interference can contain Low Intensity Radiated Field (LIRF) and Personal Electronic Devices (PEDs).

PEDs are a vast group of EMI sources that contains laptop computers, cell phones, wireless accessories (both voice and data transmitters). Cell phones work in the range of 940 MHz (GSM900) to 1719MHz (GSM1800) and can affect the performance of avionic equipment [4].

Also, accessories such as laptops and handhelds can affect electronic aircraft systems when working in the GHz range. There are also Bluetooth radio specifications for ranges of frequencies of 30-1000 MHz, 1-12.75 GHz, 1.8-1.9 GHz, and 5.15-5.3 GHz. When PEDs generate radiation in frequencies critical to the avionics equipment, they can confuse or even disable the communication and navigation systems of aircraft. There is also the intermodulation interference that can occur onboard when an undesired

combination of several signals takes place. Furthermore, unwanted frequencies that can cause interference in adjacent receivers may be located onboard. Intermodulation products are classified by their order (2nd, 3rd, 4th, ..., Nth). The frequencies that give rise to the products are designated by capital letters (A, B, C, etc.). These terms may include "harmonics" which can be treated in several ways: the 2nd harmonic of frequency “A” is designated “2A” and therefore contributes 2 terms; the 3rd harmonic of frequency B is designated "3B” and contributes 3 terms, and so on. The general equation for the intermodulation product is written as

$$I.M. = n_1A \pm n_2B \pm n_3C \pm .... \quad (15)$$

where A, B, C etc. are the mixing frequencies and n_1, n_2, n_3, *etc.* are the harmonics, or multiples of the mixing frequencies.

1.2.2 EXTERNAL ELECTROMAGNETIC INTERFERENCE

External EMI comes from any of a vast list of different sources, but they can be categorized as either man-made or environmental. For the latter, the most significant sources are lightning and electrostatic discharges. When lightning strikes an aircraft, it introduces a range of electric currents into the structure (up to one hundred thousand amperes). Strikes can cause substantial physical damage, which are out of scope of this thesis (shown in Figure 3). These currents disperse into structures and come with changing electromagnetic fields that can penetrate the aircraft. The fields and structural IR voltages represent a part of the internal lightning environment. These cause the

voltages and currents within connecting wiring (being sensitive equipment). Sometimes, fields inside aircraft can even penetrate equipment enclosures and put at risk the functionality of the system.

Figure 3 Lightning Damage to Radome

Precipitation static is another environmental phenomenon that has to be considered. When an aircraft flies through dry precipitation in the form of frozen rain or snow, the impact of these particles on the aircraft will cause a phenomenon of triboelectric charging, known as precipitation static or P-static. This process produces interference and static in the aircraft communications and low frequency navigation aids. Man-made external sources (high intensity radiated fields [HIRF]) are the interference that come from terrestrial or extra-terrestrial locations [5]. In December of 1989, the FAA issued its first regulatory requirement for HIRF: an interim policy that requires that critical avionics on new aircraft be shielded to withstand an illumination of 100 V/m over a frequency range from 10 kHz to 18 GHz, following test procedures established by the RTCA [6]. There is a very long list of these sources, including commercial broadcast

stations working in VHF, UHF, communication satellites, and aviation navigation systems. Also, radars generate large peak pulse powers and relatively high harmonic radiation in frequency ranges of 225 MHz to 35 GHz.

1.2.3 THREATS OF ELECTROMAGNETIC INTERFERENCE TO THE AIRCRAFT

An interference sources, the interference path loss, and a victim are the three main elements of an electromagnetic threat against an aircraft (shown in Figure 4).

Figure 4 Source (e.g. cell phone), Path Loss (Fuselage), and Victim (e.g. avionic system)

The propagation loss is referred to as interference path loss (IPL), which shows the level of attenuation of signals propagating from a source (e.g. cell phone) to aircraft avionics (opposite of the interference path coupling [IPC]). As a result, a low IPL means that the strong interference signals at the receiver (or high IPC) and not desirable. In comparative studies done by NASA, IPL measurements were performed for aircrafts carriers of 4-16 passengers and crew [7]. A metallic Lear Jet 35A of Bombardier and a composite Cirrus SR-22 GTS were investigated during this study [7]. The measurement approach was based on using a tracking spectrum analyzer with a frequency generator to perform synchronized sweeps with the analyzer. The generator produced a known output

power level to the transmission antenna at the same time that the analyzer records the peak coupled power to the aircraft antenna port (a biconical antenna and a dual ridge horn antenna are used as the transmit antennas). The setup for a passenger cabin excitation and a top mounted aircraft antenna is shown in Figure 5.

The measurements are performed for different aircraft systems, including localizer (LOC), very high frequency omnidirectional range (VOR), very high frequency voice communication (VHF-Com), glideslope (GS), distance measuring equipment (DME), air traffic control transponder (ATC), traffic collision avoidance system (TCAS) or traffic collision alert device (TCAD), and global positioning system (GPS) are shown in Figure 6. The results of IPL tests show that composite aircraft (SR-22 GTS) provide lower shielding between external antennas and the passenger cabin.

In other studies done by NIST on electromagnetic penetration of different aircrafts for the FAA, cavity coupling characteristics between antennas placed at different angular positions around aircrafts were measured [9]. The field uniformity within these cavities with antennas placed in various compartments inside the aircraft was determined as well. The off-the-shelf components used for this measurement include high frequency (1-18 GHz) double-ridged guide (DRG) horn antennas, a vector analyzer (VNA), interconnecting transmission media, and an amplifier. Connections between transmitting and receiving antennas are made by use of electro-optic links. Low frequency antennas (0.1 to 1.5 GHz) include two ultra-wideband transverse electromagnetic (TEM) horn antennas. A schema of the test is shown in Figure 7. Their work shows a higher level of electromagnetic penetration for a composite aircraft (Hawker-Beechcraft Premier IA) compared to a metallic aircraft (Bombardier Global 5000).

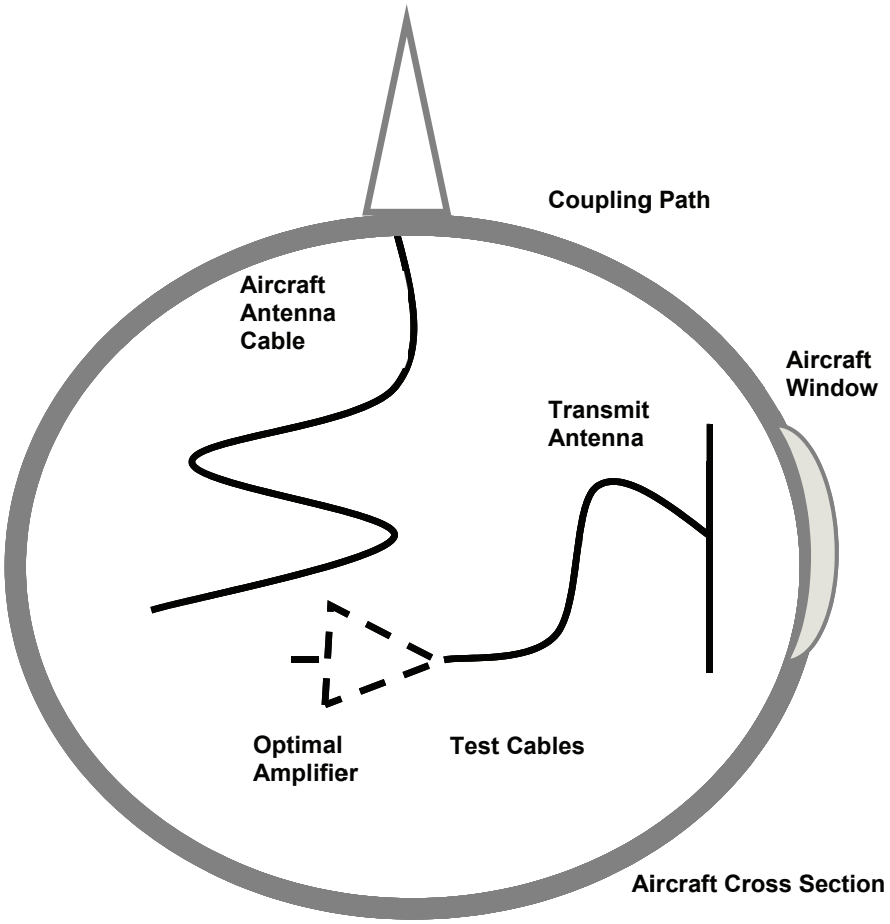

Figure 5 Test setup for IPL

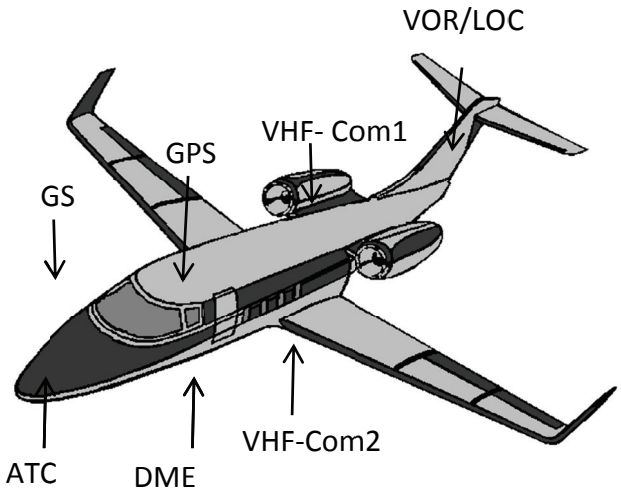

Figure 6 Schema of LearJet 35A [8]

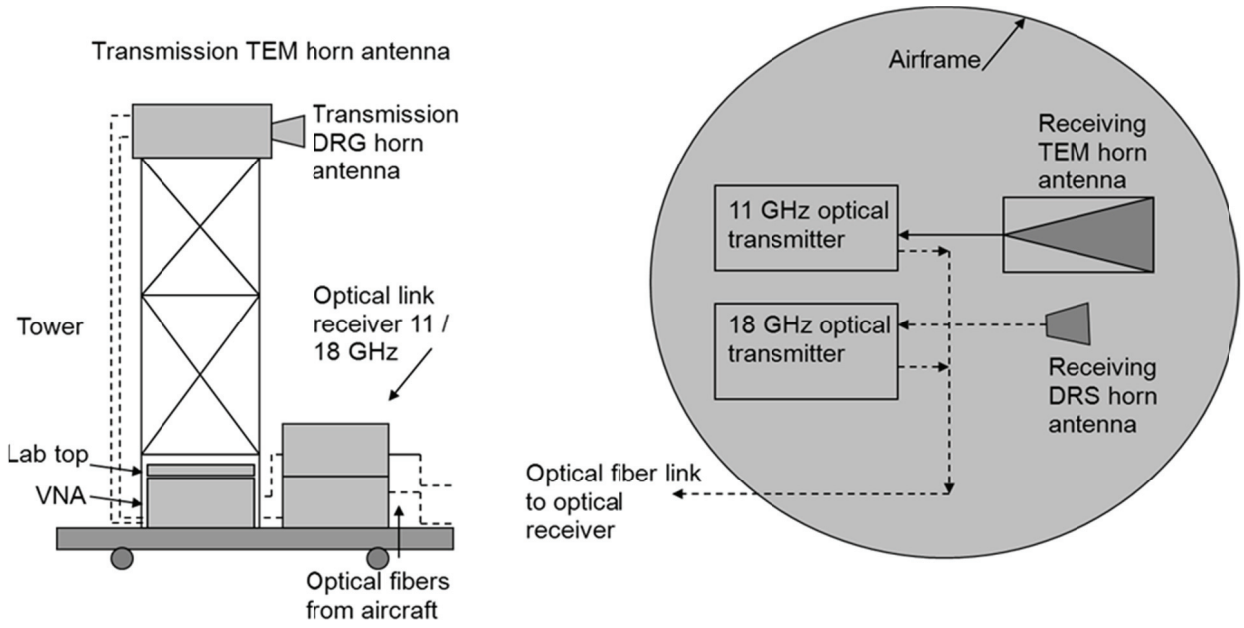

Figure 7 Electromagnetic Penetration Test Setup

1.3 Electromagnetic Interference Shielding

In the last section, it was shown that composite aircrafts have a lower electromagnetic protection compared to metallic ones. As a result, extra protection is needed. Here, a general consideration of a physical mechanism for electromagnetic (EM) shielding against unwanted EM emissions as well as industrial technologies of shielding is presented. Electrical fields of EM waves are generated and easily interact with high impedance voltage driven circuitry (e.g. straight wire or dipole). Magnetic fields of EM waves are generated, and most interact with low impedance current-driven circuitry (e.g. wire loops) [5]. The interference path loss (IPL) of the shield is a function of the material, frequency, and distance from the source. The ability of a shield to attenuate an EM field (or control radiated EM energy) is referred to as its shielding effectiveness (with unit of

decibel dB). Shielding effectiveness (SE) is defined as the ratio of the two values of EM field strength before and after (indices of 1 and 2) placing the shield:

$$SE_{dB} = 20 \cdot \log\left(\frac{E_1}{E_2}\right) \qquad SE_{dB} = 20 \cdot \log\left(\frac{H_1}{H_2}\right) \tag{16}$$

1.3.1 PHYSICAL MECHANISM

Reflection (R), Absorption (A) and Multiple Reflection (B) are three mechanisms of electromagnetic shielding (Figure 8) [10]. A conductive material is the best candidate for reflection as its shielding is based on mobile charge carriers (electrons) in the material. These mobile charges carriers generate an impedance mismatch between free space wave impedance and essential impedance of the shield. Because of this mismatch, a large part of incident field is reflected.

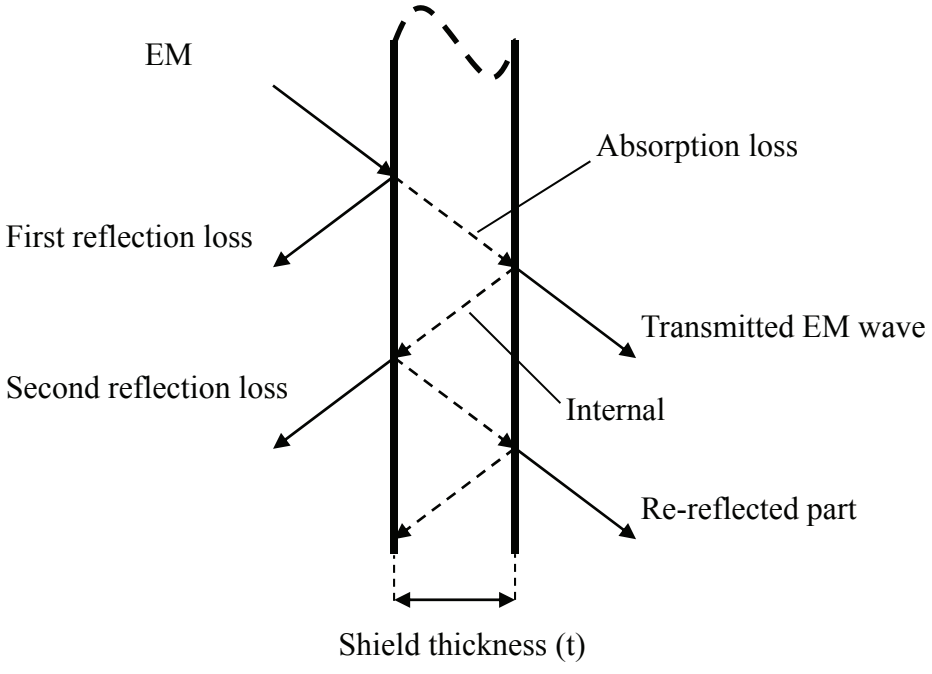

Figure 8 Mechanism of Electromagnetic shielding

Equation (14) can be rewritten by the transmission coefficients of the first and second air/shield interface (T_1 and T_2) and results in [11]:

$$R_{dB} = -20 \cdot \log|T_1 T_2| = 20 \cdot \log \frac{(1+k)^2}{4 \cdot k} \tag{17}$$

where $k = Z_0/Z_s$ and Z_s is the impedance of shield.

Absorption is another mechanism of shielding that necessitates electric and/or magnetic dipoles in the shield [12]. Normally the magnetic loss is generated by the imaginary part of permeability and occurs in the following ways [13]:

- Hysteresis
- Domain wall motion
- Eddy currents
- Ferromagnetic resonance (FMR)

Hysteresis is due to irreversible magnetization that is negligible for very weak or high frequencies (e.g. microwaves) of the applied field. Skin depth is defined as the necessary distance for the wave to be attenuated to 1/e or 37% of its initial amplitude:

$$\delta = \frac{1}{\sqrt{\pi f \sigma_S \mu_S \mu_0}} \tag{18}$$

where *f (Hz)* is the frequency

σ_S *(S/m)* is the material conductivity

μ_S is the relative permeability of the material

$\mu_0 = 4x\pi x10^{-7} H/m$ is permeability of free space

The skin depth is reduced by increasing the permeability of shield and/or conductivity. The absorption loss can be defined as in [14]:

$$A_{dB} = 20 \cdot \log\left(e^{t/\delta}\right) = 8.686\left(\frac{t}{\delta}\right) \tag{19}$$

where t(m) is the thickness of shield. Re-reflection which is caused by interference sources (e.g. PEDs) inside cabin can be reduced by high capacity EM absorber.

The multiple reflection happens on the surface or interface between the shields. The multiple reflection correction term stands for the reduction in shielding effectiveness of the shield with low abruption loss, referring to multiple reflections inside the shield (in case of A>15dB, multiple reflections can be neglected [15]):

$$B_{dB} = 20 \cdot \log\left|1 - \frac{(k-1)^2}{(k+1)^2} \cdot e^{-2t/\delta}\right| \tag{20}$$

The general term for electromagnetic shielding effectiveness is the sum of reflection (R), absorption (A) and re-reflection (B):

$$SE_{dB} = R_{dB} + A_{dB} + B_{dB} \tag{21}$$

1.3.2 STANDARD METHODS OF EM SHIELDING

Aluminum and aluminum alloys used in aircraft structures have a very high electrical conductivity (around 3.54 x 10^7 S/m for Al, which is 61% of copper's conductivity) and consequently provide an excellent shielding with an effectiveness of 100dB (fasteners provide the needed continuity of aircraft structures, however in some cases they allow leaking and degradation of the shielding as well).

The aeronautic and aerospace industries are using more and more polymer matrix composites (PMCs), particularly with carbon fibers, because of their superior mechanical properties and lower weight. For example, the percentage of using composites in a Boeing B787s is 50% (compared that of the old version of the 777, which is 12%). For the Airbus A350-900 XWB, it is around 52%. In the case of Bombardier aircrafts, for the C-series it is 20%, and for the Learjet 85 it is 100%.

The electrical conductivity of composites is not high enough to resist electromagnetic interferences, lightning (direct or indirect effects) or cosmic radiations. Carbon fibers can provide a good level of shielding effectiveness [16], but mostly based on reflection and not absorption, which is needed inside the cabin.

The shielding provided by composites for different parts of the aircraft is not enough. As a solution, metals in the forms of foil and mesh are added to the composites. Expanded copper (or in some cases, aluminum) foil is the most common method of shielding in industry. It possesses good absorption and reflection as well as low weight. The effectiveness depends on the frequency and wavelength of the field [17]:

$$SE_{dB} = 20 \cdot \log(\lambda / 2s) \quad \text{for} \quad s \le 2\lambda \qquad (SE_{dB} = 0 \quad \text{for} \quad s > 2\lambda \;) \tag{22}$$

Where s is the aperture size. As it can be seen in equation 22 of shielding effectiveness of metal mesh, performance decreases with decreasing of wavelength as well as increasing aperture size. The mesh is able to shield only the wavelength larger than half aperture size (Figure 9).

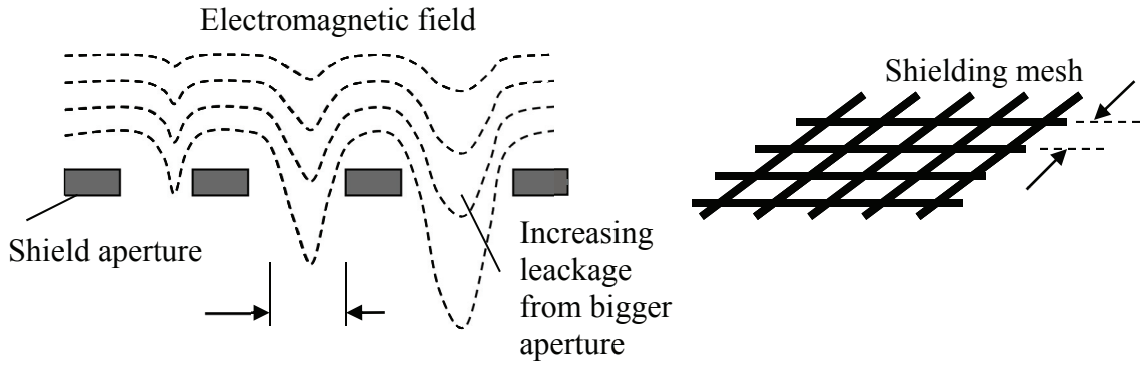

Figure 9 EM shielding with mesh

Decreasing the performance of a mesh, particularly over 1.5 GHz, can be demonstrated with equation 22 as well as Figure 10. Decreasing the aperture and increasing the volume can be done, however the advantage of a lower weight, and consequently of using composites, would be lost. The process of adding metal to composites, from a manufacturing point of view, is not realistic [18, 19].

Copper itself is very conductive, but copper mesh has a high potential for oxidization, and consequently provides a very low conductivity. Using a metallic foil can create a difference of thermal expansion between the foil and the hosted matrix, which causes internal stress. There is also the problem of frazzling of a metallic mesh in manufacturing (e.g. drilling).

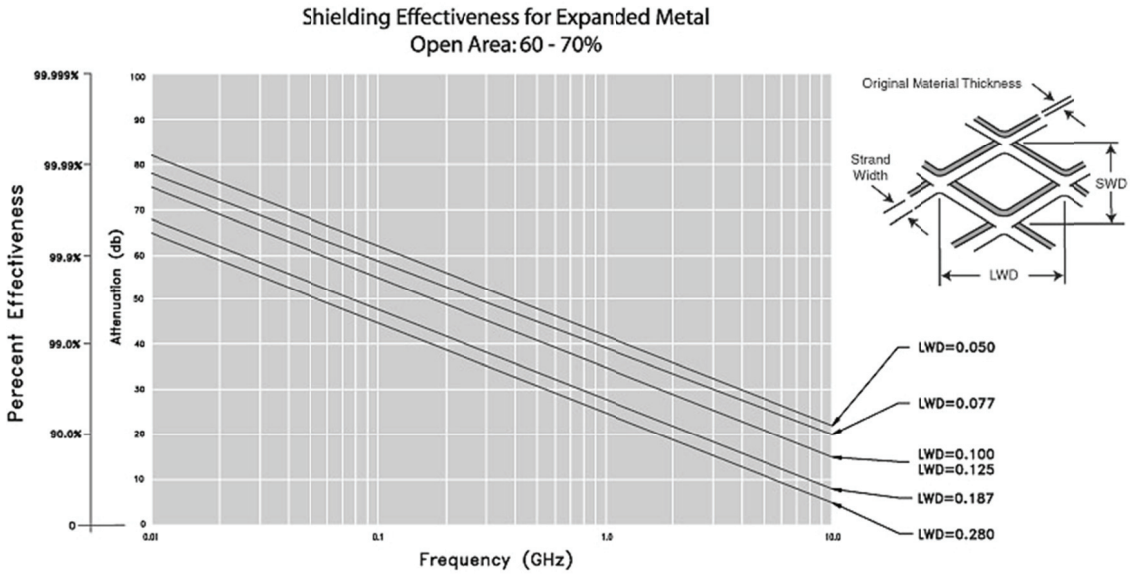

Figure 10 SE of metal mesh for different aperture sizes (www.dexmet.com)

There are different alternatives that have been developed by the industry to replace metallic mesh:

- Electroless coating
- Vacuum metalizing
- Conductive paint

However all of the mentioned methods have the same problems as metallic mesh: they experience decreased performance in high frequencies and oxidization.

1.3.3 LOSS MECHANISM OF MICROWAVE ABSORBERS

As shown in the previous chapter, conventional conductive materials (e.g. a metallic mesh) become less effective at high frequencies. EMI-absorbing materials are different from conducting materials. Absorbers are designed to attenuate the EMI energy. The design of an absorber should be incorporated, with different loss mechanisms in wide bandwidths.

There are two categories of absorbers: free space and cavity. Free space absorbers are known for their resonance at a particular frequency or a narrow range of frequencies (opposite of cavity type of materials). Some materials are better for the low frequency range, while others are better at high frequencies. The most efficient absorbers (from the cavity category) are loaded with high permittivity and permeability materials. Materials with only dielectric properties can also be used as cavity absorbers. Different types of absorbers may or may not have the property of bringing the electric field to zero when the magnetic field is going to maximum [20]. In the designing of absorber materials, the following equation can be used to estimate the absorption capability of the material [21]:

$$A = \frac{1}{2}\sigma E^2 + \frac{1}{2}\omega\varepsilon_0\varepsilon_R E^2 + \frac{1}{2}\omega\mu_0\mu_R H^2 \tag{23}$$

Where A (W/m^3) is the absorbed electromagnetic energy per unit volume

E (V/m) is the electric field strength of electromagnetic radiation

H (A/m) is the magnetic field strength of the electromagnetic radiation

σ (S/m) is the conductivity of the material

ω (sec-1) is the angular speed of the EM wave (equal to $2\pi f$); f is the frequency

ε_0 (F/m) is the dielectric permittivity of the vacuum: 8.854×10^{-12} (F/m)

ε_R (F/m) is the relative permittivity of the material

μ_0 (A/m) is the magnetic permeability of the vacuum: 1.2566×10^{-6} (A/m)

μ_R (A/m) is the relative permeability of the material.

The above equation shows that an absorber attenuates and absorbs the microwave energy by relying on the conductivity, dielectric loss, and/or magnetic loss. Dielectric loss is defined as the imaginary part of the complex permittivity (acting on electric field). Magnetic loss is defined as the imaginary part of the permeability (acting on magnetic field). Their volume resistivity should be higher than 10^8 Ω-cm [22].

1.4 Microwave Absorber Materials

Microwave absorbers are designed based on minimizing reflectivity by shape, structure, permittivity, and permeability to allow absorption of EMI energy at distinct or broadband frequencies. There are three conditions that can minimize the EMI reflection from the surface. Considering an EM wave that propagates through a free space with impedance of Z_0 happening upon a semi-infinite dielectric or magnetic dielectric boundary of impedance Z_M, a partial reflection occurs. The reflection coefficient can be defined as equation (24). When Z_M=Z_0, the reflection coefficient descends to zero (material in the layer is impedance matched to the medium). This is the first condition that minimizes the reflection coefficient. The intrinsic impedance of free space is around 377 ohms. This gives the second condition that results in a minimum reflection coefficient when the electric permittivity and the magnetic permeability are equal. The nominal intrinsic impedance is

$$Z_M / Z_0 = \left(\mu_R / \varepsilon_R\right)^{1/2} \tag{24}$$

where $\varepsilon_R = (\varepsilon_r - i\,\varepsilon_i)/\,\varepsilon_0$ and $\mu_R = (\mu_r - i\,\mu_i)/\,\mu_0$; ε_r and ε_i are the real and imaginary parts of the permittivity, respectively; and μ_r and μ_i are the real and imaginary. If the medium is free space, and both real and imaginary parts of permeability and permittivity are equal, the reflectivity coefficient is zero.

The third condition is the attenuation of the wave when it propagates into an absorbing medium. The power of the wave decays exponentially with distance x, by a factor of $e^{-\alpha x}$. Here, α (known as the Gilbert damping constant) is the attenuation constant of material that can be defined as [23]

$$\alpha = -\left(\mu_0 \varepsilon_0\right)^{1/2} \omega \left(a^2 + b^2\right)^{1/4} \sin\left[(1/2)\tan^{-1}\left(-a/b\right)\right] \tag{25}$$

where $a = (\varepsilon_r\mu_r - \varepsilon_i\mu_i)$ and $b = (\varepsilon_r\mu_i - \varepsilon_i\mu_r)$. To get a considerable attenuation with small thickness, α must be large, and consequently ε_r , μ_i , ε_i must be large. But this condition must be tempered with the first condition, where large permittivity generates large reflection. Then, the absorbing material must be lossy so that EMI energy can be dissipated into material and not reflected back. So, for an absorber, there is a compromise between the front-facing reflection coefficient and the loss per unit thickness.

1.4.1 RESONANT ABSORBERS

Resonant absorbers are produced through tuned or quarter-wavelength absorbing materials structured to absorb EMI energy at different frequencies. Resonant materials normally include Dallenbach layers, Salisbury screens, and Jaumann layers as demonstrated in Figure 11 [23].

In resonant absorbers, the material is thin and the impedance is not matched between incident and absorbing media, and as a result, not all EMI energy is absorbed. Consequently, both the reflection and transmission of EMI wave happen at the first interface.

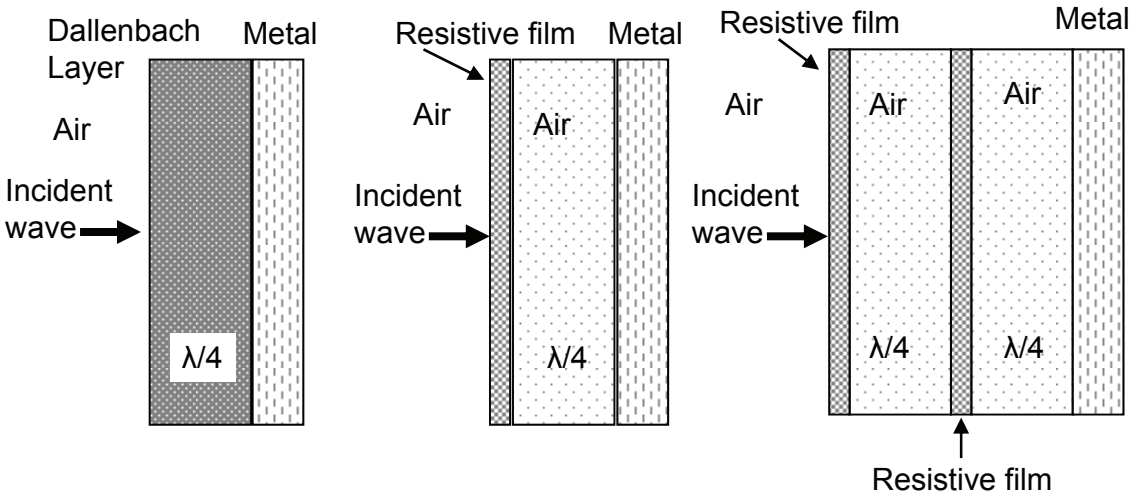

Figure 11 Resonant absorbers (left-to-right): Dallenbach layer, Salisbury screen, Jaumann layers

The Dallenbach layer is placed on a conductive substrate and is made of homogeneous lossy material. To obtain the minimum reflectivity (for certain wavelength), the effective impedance of the layer Z_M should be equal to the incident impedance Z_0. With this method, it's not possible to reach a broadband with just one layer. This absorber is fabricated with ferrite materials, such as silicon rubber, silicon carbide, titanium oxide, and carbon black [24]. This absorber is heavy and not appropriate for aeronautics applications. Creating the needed thickness for this absorber onboard does not seem realistic. Dallenbach is not able to provide the needed broad band EM shielding for aircraft.

Salisbury screen is also a one layer of resonant absorber. It does not depend on permittivity and permeability of the bulk layer. As it's shown in figure 11, it contains a

resistive sheet on an odd multiple of quarter wavelength in front of metal, normally separated by air gaps (or foam of honeycomb). Here as well, weight and occupied space are the most important limits of the method and band width.

Jaumann layers are actually modified versions of Salisbury screens with increased bandwidth and multiple thin, resistive layers separated with spacers on top of the metal backing. The tradeoff of wider bandwidth is the thickness. As a result, here the absorber is even thicker, as well as having the common problem of weight and occupied space.

1.4.2 GRADED DIELECTRIC ABSORBER

Considering equation 24, an EM wave that causes an interface will have some reflection that is proportional to the magnitude of the impedance step between the wave and the transmitting medium. Three types of impedance matching methods (matching, tapered, and pyramidal) are developed to decrease the impedance step between the wave and the absorption milieu [23]. For complete absorption of the wave, a thickness of one or more wavelengths is needed, which makes the absorber bulky and heavier.

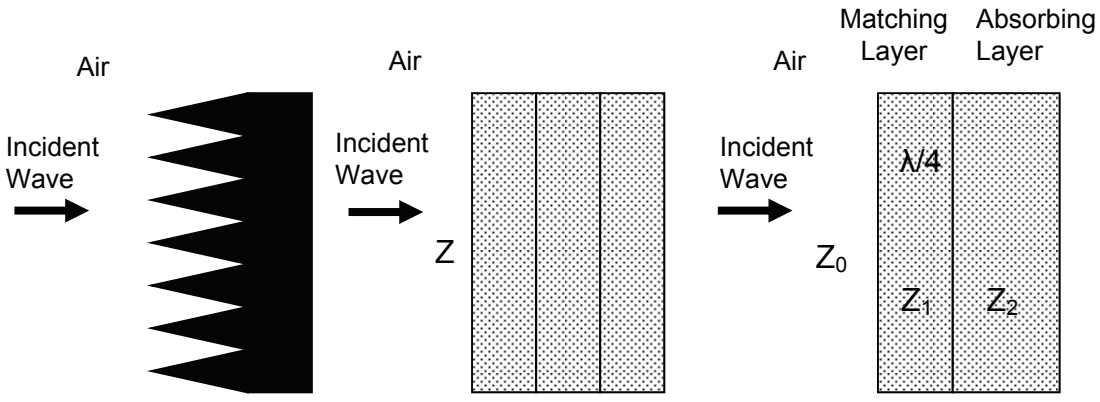

Figure 12 Graded dielectric absorbers by impedance matching

Pyramidal absorbers are pyramidal in shape (Figure 12). They are cone structures widening vertically to the surface of the substantial absorbing material in a repeatedly spaced pattern [25]. Absorption of the pyramidal absorbers is reached by a gradual transition of impedance from that of free space to the absorber. The height and periodicity of the pyramids are designed to be on the order of one wavelength. In case of shorter structures or longer wavelengths, the waves would be absorbed by a quicker change in the impedance. Pyramidal absorbers provide the best performance because they have minimum operational frequencies, above which they offer high absorption over wide frequencies. Pyramidal attenuators are normally used for anechoic chambers that are made of conductive carbon in polyurethane foam. Absorption levels of greater than 50dB can be reached by pyramids many wavelengths thick. Their main disadvantages, particularly for aeronautics applications, are their fragility and thickness. This method can be applied to other materials, such as honeycombs, foams, and netting or multilayer structures to overcome some deficiencies, but the problem of dimension still remains for any onboard usage [23].

The tapered loading absorber is normally a piece made from a mixture of low loss and lossy material. The lossy part is equally dispersed parallel to the incident surface (with a gradient increasing into the slab [26]). A kind of tapered loading material containing an open-cell foam or plastic net, is dipped or sprayed with lossy material from one side or allowed to drain and dry [27]. The manufacturing process in terms of reproducibility of the gradient is not feasible. Another kind is made of homogeneous layers with the raised loading of lossy material in the direction of the wave propagation.

These materials are thinner (their advantage over pyramidal absorbers) but still too thick to be used on civil aircrafts [23].

In matching the layer absorber, a transition absorbing layer is placed between the incident and absorbing milieu to decrease the needed thickness for the gradual transition materials. The thickness and impedance of the transition layer are between two impedances. As a result, the combined impedance from the first and second layers equal the impedance of the incident milieu. If the matching layer is one-quarter of wavelength of the EMI in the layer ($Z_1 = (Z_0Z_2)^{1/2}$), this matching is reached. At a frequency that equals the optical thickness, the impedance matching occurs. As a result, matching layer materials are narrow band absorbers, which is a disadvantage for aeronautics applications. The matching layer absorber can be made of an intermediate impedance transition layer and controlled quarter-wavelength thickness for absorption of microwave frequencies (carbon doped or impregnated urethane foams).

1.4.3 CAVITY DAMPING ABSORBER

Cavity damping absorbers are made of thin elastomeric sheets loaded with high permeability materials that provide broad frequency magnetic loss properties. The resonant or tuned absorbers are better choices from a cost and weight point of view. Thickness, price, and weight are main factors that slow down the onboard usage of these absorbers.

1.4.4 MOTIVATION FOR METALLIC NANOPARTICLES

As it's shown in the previous section, the actual absorbers on the market are not able to provide the needed performance. Consequently, they are not able to overcome the shortage of metallic mesh in high frequencies. Considerable thickness, price, substantial weight, low integrity to the whole structure of the aircraft, and a limited range of frequencies are all factors that prevent the application of these materials in the aeronautics industry.

To address this challenge, nano-size ferromagnetic particles have a great potential to be used as onboard microwave absorbers. Recently, due to the possibility of producing ferromagnetic nanoparticles, research on these particles became of a great interest [28]. It is crucial to understand how the metallic nanoparticles are behaving inside electromagnetic environment. So having a good understanding of magnetic property of ferromagnetic nanoparticle would be a must. Orbital and spin motion of electrons is the fundamental element of magnetism. Interactions of electron as well have a powerful result on magnetism. In case of ferromagnetic materials, there is a strong interactions between atomic moments [29].

Difference of ferromagnetic materials with the rest of materials is based on how they respond to fields. There are three main categories:

- Diamagnetism
- Paramagnetism
- Ferromagnetism (2 subcategories of antiferromagnetism and ferrimagnetism).

In case of diamagnetism, atoms have no net magnetic moments. However by applying a field, their magnetic moments will be in the opposite direction of the field. By removing the field, they lose their magnetization, and a negative magnetization will be formed [29].

In case of paramagnetism, the magnetic moments do not act together, and when the field is removed, the net magnetization will be zero. By applying a field, there will be a limited alignment of the magnetic moments in the direction of the field. As the result, there will be a net positive magnetization. The effectiveness of the moments is influenced by the temperature. This dependency to the temperature is known as the Curie Law [29].

For ferromagnetic materials, parallel alignment of magnetic moments is observed. As the result, there is a considerable net magnetization even when the field is removed. Iron, nickel and cobalt are very well known ferromagnetic materials.

In case of antiferromagnetic materials, antiparallel alignment of the magnetic dipoles is observed. The opposite magnetic moments annul each other. As the result, the net magnetization of the material is zero.

For ferrimagnetic materials (e.g. Iron Oxide), the moments are in anti parallel alignment but they do not annul each other. Resemblances that are observed between ferromagnetic and ferrimagnetic materials are [30]:

(1) Coupling interaction between magnetic moments for both materials

(2) Both form magnetic domains.

(3) Demonstration of hysteresis behavior for both.

Differences between ferromagnetic and ferromagnetic are [30]:

(1) Parallel magnetic moment coupling for ferromagnetic materials and antiparallel for ferrimagnetic.
(2) Comparing to ceramic ferrimagnetic materials, metallic ferromagnetic materials have a very good electrical conductivity
(3) Saturation magnetizations (Ms) of ferromagnetic materials are higher.

Ferromagnetic material contains many domains where the magnetization is constant both in magnitude and direction. By applying a field, domains change their volume by moving the boundary walls (Figure 13).

A plot of the variation of magnetization with the field is called a hysteresis loop (Figure 13). For ferromagnetic materials, the moments do not annul each other. By applying a field to a sample, the magnetization (M) improves up to a maximum value that is known the saturation magnetization (Ms). The resultant M-H curve is known as the preliminary magnetization curve [30]. Both soft and hard magnetic materials on hysteresis loom are shown in Figure 13.

Coercivity is the intensity of the applied field which is necessary to decrease the magnetization of the material to zero following reaching the saturation (Hc). So the applied field on ferromagnetic material executes the work under the hysteresis curve which causes the heat dissipation [31]. Higher Coercivity is equivalent of higher resistance of material to incoming EM wave and higher capacity of EM absorption.

By having the magnetic anisotropy, the overall magnetization Ms of a ferromagnetic prefers to be positioned along a particular direction known as the easy axis.

In case of Cobalt with hexagonal close packed crystal structure, the easy axis is the c-axis. The easy axis of BCC Iron single crystal is in the direction of [*100*]. The less easy is [*110*] direction and the difficult for the [*111*]. In case of FCC Nickel, [*111*] is the easy axis [31]. The shape anisotropy constant K_s is given by [32]:

$$K_s = ½ (N_a - N_c) \bullet M^2 \quad (26)$$

where N_a and N_c are the demagnetization factors of perpendicular and parallel to the easy axis.

The magnetic property of coercivity of particle is controlled by the size. By reducing the size of the particle, a limit will be reached below which the sample cannot be broken into domains and remains as a single domain. The creation of the domain walls is a process controlled by the equilibrium between:

- Magnetostatic energy that augments proportionally to the volume
- Domain wall energy that augments proportionally to the area between domains

If the particle size is decreased, there is a critical size below which it takes more energy to form a domain wall than supporting the external magnetostatic energy [33].

It will be harder to rotate the magnetization than moving the domain wall. As the result, comparing to multidomain particles, for single-domain a larger Coercivity will be obtained [34].

Superparamagnetic which is a phenomenon that material behaves as paramagnetism at temperature below the Curie temperature is out of scope of this work (generally it happens when the dimension of particle decrease into below 10nm). As the temperature is the key element in defining the magnetization of the entire crystallite [35]. Also the Coercivity in the super paramagnetic regime is much less than single domain ferromagnetic particle.

The critical size of a single domain particle with the highest Coercivity is defined based on following equation [36]:

$$D = 18\frac{\sqrt{K_{eff} A}}{\mu_0 M_s{}^2} \tag{27}$$

where A is the exchange constant

K_{eff} is anisotropy constant

μ_0 is the vacuum permeability

M_s is the saturation magnetization

So theoretically by choosing the particles with critical size as well as high saturation magnetization, the maximum area under hysteresis loop will be obtained which in application of EM absorption is desirable.

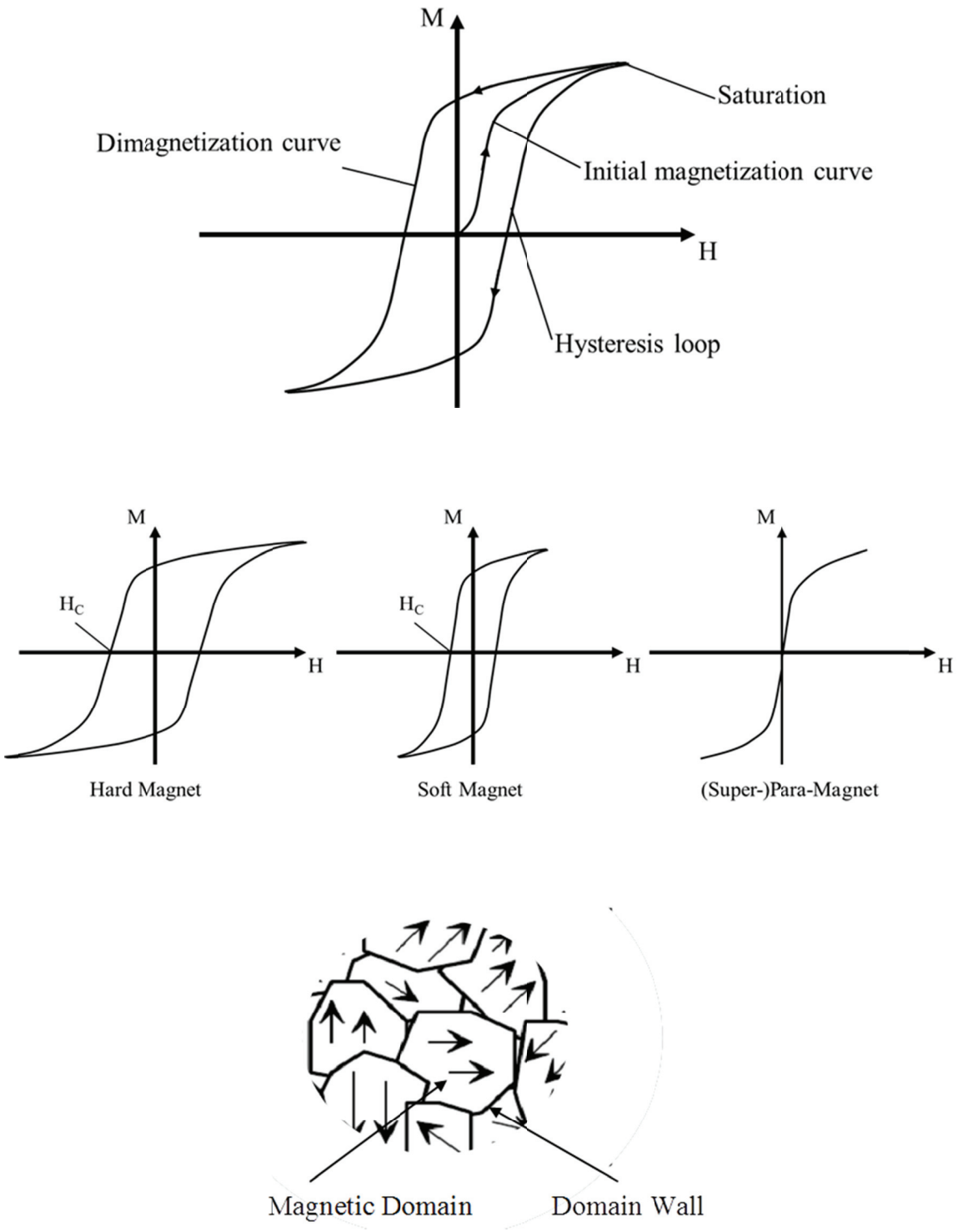

Figure 13 Hysteresis loop, Hard/Soft/Para magnets/Magnetic domains

For nanoparticles, the exchange interactions resulting in the possibility of exchange modes is an important factor that should be considered [37]. Resonance peaks in the absorption spectra are due to the presence of exchange modes [38]. Plot of radio frequency energy absorption versus applied static field characterizes the resonance loss. Line width (ΔH) is defined as the difference between the applied field values and the energy absorption which is one half of the maximum absorption [39]. In combination with the line width, the dimensionless Gilbert damping constant (equation 28) α can characterize the loss:

$$\alpha = (\gamma . \Delta H) / 2\omega \quad (28)$$

where γ is gyromagnetic ratio and for Iron is equal to 2.8 MHz/Oe (for Cobalt is equal 3.11 MHz/Oe). The increase of α by decreasing the size of the particle is due to a surface effect. Having the particle with smaller size will result in more pronounced the effect of surface defects and increased α [40].

To use metallic particles as an absorber shield for composites, different methods can be followed. Particles can be mixed with a polymer phase and used on the surface of composite structures as paint. There is also the possibility of deposition particles on fibers embedded in composites. Another possibility is to mix the particles with the polymer phase of the composite itself. Various possibilities of shielding are shown in Figure 14. In this work, for the purpose of electromagnetic absorption, only the scenarios of mixing the particles with polymer (nanocomposite) are considered.

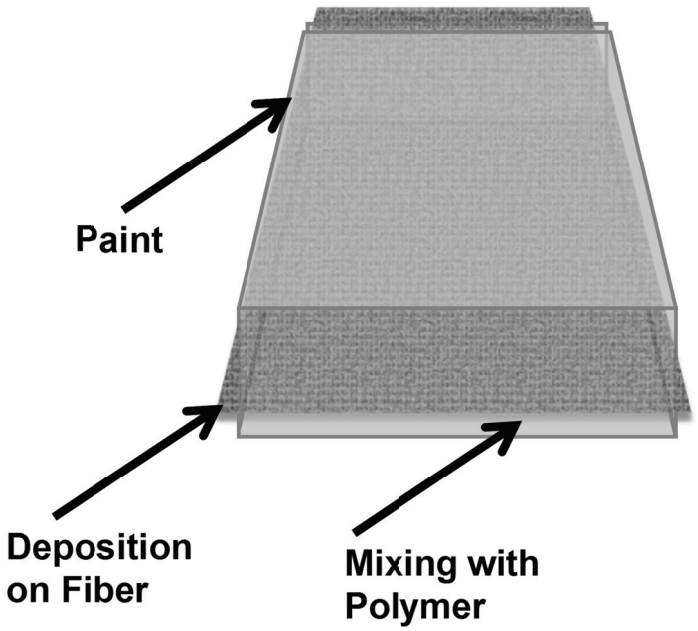

Figure 14 Different possibility of shielding with nanoparticles

As is shown in equation 29, the permeability (or susceptibility, $\mu = \chi + 1$) of nanocomposites containing ferromagnetic particles in polymer phase depends on [41]:

- Saturation magnetization
- Anisotropy constant
- Damping constant

The susceptibility (permeability) is calculated by:

$$\chi = \nu_p \frac{\mu_0 M_s^2}{2K} \frac{R_3 + iR_4(\omega/\omega_0)}{R_1 + 2iR_2(\omega/\omega_0) - (\omega/\omega_0)^2} \tag{29}$$

where

υ_p is the particle volume fraction

M_0 is the permeability in vacuum

M_s is the saturation magnetization

K is the effective anisotropy constant

ω is the frequency of incident wave

ω_0 is the resonance frequency and equal of $\gamma 2K/Ms$

γ is the gyromagnetic ratio

R_1, R_2, R_3 and R_4 are the functions of damping parameter

σ is equal of $KV_p / (k_BT)$ where V_p is the particle volume

k_B is the Boltzman constant

T is the temperature

Increasing the permeability is desirable as it results to the higher level of EM absorption. Type and size of the ferromagnetic particles and their influence on level of EM absorption are the main factors that are investigated in this work.

1.5 Models for EM Shielding Effectiveness Calculation of Composites

Analytical calculation is helpful to predict the electromagnetic shielding of a material, as well as decreasing the needed time for experimental work.

Here, analytical methods for electromagnetic shielding calculations (based on permeability, conductivity and permittivity) in the literature are reviewed. Though the investigated nanocomposites appear as a composition of electric and dielectric materials – metallic nanoparticles and polymer matrix – the application of mixing rules is required that allow the determination of effective parameters for the noted material properties.

1.5.1 SHIELDING EFFECTIVENESS CALCULATION MODELS

There are diverse models for calculating the shielding effectiveness (SE) of reflection (R), absorption (A) and multiple reflection (B) in dB as the following [40,41]:

$$R_{dB} = 108.1 - 10\log_{10}(\mu_r f_{MHz} / \sigma_r) \tag{30}$$

$$A_{dB} = 1314.3 t_{cm} \sqrt{f_{MHz} \sigma_r \mu_r} \tag{31}$$

$$B_{dB} = 20\log_{10}(1 - e^{-2t\sqrt{\pi f \mu \sigma}} e^{-j2t\sqrt{\pi f \mu \sigma}}) \tag{32}$$

where μ_r and σ_r are the relative permeability and conductivity of the shielding material, respectively, *f (MHz)* is the frequency of the penetrating electromagnetic field and *t(cm)* is the thickness of the shield. Equations (30)-(32) are initially proposed to calculate the shielding of metal materials, but are also good for composites. In any case, the part of absorption by a factor 10^3 results in better results, especially for higher frequencies [42].

$$A_{dB} = 1.32 t_{cm} \sqrt{f_{MHz} \sigma_r \mu_r} \quad (33)$$

More models to estimate SE of composites are presented [43-45]:

Classical Good Conductor Approximation

The classical electromagnetic good conductive approximation calculates the shielding effectiveness mainly for conductive polymer blends (with high concentration of conductive fillers). As the result, this model predicts perfectly in case of shielding mechanism of the system that is mainly based on reflection and multiple reflections. This model can be used for all samples that fulfill the classical good-conductor approximation for both electrically thin (thickness<skin depth) as well as electrically thick (thickness>skin depth) over the frequency range of interest.

$$SE = 10\log\left(\frac{\sigma_{eff}}{32\pi f \varepsilon_0}\right) + 20\frac{t}{\delta}\log(e) \quad (34)$$

Where $\delta = \frac{1}{\sqrt{\pi f \sigma_{eff} \mu_{eff} \mu_0}}$ is the skin depth

σ_{eff} *(S/m)* is the effective bulk conductivity

f (Hz) is the frequency

$\varepsilon_0 = 8.85 \times 10^{-12}$ *F/m* is the vacuum permittivity

t (m) is the material thickness

μ_{eff} *(H/m)* is the effective relative permeability of the material

$\mu_0 = 4 \times \pi \times 10^{-9}$ *H/m* is permeability of free space.

Simon Formalism

The shielding effectiveness of the composites can be obtained by Simon formalism even at high frequencies for electrical conductive materials. This model neglects the contribution of multiple reflections and can be used up to a few GHz. This model is been developed for high conductive materials. This model is been used mainly for composite materials containing microparticles with concentration over percolation limit.

$$SE_{dB} = 50 + 10\log(\rho f_{MHz})^{-1} + 1.7t(f_{MHz}/\rho)^{1/2} \quad (35)$$

where ρ *(Ωcm)* is the volume resistivity

f (MHz) is the frequency

t (cm) is the material thickness.

Colaneri and Shacklette

Colaneri and Shacklette can be used for intrinsically conductive polymers (with various conductive fillers) with the most reliable performance for far-field shielding. This model is developed for electrically thin samples (thickness << skin depth) with micor particles inside polymer matrix.

$$SE = 20\log\left(1 + \frac{Z_0\sigma_{eff}d}{2}\right) \quad (36)$$

where Z_0*=377Ω* is the impedance of free space

σ_{eff} *(S/m)* is the bulk conductivity.

Schelkunoff Theory

Shielding effectiveness can be predicted for the plane wave with transmission theory of Schelkunoff which is been used mainly for composites containing (micro) particles. This model is been used for single, double, and laminated shields for both solid and perforated sheets. This model is been used both for microwave as well as range of frequency between 100 Hz and 50 kHz.

$$SE_{dB} = 20\log\left(\frac{\pi}{\mu_0\sigma_{eff}}\right)^{1/2} + 20\log\left(t(\varepsilon_{eff}+1)\right) - 20\log(2\varepsilon_{eff}) \tag{37}$$

where $\mu_0 = 4x\pi x10^{-7} H/m$ is permeability of free space

σ_{eff} *(S/m)* as the bulk conductivity

ε_{eff} *(F/m)* is the permittivity of the material

t (m) is the material thickness.

1.5.2 MIXING MODELS FOR COMPOSITES

The estimation of electromagnetic (EM) shielding effectiveness of composites with one of the above models of EM shielding can be realized either by getting the necessary input parameters (e.g. conductivity and permittivity) through experiments [46], or by using the mixing rules to estimate properties of the composites. The Maxwell Garnett formulation is the most popular mixing rule for conductive/dielectric mixtures [47]:

$$\varepsilon_{eff} = \varepsilon_b + \frac{\frac{1}{3}\sum_{i=1}^{n} f_i(\varepsilon_i - \varepsilon_b)\sum_{k=1}^{3}\frac{\varepsilon_b}{\varepsilon_b + N_{ik}(\varepsilon_i - \varepsilon_b)}}{1 - \frac{1}{3}\sum_{i=1}^{n} f_i(\varepsilon_i - \varepsilon_b)\sum_{k=1}^{3}\frac{N_{ik}}{\varepsilon_b + N_{ik}(\varepsilon_i - \varepsilon_b)}} \tag{38}$$

where ε_b and ε_i are the relative permittivities of the base dielectric

i-th type of embedded particles

f_i is the volume fraction of each embedded particles

N_{ik} are the depolarization factors of every inclusion that characterize their geometry

For the case of only one kind of embedded and spherical particle ($N_{ik}=const=1/3$) equation (38) is reduces to:

$$\varepsilon_{eff} = \varepsilon_b + \frac{f_i \varepsilon_b (\varepsilon_i - \varepsilon_b)}{\varepsilon_b + \frac{1}{3}(1 - f_i)(\varepsilon_i - \varepsilon_b)} \tag{39}$$

with the complex relative permittivity of the inclusions

$$\varepsilon_i(j\omega) = \varepsilon_i' - j\varepsilon_i'' = \varepsilon_i' - j\frac{\sigma_i}{\omega\varepsilon_0} \tag{40}$$

where σ_i is the bulk conductivity of the embedded (the real part is supposed to be much smaller than the imaginary part $(\varepsilon'_i << \sigma_i/\omega\varepsilon_0)$ [47]).

The Neelakanta formula [48] is another method of calculating the complex permittivity and conductivity of a conducting/dielectric mixture. The effective conductivity can be estimated from

$$\varepsilon_{eff}(j\omega) = \varepsilon_{eff}' - j\varepsilon_{eff}'' \tag{41}$$

with

$$\varepsilon_{eff}' = \left\{\frac{\varepsilon_b}{1 + (\varepsilon_b - 1)^{1/3..6}}\right\}\left\{\left[\left(\frac{\sigma_i}{\omega\varepsilon_0}\right)^{f_i}(\varepsilon_b - 1)^{(1-f_i)}\cos\left(\pi f_i / 2\right)\right]^{1/3..6} + 1\right\} \tag{42}$$

$$\varepsilon''_{eff} = \frac{\sigma_{eff}}{\omega \varepsilon_0 \varepsilon'_{eff}} \tag{43}$$

$$\sigma_{eff} = (\sigma_i - \sigma_b)\left\{\left[\frac{\omega\varepsilon_0(\varepsilon_b - 1)}{\sigma_i}\right]^{(1-f_i)} \sin\left(\pi f_i / 2\right)\right\}^{1/3} + \sigma_b \tag{44}$$

To calculate the effective electromagnetic properties of the conductive/dielectric composite, the Bruggeman's formula is helpful. For spherical, conductive embedded particles in a dielectric matrix, the effective permeability can be calculated as [49]

$$\frac{\mu_i - \mu_{eff}}{\mu_i - \mu_0} = (1 - f_i)\left(\frac{\mu_{eff}}{\mu_0}\right)^{1/3} \tag{45}$$

or

$$\mu_{eff} = \left[\frac{1}{6}\left(108\mu_i + 12\sqrt{12b^3 + 81\mu_i^2}\right)^{1/3} - \frac{2b}{\left(108\mu_i + 12\sqrt{12b^3 + 81\mu_i^2}\right)^{1/3}}\right]^3 \tag{46}$$

with

$$b = (1 - f_i)(\mu_i - 1) \tag{47}$$

The permeability μ_i of particles is necessarily the same as the permeability of the initial bulk material; therefore, α_{cor} is defined as a correction factor that is implemented as the ratio between average distance between neighboring particles in the powder and average diameter of the particles. The resulting permeability is approximated by:

$$\mu_i \approx \frac{\mu_{bulk}}{1 + \alpha_{cor} \cdot \mu_{bulk}} \; for \; \mu_{bulk} >> 1 \tag{48}$$

$10^{-5} < \alpha_{cor} < 10^{-2}$ [50] and the exact value for this study should to be estimated.

Chapter 2 Materials and Fabrications

In this chapter, the materials and process of fabrication are explained. Also, the reasons for the selection of ferromagnetic particles of iron, cobalt, nickel and iron oxide particles are presented. Following, explanations regarding the different methods of production of metallic nanoparticles are presented.

The detailed information regarding the purchased particles and their compositions is presented. Moreover the complete clarifications regarding the fabrication process of nanocomposites, as well as the results of analysis, are given.

Verification is done at each step, including observation of the fabrication process and checking the accuracy of information provided by suppliers. Finally, the details of the used equipment in this work and the test procedure used for electromagnetic characterizations of nanocomposites are provided. In Appendix A, more explanation on improving the conductivity of composite by metallic nanoparticles is presented.

2.1 Metallic Nanoparticles

Recently, due to possibility of producing ferromagnetic nanoparticles, research on these particles has become of a great interest. Magnetic nanoparticles are becoming more and more popular due to their enormous applications: magnetic fluids [51], catalysis [52], biotechnology [53] magnetic resonance imaging [54], and data storage, which is currently the largest commercial application of iron nanoparticles. Here, a quick review of different methods of particle production is presented, Followed by more details about the magnetic properties for EM shielding.

2.1.1 FABRICATION METHODS FOR METALLIC NANOPARTICLES

Here, the classification of techniques to synthesize nanoparticles based on their processing routes is realized. Gas, liquids and solid are the main categories selected in this work. The gas category contains many methods:

- Physical vapor deposition (PVD)
- Chemical vapor deposition (CVD)
- Aerosol processing

The liquid category includes other technologies:

- Electrochemical discharge process
- Sol-gel process
- Wet chemical synthesis

Finally, in solid category, the following methods of fabrication are considered:

- Mechanical alloying/milling
- Mechanochemical synthesis

Because of the importance of particle production for EM shielding for each category, different methods are investigated and presented in this work. At the Technical University of Delft (Nanostructured Materials, Delft ChemTech, laboratory of Prof. Schmidt-Ott), spark discharge generation is being investigated for the gas category. At Concordia University, the Electrocatalytic Green Engineering Group investigated the method of electrochemical discharge generation for the liquid category (as well as chemical reactions for producing particles at Prof. Mulligan's lab). Also, the electrodeposition process is being studied for the liquid category at the University of

Montreal (laboratory of Dr. Rochefort). For the solid category, mechanical alloying is being looked into at the SPEX CertiPrep company.

2.1.1.1 LIQUID CATEGORY - ELECTROCHEMICAL DISCHARGE

High-purity, homogeneous, and nanosized metal particles can be prepared via liquid routes. Three methods of electrochemical discharge generation, chemical reaction, and electrodeposition are explained here. Sol-gel also is a popular method for the liquid category, and more explanations about it can be found in [55, 56].

In 1844, Fizeau and Foucault [57] discovered the electrochemical discharge phenomenon, which is now recognized by names like "electrode effects" and "contact glow discharge electrolysis." Guilpin et al. [58], and recently Vogt et al. [59], have conducted systematic studies of the phenomena. The phenomenon has also found to have applications in the machining of glass and other non-conducting materials through the process is known as SACE- Spark Assisted Chemical Engraving [60]. The most important concern regarding this phenomenon is the steady state I-U (current-voltage) characteristics for a two electrodes system in aqueous electrolytes. A schematic of the setup has been given in Figure 15.

In Figure 15-right, the counter electrode is been considered very large compared to the working electrode, and the I-U curve is presented as well. The I-U characteristic shows the current passing through the electrode at a given fixed voltage. The bubbles around the electrode are the main reason that only a mean current is given. This mean

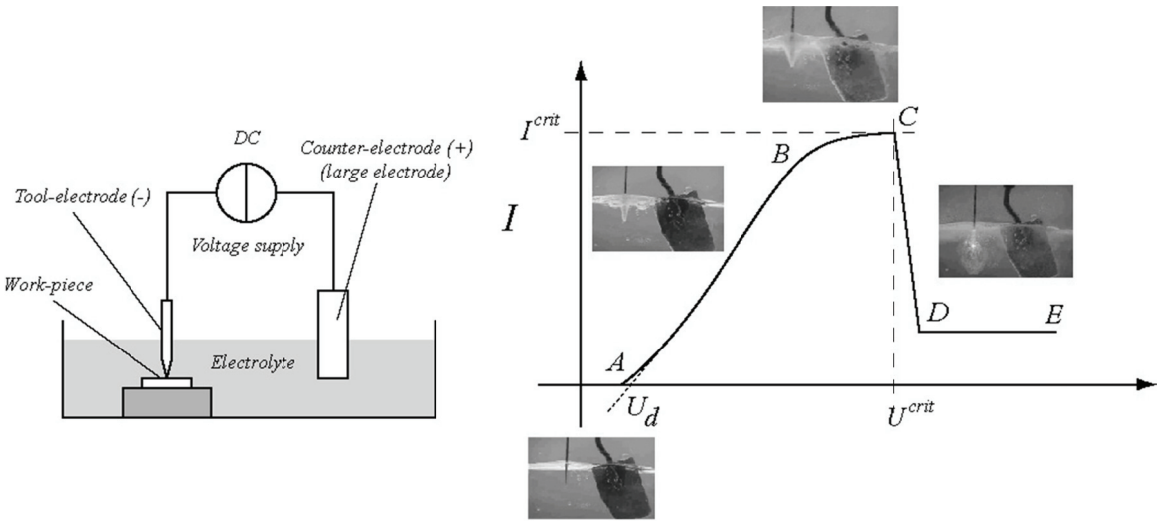

Figure 15 Schematic of the setup for producing electrochemical discharges Right: Typical static Current-Voltage I-U curve for an electrode in aqueous electrolyte

current is the current once the system reaches a steady state (complete formation of the bubble layer). The bubble layer is composed of the adherence region (where bubbles adhere to the electrode surface), a bubble diffusion region (where the bubble concentration is high), and finally the bulk region (where bubbles are quite dispersed). Voltage smaller than decomposition potential U_d, are called thermodynamic and over potential region. The region AB is called the ohmic, BC the limiting current region, CD the instability region (C is a critical point with Critical voltage U^{crit} and critical current of I^{crit}), and finally DE is the spark region.

In an aqueous electrolytes containing metal ions, large cathodic potential is applied to the working electrode. Large current densities (j=1A/mm^2 at U=20V) lead to the formation of a gas film around the electrode. Electrical discharges are created across the film, which lead to the formation of metal nanoclusters (typically 10-150 nm), see Figure 16.

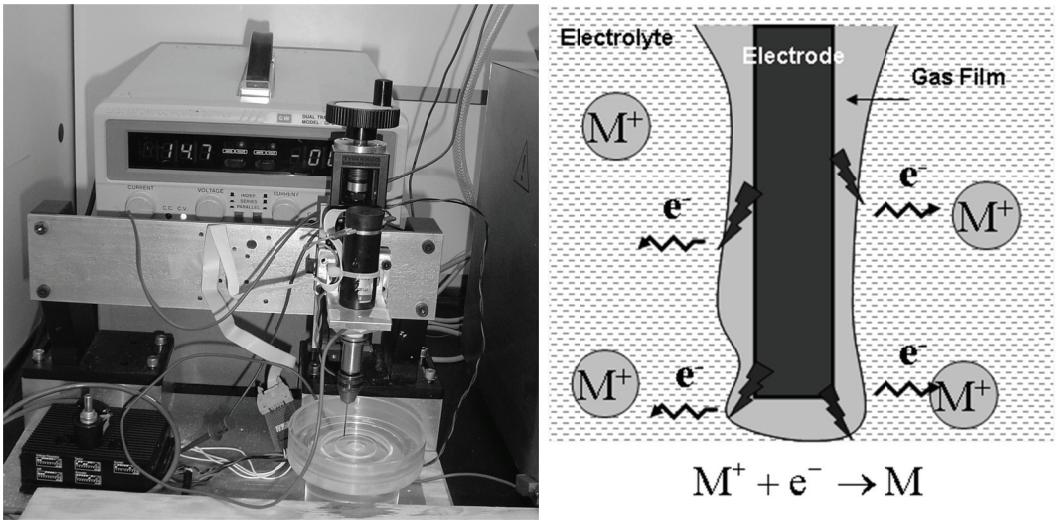

Figure 16 Setup to fabricate nanoparticle (left), Schema of creation of metallic nanoparticle inside solution (right)

Two electrodes of metal (e.g. nickel) are dipped into an electrolyte (typically 3M H_2SO_4 and 1mM $NiSO_4$). When the applied voltage is higher than a critical value (typically around 30V), the bubbles grow so dense on the electrode surface that they coalesce into a gas film. Electrical discharges occur between the electrode and the electrolyte. Nanoparticles of metal (e.g. nickel) would be produced inside the solution based on conditions local to the:

- Locally increasing of ph
- Having high temperature close to electrode
- Existing of strong stirring
- Occurrence of short bursts of discharges across the gas film

The exact mechanism of nanoparticle synthesis by electrochemical discharge phenomenon has still to be described, but the following mechanism is believed to take place. Most of the current is used for H_2 evolution, but a part of current reduces M+ to M. The created M particles would be grouped to form clusters (see Figure 19, right). The

clusters are prevented from depositing on the electrode surface by the gas film. In Figure 17, a transmission electron microscope (TEM) image and an energy-dispersive X-ray (EDS) spectra of the nickel nanoparticles synthesized by electrochemical discharge is shown to confirm the creation of nanoparticles of nickel through the electrochemical discharge process. The sample used in this characterization has been obtained by pouring the result of the electrochemical discharge process on a standard copper mesh of TEM test. As a result, the ECD setup is a convenient method for fabricating the metallic nanoparticles (e.g. nickel). The details about the integration of ECD for electromagnetic shielding are explained in Appendix A.

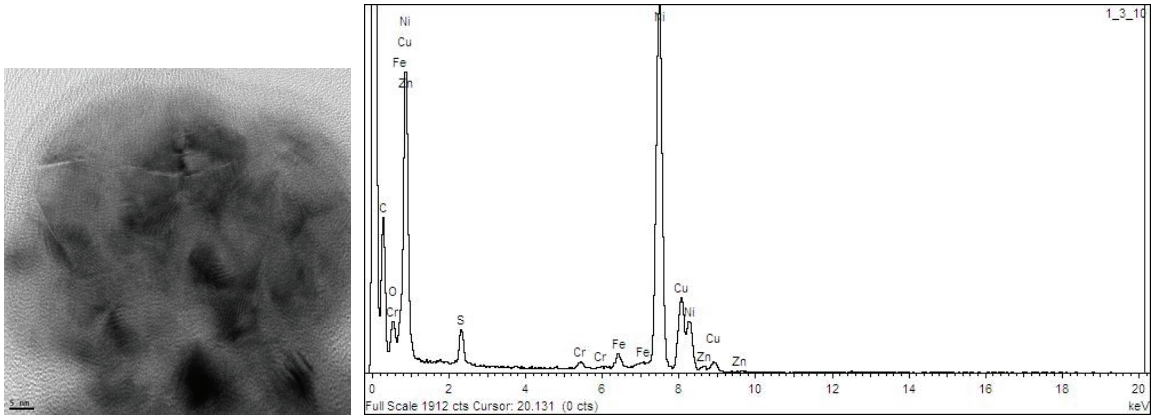

Figure 17 TEM image of Nickel nanoparticles synthesized by ECD (scale 5nm) (left), EDS of Nickel nanoparticles synthesized by ECD (right)

There is also the possibility of creation of carbon nanotubes (CNs), which has been presented in Figure 18. Presently the reason of forming the CNs is under investigation. As the first step, there is the High Resolution TEM microscopy characterization (HRTEM), which should be performed.

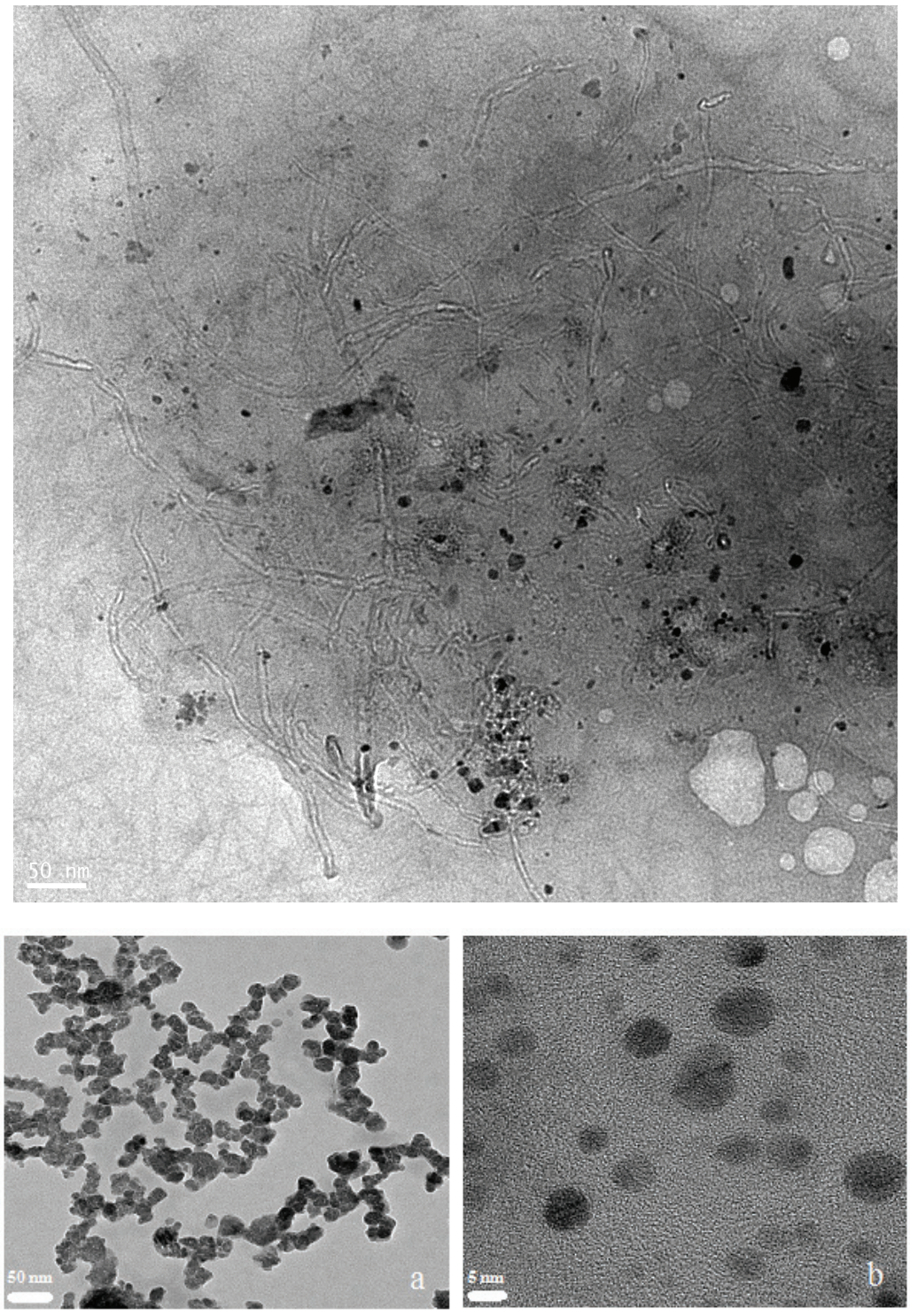

Figure 18 TEM images of creation of CNs on nickel particles (up), Copper (a) and Nickel (b)

2.1.1.2 GAS CATEGORY - SPARK DISCHARGE GENERATION

The most common method used for the synthesis of metal nanoparticles with a well defined and narrow size distribution is inert-gas condensation [61]. Different sources such as evaporation, sputtering, and laser have been adopted to vaporize materials from the surface of solids into clusters [62]. The clusters generated are condensed, transported, and collected on a cold finger. The nanoparticles formed are then in-situ compacted under high vacuum conditions to form a clean bulk nanocrystalline solid. Chemical vapor deposition (CVD) contains the creation of vapor species through the decomposition of gaseous reactants in the area of a hot substrate to form nanoparticles. Thermal, laser, or plasma energies are used for the decomposition of gaseous reactants [63]. In aerosol processes, the liquid would be converted to the vapor phase followed by condensation into droplets. These methods can be used to produce different types of metallic powders [64, 65, 66, 67]. Based on the work that is done in this thesis, the following explanations regarding the spark discharge generation are presented.

The process of spark discharge is initiated by gas breakdown and the formation of a conducting channel, and dissociation and ionization of the gas molecules within a very short time (Figure 19). The plasma channel then thermally expands and a shock wave is formed. In the final stage, charge carriers recombine, the plasma cools, and the shock wave is attenuated to a sound wave [68]. The rapid discharge consists in a current associated with a high temperature (typically 20,000 K). Electrode material is evaporated in the surrounding area of the spark. This is followed by rapid cooling, primarily directed by adiabatic expansion and radiation and below the evaporation temperature dominated by thermal conduction. Because the vapor cloud is small compared to other evaporation-

condensation processes, the cooling period below the boiling point is comparatively fast, and high a concentration of very small particles forms. The generator, which is shown in Figure 19, consists of a chamber about 300 cm^3 in volume, in which two opposing cylindrical electrodes are mounted at a modifiable distance. The electrodes are 3–6.35 mm in diameter, and the gap between them is adjustable from zero to a few millimeters. They are connected to a high voltage power supply, and parallel to a variable capacitor with a maximum capacitance of 20 nF. A high voltage probe connected to an oscilloscope is used to record the voltage across the spark gap during the discharge. The power supply delivers a constant current, periodically recharging the capacitor after discharge has occurred at the breakdown voltage. The current of gas containing the nanoparticles is conducted into a duct and a filter to collect the particles (see Figure 20). The details regarding the integration of spark discharge generation for electromagnetic shielding are explained in Appendix A. In Figures 21, 22, the different types of particles (silver and alloy of copper/silver) fabricated by this method are presented.

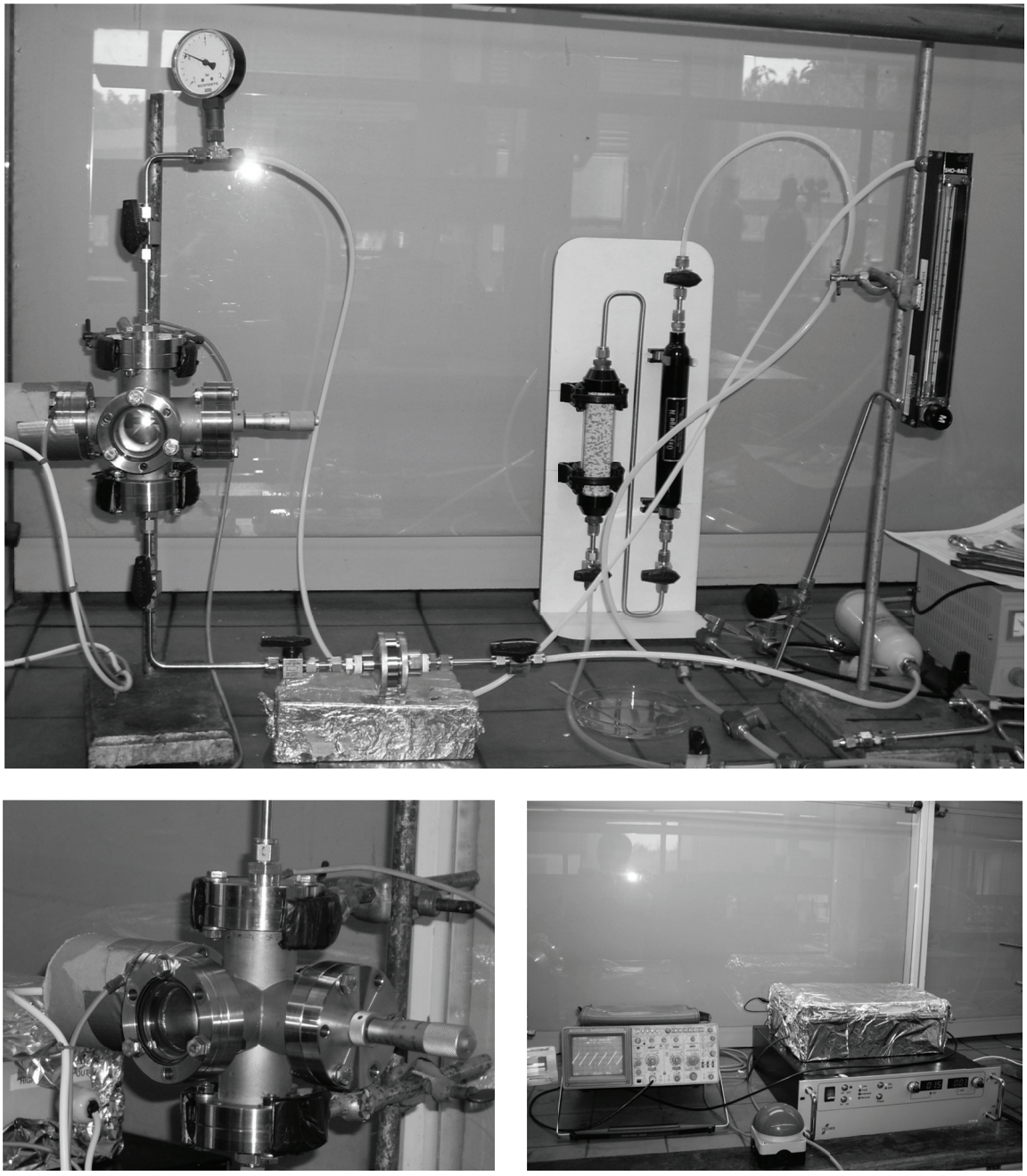

Figure 19 Whole setup for Spark Discharge Generation (up), Combustion Chamber for Spark Discharge (left), Oscilloscope, ON/OFF bottom, Conductance and Power Supply (right)

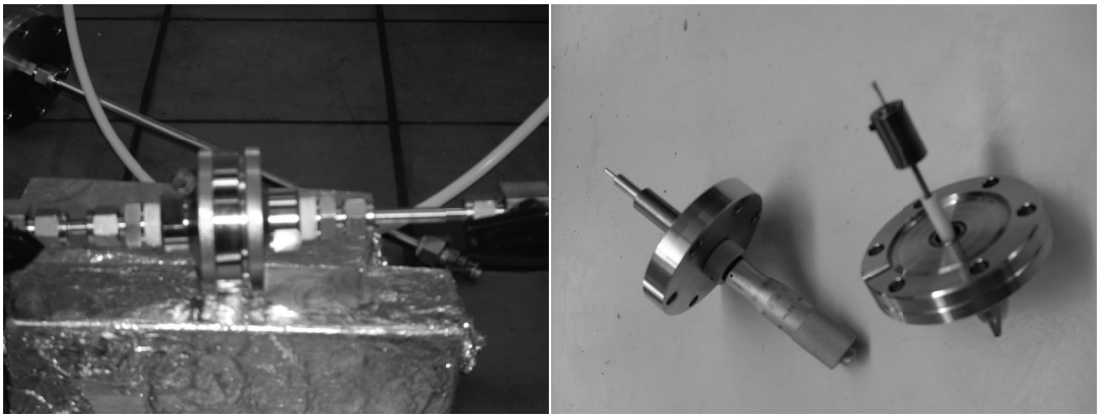

Figure 20 Filter to Collect the Particles (left), Electrode Holders (right)

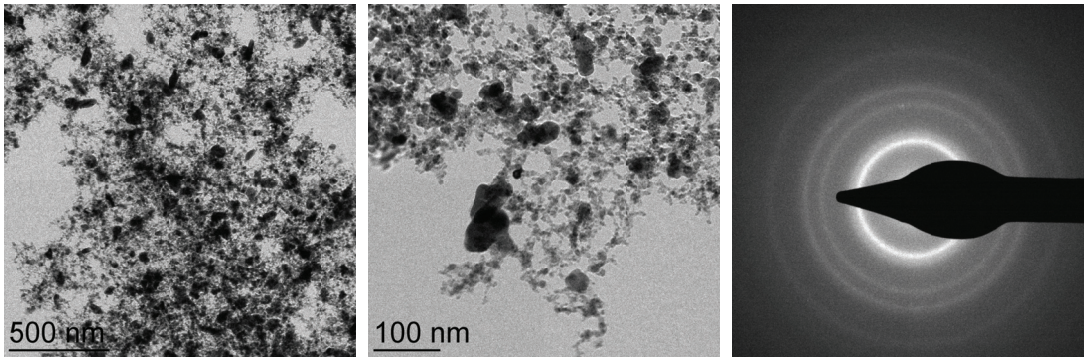

Figure 21 TEM images of Silver/Copper sample

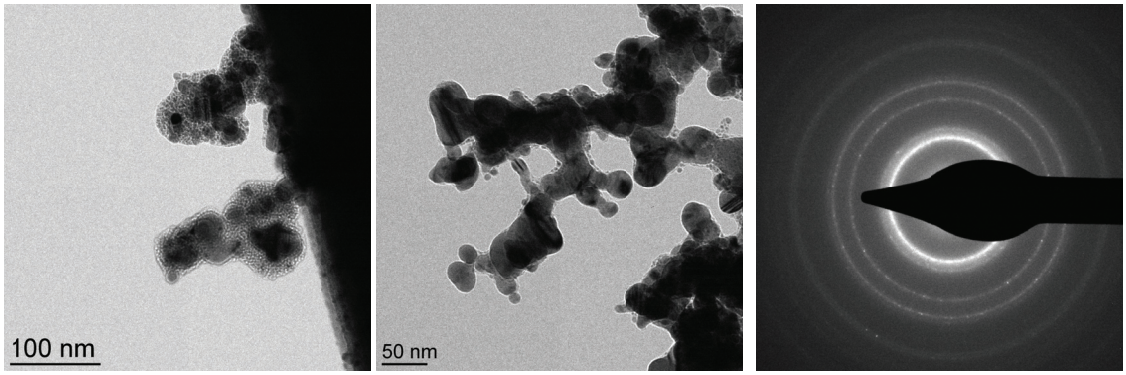

Figure 22 Silver Sample TEM

2.1.1.3 SOLID CATEGORY MECHANICAL ALLOYING/MILLING[i]

The above techniques involve the accumulation of clusters of atoms in the vapor or liquid phase, and their following condensation to form nanoparticles. However, a solid state route such as mechanical alloying/milling produces its nanostructures not by cluster assembly, but through the structural decomposition of coarser grained structures as a result of severe plastic deformation [69]. It is potentially a method of producing powders with a broad range of chemical composition and structure from the amorphous, inter metallic, supersaturated solid solution to nanocrystalline phases. The main problems of mechanical alloying are contamination and grain growth of the powders during processing [70]. The advantage is a broad range of chemical composition. The disadvantages are contamination and grain growth of the powders during processing. Bringing the particle to micro-size, and later to nano-size, would take time and money. Here, ideas and initial test results are presented to decrease the cost of the mechanical alloying process.

The method of mechanical milling/alloying is an established technique for the fabricating of nanoparticles. During the process, raw powder particles experience severe plastic deformation, undergoing a repetitive cold welding and fracturing mechanism. To perform mechanical alloying/milling, there are different mechanisms:

- Vibratory mill
- Planetary mill
- Uniball mill
- Attritor mill

Reaching the final particles through this process takes time and money. The proposed idea in this work is based on using the waste of micro electro discharge machining (micro-EDM) machines. Following the process of micro-EDM, the waste contains the microparticles. By taking these particles into the milling/alloying process, the desired nanoparticles are obtained with less cost and more rapidly:

- The milling machine would just reduce the size of particle from micro to nano instead of from bulk to nano.
- There is no charge to use the waste, and consequently the charge of primary materials needed for the process would be for free.

Currently this research is at a lab-level scale. Typical achieved yields are 10gr of nanoparticles in 20h. However, by overcoming existing challenges, there could be a savings of 10,000kg/year of EDM waste into the environment. Also, providing a cheap nanoparticles to the market would be possible [71].

In Figure 23, a SEM image and an energy-dispersive X-ray (EDS) spectrum of this waste is shown. Typical grain size is in the range of 50 μm. In Figure 24 (left), an industrial μ-EDM used by Philips is shown.

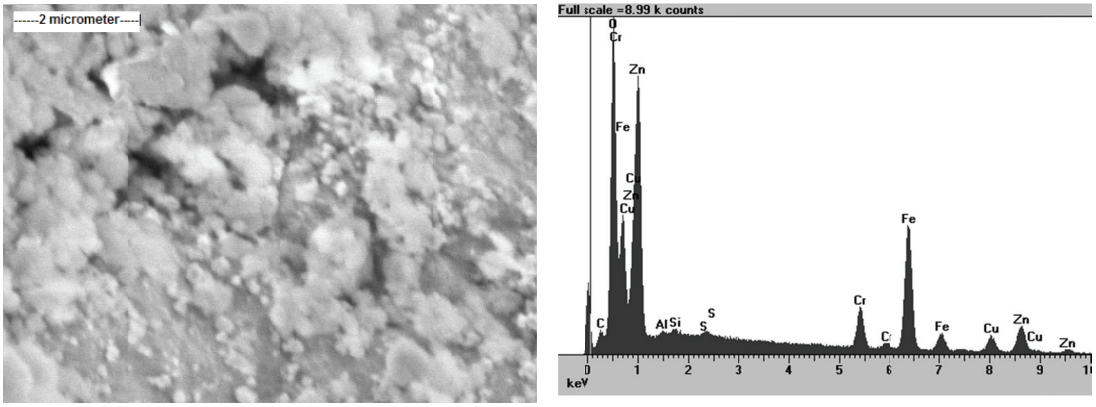

Figure 23 (left) SEM image of μ-EDM waste, (right) EDS spectrum of μ-EDM waste

Figure 24 (left) Massive micro-EDM (with permission of Philips®), (right) SPEX 8000 D Mixer/Mill.

In our research, we propose that the waste be used as an input for the mechanical milling/alloying process to produce particles down to 100nm.

During the mechanical alloying/milling process, the powder will undergo harsh plastic deformation, undergoing a repetitive cold welding and fracturing mechanism. This method is recognized as a flexible process for the fabrication of a broad range of nanocrystalline powders. In this research, the use of the waste as an input for a 8000M mixer / mill (see Figure 24, right) to produce particles down to 100nm is proposed. Two portions of samples of waste are grounded in the SPEX 8000D Mixer/Mill for approximately 800 minutes each. The waste of Micro-EDM is used as a paste, and two portions of approximate 13.8 grams each are taken and placed in 8001 steel vials with two 1/2 inch (12mm) steel balls and approx. 15ml of a grinding aid. Sample A is grounded with denatured ethanol as a grinding aid, and sample B is ground with Vertrel XF as a grinding aid. Grinding time is set at the maximum (99:59, or 99 minutes and 59 seconds) allowed on the conventional timer, and in both cases the sample runs for 10

such runs. As mentioned, the alcohol is more effective for this purpose (see Figure 25). In the case of sample B, Vertrel XF is less effective in rinsing, and the sample is allowed to dry to make it easier to recover. Vertrel XF is used as it is chemically inert for almost all samples, prevents sample particles from sticking to each other or the vial and grinding balls, and usually evaporates rapidly after grinding. However, in this case, the sample paste and Vertrel appeared immiscible, or only partly miscible, when inspected after the first 100 minutes of milling. Furthermore, alcohol does not tend to evaporate during milling, and Vertrel can evaporate, changing the viscosity and other properties of the sample if the vial is not tightly sealed.

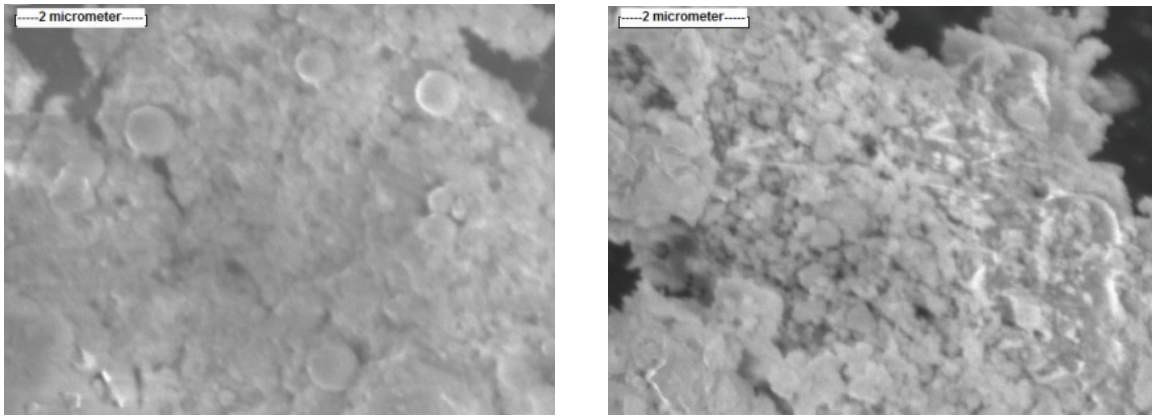

Figure 25 SEM of sample A grounded with denatured ethanol (left), SEM of sample B grinded with Vertrel XF (right).

The utilization of denatured ethanol used as grinding aid in the milling process results in particles less than 100nm and also less amorphous compared to Vertrel XF. The initial sample, as well as two treated samples (A and B), are all rich in iron, chrome, zinc, copper, as well aluminum and titanium. The process doesn't seem to significantly change the chemical composition of the resulting nanoparticles. The sample B (grinded with Vertel XF) seems to have a higher iron content compared to sample B and the EDM

waste. Further investigations are needed to determine if the utilization of Vertel XF favors the formation of iron nanoparticles. The presence of oxygen in all samples is certainly related to surface oxidation of the metal particles. In the case of iron, this oxide is highly magnetic, and particles have the tendency to attach to each other. The undergoing research is at laboratory scale with a batch production of 10gr for 20h. For industrial production, more sophisticated milling machines would be needed.

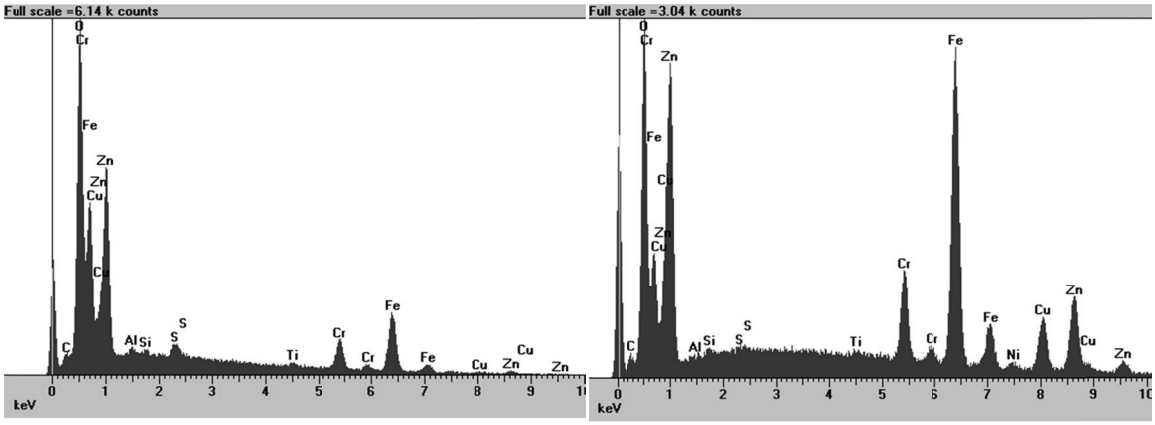

Figure 26 (left) EDS spectrum of sample A grinded with denatured ethanol (right). EDS spectrum of sample B grinded with Vertrel XF

Also, selecting the appropriate surfactant during the milling/alloying process in order to control the particle size is a key factor. As shown in the above figure, the EDS analysis of the samples shows that the result of the process is quite rich in different transient metals.

2.1.2 MAGNETIC PROPERTIES OF METALLIC NANOPARTICLES

Composites containing metallic magnetic particle filler have certain advantages:

- High saturation magnetization
- Tunability of magnetic permeability by controlling the volume fraction of metallic particles

- Mechanical flexibility of the host material of the composite

As bulk material, there is a long list of ferromagnetic materials, the primary ones of which are as follows:

- Chromium dioxide or chromium(IV) oxide
- Cobalt
- Dysprosium
- Ferrite (iron)
- Ferrite with iron(III) oxide (Fe_2O_3)
- Gadolinium
- Gallium manganese arsenide
- Iron
- Magnetite
- Neodymium magnet (NdFeB, NIB)
- Nickel
- Permalloy (a nickel-iron magnetic alloy)
- Rare-earth magnet (alloys of rare earth elements)
- Samarium-cobalt magnet
- Suessite (rare iron silicide mineral with chemical formula: Fe_3Si
- Yttrium iron garnet (YIG) is a kind of synthetic garnet, with chemical composition $Y_3Fe_2(FeO_4)_3$, or $Y_3Fe_5O_{12}$)

As was mentioned in the previous chapter, the loss mechanism for magnetic materials is based on hysteresis, domain wall motion, eddy current, and ferromagnetic

resonance. In the case of microwave frequencies, only the last two remain as the others are comparatively low frequency phenomena. By switching from bulk to nano, the exchange interaction has to be considered. Because of the changing of the magnetic loss mechanisms for nanoparticles, the bulk materials with higher magnetic loss do not necessarily provide the same performance as their nano form. Iron, nickel, and cobalt as nanoparticles are considered as the selected materials in this work for EM absorption due to their higher magnetic loss. These metals exhibit relatively high permeability μ_r (*250*, *600* and *5000*, respectively) and cause a high magnetization in an electromagnetic field.

It should be mentioned that iron (particularly in nano form) also has very high reactivity to water and oxygen. Hence, without protection, oxidation happens easily. That is why commercial iron nanoparticles can have an iron-core, iron oxide-shell forms. On the other hand, iron oxide (e.g., Fe_3O_4) has a high stability against oxidization, and consequently is not complicated to manipulate. So, even if it has a relatively low magnetic loss and permeability (25), it is still accepted for use, and it is considered as one of the selected materials for the investigation of electromagnetic absorption in this work.

By recalling equation 27 from Chapter 1, the critical diameter for the materials applied to composites is listed below [72]:

Table 1 Critical diameters for single domain state

	Iron Fe	Iron Oxide Fe_3O_4	Nickel Ni	Cobalt Co
d_C [nm]	55	128	15	7

2.1.3 METALLIC NANOPARTICLES CONSIDERED FOR EM SHIELDING

Following the prevoius section, two factors—particle size and type of particle—are considered as the main subjects of investigation for improving the absorption capabilities of composites containing metallic nanoparticles (iron, cobalt, nickel and iron oxide). Commercial availability and the need for a considerable amount of particles for this research are the main reasons for using the accessible particles on the market. Also, this project may potentially be applicable in industry, and as a result, using commercial particles would accelerate integration of this technology in industry. To study the effect of size, the focus is to find the particles with minimum size that can provide the maximum shielding effectiveness. Critical diameter (explained in Chapter 2) is considered as the main lead in finding the optimum size of the particle for shielding. Here, the available particles with a size lesser, equal to and greater than the critical size are considered and purchased. Iron and nickel are considered for investigation of the size effect based on their higher magnetic properties, as well as availabilities in the market.

Table 2 Purchased nanoparticles for determination of material effect

	Iron Fe	Iron Oxide Fe_3O_4	Nickel Ni	Cobalt Co
Particle size [nm] (Information by supplier)	25	20-30	20	25-30

The above table illustrates the sizes of the different purchased nanoparticles so as to estimate the effect of different metallic materials. The particles are all purchased from

the same supplier (Sky Spring Nanomaterials. Inc. [Houston, USA]) and consequently the results are comparable (fabrication and manipulation). Based on supplier product information, particles are all spherical with purity of 99.8%. Laser evaporation is the method that is used to manufacture the particles. Particles are received in the form of 5-25gr packages of black powder (partially passivated to any manipulation). To study the size effect, different nanoparticles of iron and nickel were acquired (sizes of particles are shown in Table 3).

Table 3 Purchased nanoparticles for determination of size effect

	Iron Fe			Nickel Ni		
d_C [nm]	55			15		
Particle size [nm] (Information by supplier)	25	40-60	60-80	<15	~15	>15

2.2 Composition of Nanocomposites

With the aim of EM shielding, particles can be hosted in different parts of composites. Here, the simple case of mixing particles with polymer phase (Epoxy) is investigated. In next chapter, particles are introduced to the polymer phase of polymer matrix composite (PMC) with carbon fibers. Here, the effect of adding particles (size and type) on EM absorption is studied. To keep the advantage of the low weight of composites over metallic parts (e.g. aluminum), the volume fraction of particles should

be kept as low as possible. It's proven that even a very small amount (5% and 30%) can improve the shielding effectiveness [73].

Improving the absorption level of composites by metallic nanoparticles is the main goal of this project. There is a limit to the amount of particles inside a matrix called the "percolation limit," and above this limit there will be agglomeration of particles and increasing conductivity and reflection of the composite (explained in Appendix A). However, here, the amount is kept low to provide the maximum absorption and minimum reflection. The dielectric properties, and as a result percolation threshold, depend only on the volume fraction and not on particle size [74].

A statistical model that assumes site or bond percolation in the lattice coordination has been developed by several investigators [75, 76]. For this work, experimental values for the percolation threshold are considered. For nickel and Fe_3O_4 nanoparticles, values of volume fractions without rising of percolation are exposed. The effects are demonstrated through a hardly falling or even rising volume resistivity of the particle/polymer composite up to exact values obtained at 10.27vol% for nickel and 5.79vol% for Fe_3O_4, respectively [77]. For cobalt and iron, proper values are not available, though lower values than 5.79vol% are not expected. To stay below the percolation threshold for all materials, a volume fraction of 4% is considered for nanoparticles inside the composites. Even if it is not a part of objectives of this project, just to conclude the effect of increasing of volume fraction, samples with 20% volume fraction of iron and Fe_3O_4 nanoparticles are fabricated.

Adding a silane based coupling agent to the composites extensively increase the homogeneous distribution of particles in the matrix of epoxy [78]. Electrical and flexural

properties of the composites are enhanced by homogeneous particle distributions in treated composites. The coupling agent has a structure with two different functional groups, one, which is attracted to the resin and the other one, which is attracted to the surface of the filler. APTES (3-aminopropyl triethoxysilane) is the coupling agent that is used in this work. It is purchased from Sigma Aldrich, Inc. (St. Louis, USA). As it is found out to be the most recommended [78] with a weight ratio of 1/10 (coupling agent/particles).

Chloroform, with a volume ratio of 1/10 (solvent/sample) is used as a dispersing agent for the particles in the mixture. Chloroform evaporates entirely during the mixing process (including mixing under vacuum), and as a result it will not stay in the composite and should not be considered in estimation. Epon^{TM} Resin 828RS (epoxy) and Epikure 3046 (curing agent) are two components of the epoxy resin system (matrix of nanocomposite). Based on the supplier's instructions, the weight ratio of 2/1 (curing agent/epoxy) is used. Densities and weights or volume ratios for the different components of the nanocomposites are summarized in Table 4.

Table 4 Material information for composite composition

	Cobalt (fcc)	Nickel	Iron	Fe3O4
Density [g/cm³]:	8,90	8,91	7,87	5,18
Vol. fraction of sample [%]:	4	4	4 (20)	4 (20)

	Epoxy	Coupl. Agent	Curing Agent	Chloroform
Density [g/cm³]:	1,16	0,93	0,95	1,48
Weight fraction of Epoxy [%]:			50	
Weight fraction of particles [%]:		10		
Vol. fraction of sample [%]:				10

The ingredients and weights for the mixtures are estimated to make sure 4% volume fraction of particles (samples of 20% volume fraction for iron and Fe_3O_4 as well) is obtained. Also the required amounts of epoxy/agents for a sample size of 6cm*4cm*0,1cm (W*H*T), that gives the total volume of 2,4cm³ for each sample is considered. If the thickness of structural composites of aircraft is higher than 1mm (2-5mm), the thickness will be enough to investigate the effect of nanoparticles on EM absorption.

Table 5 Weight composition for fabrication of nanocomposites

	Cobalt	Nickel				Iron				Fe3O4		Pure Epoxy
Particle size [nm]:	25	20	<15	15	>15	<55	55	55	>55	25	25	-
Particles [g]:	0,85	0,85	0,85	0,85	0,85	0,76	3,78	0,76	0,76	0,50	2,49	-
Chloroform [g]:	0,36	0,36	0,36	0,36	0,36	0,36	0,36	0,36	0,36	0,36	0,36	0,36
Epoxy [g]:	1,62	1,62	1,62	1,62	1,62	1,60	1,20	1,60	1,60	1,62	1,26	1,68
Coupling agent [g]:	0,09	0,09	0,09	0,09	0,09	0,08	0,38	0,08	0,08	0,05	0,25	0,09
Curing agent [g]:	0,81	0,81	0,81	0,81	0,81	0,80	0,60	0,80	0,80	0,81	0,63	0,84
Sum weight [g]:	3,72	3,72	3,72	3,72	3,72	3,59	6,31	3,59	3,59	3,34	4,98	2,97

2.3 Fabrication of Nanocomposites

Before starting to fabricate the nanocomposites, a mold is needed. Here, a silicone rubber mold is prepared. V-330 Mold Making Silicone Rubber by FREEMAN (Ohio, USA) is used with a C-45 hardener as two components of the silicon rubber mold. Properties like high accuracy, high heat resistance, and excellent tear strength and elongation properties are offered by a mold made of silicon rubber. A casting form with negative samples of the desired dimensions is needed and has to be placed to manufacture the silicon rubber mold. The silicone and hardener in a weight ratio of 1/10 (hardener/silicone) are mixed, and then cast into the form (Figure 27). To prevent air enclosures and to ensure accuracy, lower areas are filled first during the casting of the silicone rubber. To create a silicone mold of about 1cm in thickness, the casting form is filled to ensure form stability during the later fabrication and baking processes (Figure 27).

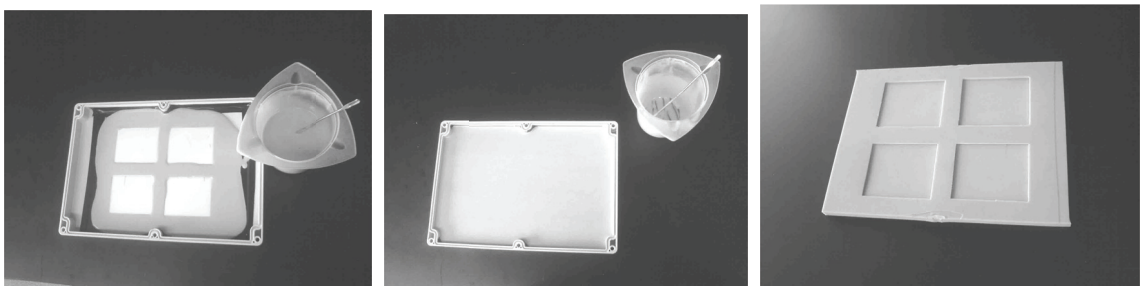

Figure 27 Different steps of mold making

After 24 hours (the needed time for drying/hardening of silicone rubber), the mold can be taken out of the casting form and used immediately for the composite production (Figure 30). To investigate the effect of the type and size of particles, the fabrication of the mold (applied for the set of nanocomposites) will follow the same procedure. The only difference is the different negative samples applied to the casting form.

The metallic nanoparticles are received either in small glass tubes or in plastic bags (shown in Figure 28). For iron nanoparticles (size of 25nm), which are highly reactive, extra care should be taken to avoid unwanted oxidization. During the fabrication process, a special handling is needed which is described later. Figure 28 (right) shows a sample with approximated weight of 1g of Fe_3O_4 nanoparticles not soluble in any kind of solution with very low density ($0.84g/cm^3$).

Figure 28 Nickel nanoparticle from QuantumSphere (left), Fe3O4 nanoparticle (right)

To have a large enough number of samples for testing, the compositions given in last chapter are expected for an amount of four samples for each kind of nanoparticle. Generally, a very small loss of mixture will remain in the beaker as well as on different tools; even so, this amount will ensure at least three samples.

On a laboratory weight (precision of 0.1g, which is zeroed after placing the beaker), the mixture for the nanocomposites are combined in a small glass beaker with following order:

1. The calculated amount of particles is filled in.
2. Chloroform is poured in (on top of the particles), based on the amounts calculated in last section. For small iron particles, the chloroform is injected directly with a syringe into the sealed bag to avoid any oxidation. Knowing the amount of injected chloroform, the exact mass of nanoparticles can be measured and poured

into the beaker. Another possibility would be to re-estimate the composition of the mixture, following the total mass of nanoparticles in the bag. The accurate procedure is dependent on the necessary amount of particles in total and can be chosen on a case-by-case basis.

3. The mixture of chloroform/particle are ultrasonicated for 30s (Figure 32). Agitation in an ultrasonic bath is more effective in dispersing nanoparticles into viscous systems and in dispersing possible agglomerations compared to conventional stirring [79, 80]. The coupling agent and the epoxy resin would be added without delay after the first sonication so as to prevent early evaporation of the chloroform. Mechanical stirring for 10min at 700rpm would continue the process (Figure 29).
4. Following addition of the curing agent, the mixture are mixed mechanically and ultrasonicated again for *10min*. After, they are poured into another a beaker (more suitable for the vacuum mixer). Inside the vacuum mixer (Figure 29), the remains of the chloroform is extracted by alternately operating for a couple of minutes and controlling the remaining weight inside the beaker. The remaining air enclosure is removed from the mixture. Consequently, the mixture can be cast into the silicone mold.

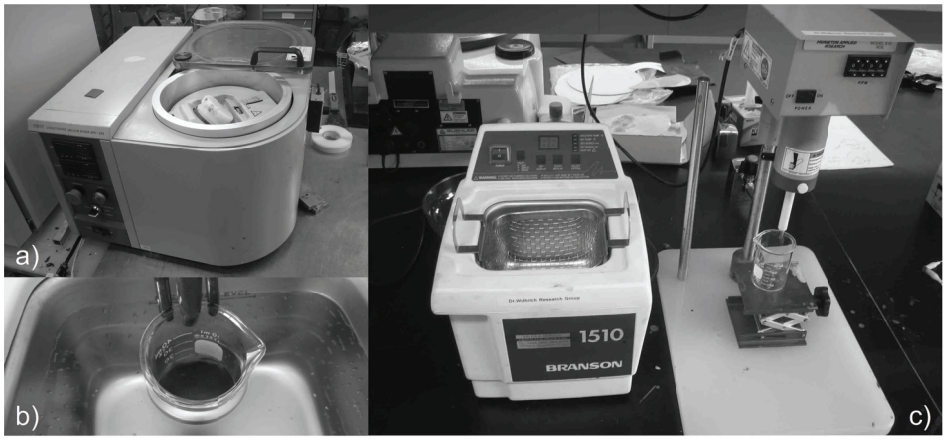

Figure 29 Vacuum mixer (a), solvent/particles in ultrasonic bath (b), mixing equipment (c)

The mixing procedure of the nanocomposites cam be summarized:

1. Chloroform is added to nanopowder in a glass beaker.
2. Chloroform is injected directly into storage bag (in case of highly reactive iron nanoparticles).
3. Mixture is ultrasonicated for 30s.
4. Coupling agent and epoxy resin are added.
5. Mixture is stirred mechanically for 10min at 700rpm.
6. Curing agent is added to the mixture.
7. Mixture is stirred mechanically for 10min at 700rpm
8. Mixture is ultrasonicated for 10min.
9. Mixture is poured into plastic beaker suitable for vacuum mixer.
10. Vacuum mixing and weight controlling are applied so chloroform is totally removed (approx. 5-8min).

The silicone mold with the nanocomposite mixture is left for about 24 hours to degas. Then, the mixture is put into the oven to conclude the fabrication procedure during

the baking process. For the curing process, an unpressurized oven is used, that is carried out in three steps.

First, the oven is warmed up from room temperature to 80°C at a rate of 5°C/min. The pre-curing step happens at 80°C for 2 hours, followed by raising the temperature to 125°C and the post-curing step for 3 hours.

Second, the samples are cooled down to room temperature and taken out of the mold. To avoid any kind of bending during the curing process and cooling period, the silicone mold should be loaded with weights on the edges. The curing process of the nanocomposites can be summarized:

1. Warm-up from room temperature to 80°C at a rate of 5°C/min.
2. Pre-cure at 80°C for 2 hours.
3. Increase the temperature to 125°C.
4. Post-cure at 125°C for 3 hours.
5. Cool down to room temperature.

Figure 30 shows the samples of nanocomposites with added particles of Fe_3O_4, nickel and iron, and a reference sample with just pure epoxy resin. After taking them out of the mold, the samples' side edges are grinded mechanically to have a clean top surface free of burrs. The four holes were drilled for the waveguide's flange for EM shielding tests. The samples are quite fragile, so drilling the holes should be done carefully (so there is no possibility of having a break or crack during manufacturing). In total, twelve different types of nanocomposites are fabricated. With a lot size of three that gives 36 samples.

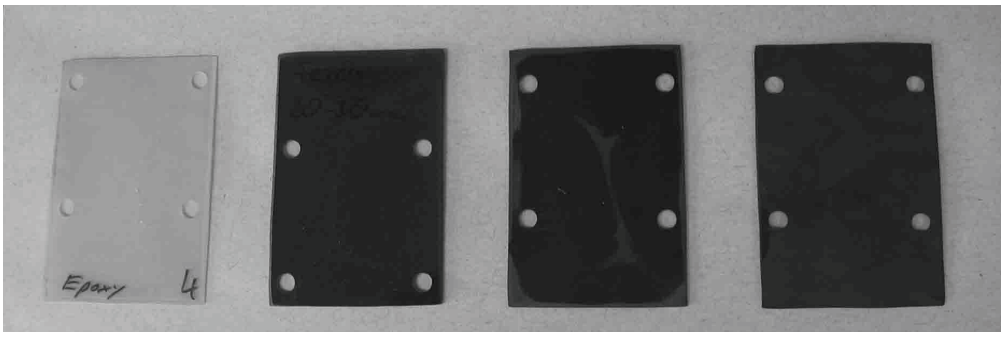

Figure 30 Samples (pure epoxy, with Fe_3O_4-, Nickel- and Iron-filler, left-to-right)

To consider the possibility of improving the performance of fabricated samples, two types of modifications are created during the fabrication process:

Revision 1

1. Powder/slurry mixture of nanoparticles in choloroform solvent quickly stirred by ub for 30 seconds
2. Addition of epoxy resin and coupling agent (10w% of amount of nanoparticles)
3. Mixing by ultrasonic bath for 10 minutes and high speed mixer (19,000) for 10 minutes
4. Addition of curing agent (half weight of resin)
5. Mixing by ultrasonic bath for 10 minutes
6. Curing during night and solvent evaporation
7. Normal curing procedure and curing following conventional procedure

Revision 2

1. Powder/slurry mixture of nanoparticles in ethanol + coupling agent mixed by highspeed mixer

2. Addition of epoxy resin
3. Mixing by ultrasonic bath for 15 min, high speed mixer (11,000 rpm) for 20 minutes
4. Addition of curing agent (half weight of resin)
5. Mixing by ultrasonic bath for 15 minutes
6. Solvent evaporation + curing and mixing under vacuum as well as curing following conventional method

The EM shielding effectiveness of two modified methods of nanocomposite fabrication are presented in next chapter.

Chapter 3 Characterization

In this chapter, different characterization methods are explained. First, different methods of electromagnetic characterizations are explained. The selected method of EM test, and the reasons for selecting this method, are explained. Then, explanations regarding the thermal and mechanical tests as well as the selected ones are presented. At the end of this chapter, the verification methods of fabrication (containing XRD, both optical and SEM microscope) are presented.

3.1 Characterization Methods for EM Shielding

The development of new materials for electromagnetic shielding is of great interest. As mentioned before, the application of composite materials is quite desirable due to their mechanical properties while having low weight and other advantages explained in the previous chapters. Nevertheless, due to the necessity of implementing electromagnetic properties to the fiber/polymer-composite in terms of ensuring the electromagnetic interference shielding (EMIS), additional efforts have to be made to develop a ready-to-use material for aerospace applications. To determine the EMIS properties of shielding materials, technically mature characterization methods have to be found and applied in the correct ways to guarantee accurate predictions, not least with regard to performing obligatory certifications of the potential product.

The shielding effectiveness (SE) describes the performance of the shield and is defined as:

$$SE = 10 \cdot \log_{10} \frac{incident\ \ power\, density}{transmitted\ \ power\, density} = \frac{P_0}{P_S} \tag{49}$$

This expression describes the ratio of measured power before and after the shield is placed in the electromagnetic field, and can also be written as

$$SE_E = 20 \cdot \log_{10} \frac{E_0}{E_S} \tag{50}$$

$$SE_H = 20 \cdot \log_{10} \frac{H_0}{H_S} \tag{51}$$

where $E_{0,S}$ and $H_{0,S}$ are the effective electric and magnetic fields with and without a shield, respectively. In far field conditions (ratio of *E*-field / *H*-field—wave impedance—is constant) and therefore in the applicability of plane wave assumptions, it is $SE_E = SE_H$.

There are different ways to determine $E_{0,S}$, $H_{0,S}$ or $P_{0,S}$. The basic test methods for the shielding effectiveness measurement of a material sample are the coaxial holder method, the dual-TEM cell method, free space measurement in the frequency or in the time domain, and the application of waveguides. There is also a technique called four-point-resistance where the measured surface/volume resistivity of the material is used to calculate the SE. A problem in measuring the square resistance of filled conductive plastics occurs because the conductive filler is not necessarily on the surface of the material, so this method is more useful for homogeneous materials and is not considered further in this work [81].

3.1.1 COAXIAL HOLDER METHOD

The primary, and most often used, measuring method in the controlled medium is the coaxial holder method following the ASTM D4935 standard [82]. This method uses a holder transmission line and a vector network analyzer (VNA), as is shown in Figure 31. The sample is placed and fixed in the coaxial transmission line holder. By measuring the scattering parameters S_{11} and S_{21}—reflection and transmission coefficients—it is possible to determine the contribution of the absorption and the reflection at the total shielding effectiveness.

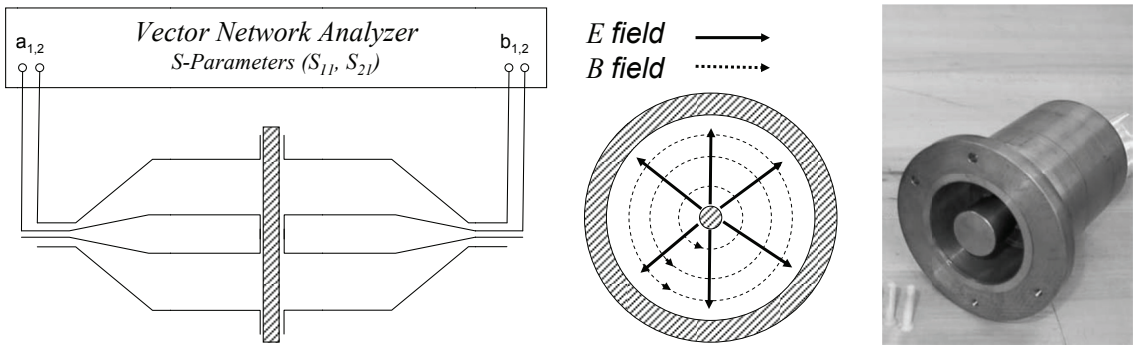

Figure 31 Schematic sketch of coaxial holder, its cross-section and an example

S-parameters describe the response of a 2-port (in this case) network to voltage signals emitted and received at each port. The first number in the subscript refers to the responding port, while the second number refers to the incident port. Thus, S_{21} means the response at port 2 due to a signal at port 1. With the following equations, the shielding effectiveness and its composition can be calculated [83]:

$$\begin{pmatrix} b_1 \\ b_2 \end{pmatrix} = \begin{pmatrix} S_{11} & S_{12} \\ S_{21} & S_{22} \end{pmatrix} \times \begin{pmatrix} a_1 \\ a_2 \end{pmatrix} \tag{52}$$

$$T = |S_{21}|^2 = |S_{12}|^2 \tag{53}$$

$$R = |S_{11}|^2 = |S_{22}|^2 \tag{54}$$

$$A = 1 - R - T \tag{55}$$

$$SE_{R,dB} = 10 \cdot \log_{10}(1 - R) \tag{56}$$

$$SE_{A,dB} = 10 \cdot \log_{10}\left(\frac{T}{1 - R}\right) \tag{57}$$

Due to the occurrence of higher field modes inside the tested material and the coaxial holder at higher frequencies, this method is limited to ~1.5GHz according to ASTM D4935 and in conformity with recent literature [84,85]. The latest research has shown ways to extend the frequency range investigated by the coaxial holder method by up to 18GHz. Therefore, it is required to reduce the diameter of the coaxial chamber to fit to higher cutoff frequencies and smaller wavelengths of the transmission line theory [85]. Another way is presented in [86]: instead of longitudinal flanging of the sample, it is transversally placed in the coaxial holder, and simultaneously a capacitive coupling between measuring cell and the samples is created, and higher modes are therefore prevented while better agreement with physical simulations and theoretical predictions is achieved.

3.1.2 DUAL TRANSVERSE ELECTROMAGNETIC CELL

The Transverse Electromagnetic (TEM) cell is very similar to the coaxial holder, with the difference being that the cross section is now rectangular rather than circular. A dual-TEM cell is therefore simply a pair of TEM cells with the added feature of an aperture in a shared wall. The aperture transfers power from the driving cell fed by a signal generator to the receiving cell with a signal analyzer (Figure 32). The insertion loss provided by putting a sample in the aperture gives an evaluation of the shielding effectiveness of the material. The upper frequency is a function the size of the TEM cell and is commonly limited to approximately 1GHz. A major limitation and problem is the variation in measured data due to contact resistance. Many materials, especially those made from plastic, give large variations in contact resistance. This is also a problem for some other measurement systems.

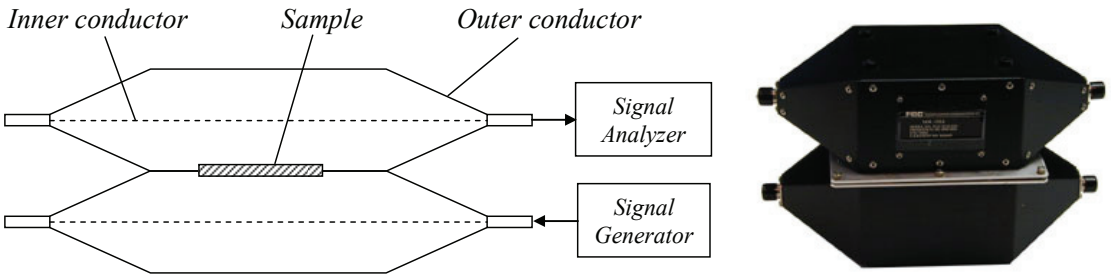

Figure 32 Schematic sketch and representative of the dual-TEM cell [87]

3.1.3 FREE SPACE MEASUREMENT

Derived by the MIL-STD-285 standard [88] and very time consuming and costly, the free-space technique is a method that allows wide frequency range measurements with the upper frequency limit around tens of GHz. Moreover, this method allows the shielding effectiveness measurement for a large sample size. Thus, this electrical contact-

free method is suitable for a large class of shielding and additionally, in-situ measurements become possible.

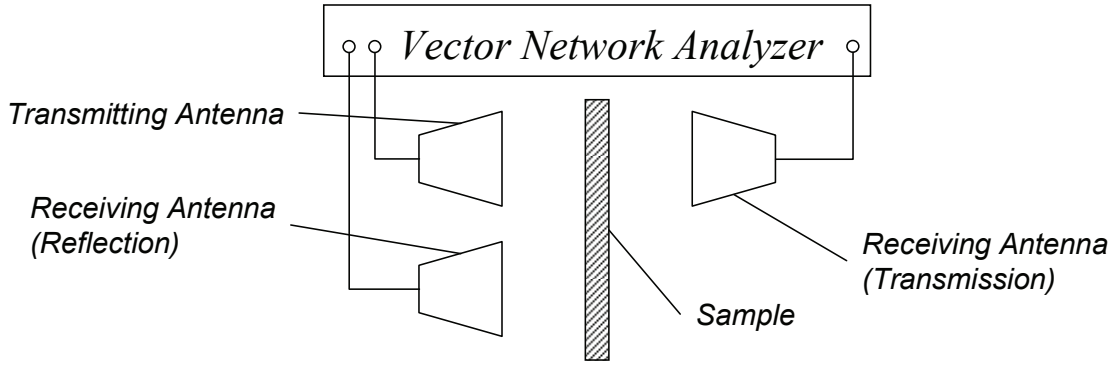

Figure 33 Free Space Measurement setup for frequency domain

Figure 33 shows the main setup of a free space measurement of shielding effectiveness. Depending on the required type of data (reflection or transmission values), the choice of the different receiving antennas must be made. The main difficulties of the free space measured techniques are those related to controlling the electromagnetic environment, consisting of the separation of the desired electric field from perturbing fields.

The free space measurement is usually carried out with a certain frequency-transmitting antenna. On the other hand, the time-domain technique allows separation of the desired signal from the unwanted reflections in the laboratory by using sub-nanosecond pulses whose differences in time arrival at the receiving antenna is measured [89]. Because the shielding effectiveness of the materials depends on the frequency (*SE* is different, depending on frequency component of the field), the shapes of these two pulses, with without and the shield, may be different. The direct difference in spectra response gives the SE value.

3.1.4 RECTANGULAR WAVEGUIDE TEST SETUP

Similar to the test setup for coaxial holder method, the application of rectangular waveguides to channel the electromagnetic plane wave penetrating the sample allows us to determine the shielding effectiveness at higher frequencies and reduce shape complexity of the sample at the same time [90]. The electromagnetic waves in a metal waveguide may be described as travelling down the guide being repeatedly reflected between opposite walls of the guide [91]. When functioning as transmission lines, waveguides are considerably simpler than two-conductor cables—especially coaxial cables—in their manufacture and maintenance. With only a single conductor (the waveguide's wall), there are no concerns with proper conductor-to-conductor spacing. The mode with the lowest cutoff frequency is termed the dominant mode of the guide. It is essential to choose the size of the guide such that only this single mode can exist in the frequency band of operation [92]. Signals are typically introduced to and extracted from waveguides by means of small antenna-like coupling devices inserted into the waveguide (Figure 34).

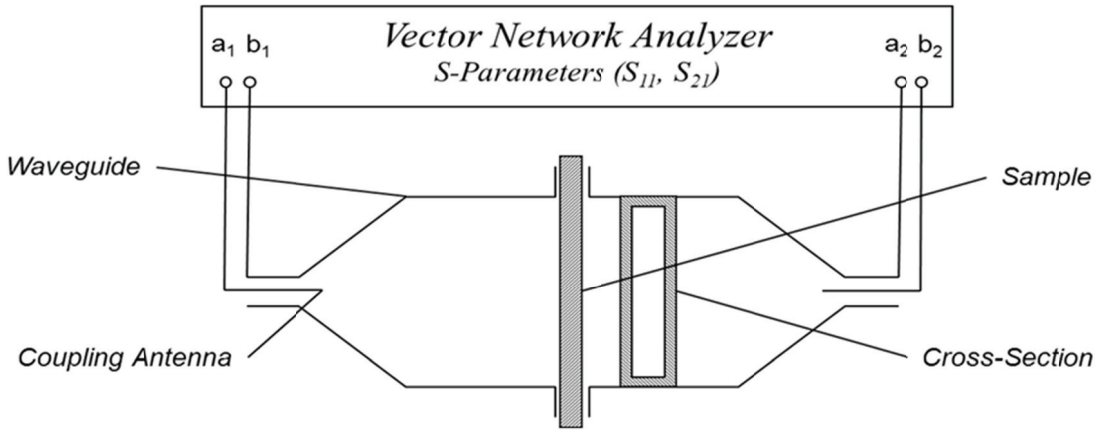

Figure 34 Schematic sketch of rectangular waveguide measuring setup

Just as with the coaxial holder method, the scattering parameters are measured to determine the shielding effectiveness. Due to its ability the deliver proper results for high frequencies as it is necessary in this work, this method is applied for electromagnetic characterization of the nanoparticle/polymer composites.

Rectangular waveguide dimensions are classified through the EIA standard [93]. For any frequency range from 0.32GHz through 325GHz, different waveguides must be applied, and the information can be taken out of a waveguide table [93]. The cross section is dependent on the cutoff frequency's wavelength: for the starting frequency range of 0.32GHz to 0.49GHz, the proper waveguide would be, regarding the WR2300 standard, one with an inner cross section of 23 x 11 inches (WR for Waveguide Rectangular). Another selection would be a waveguide of 3.4 x 1.7 inches (WR340) for a measurement from 2.2GHz to 3.3GHz. For the considered x-band (8.2GHz to 12.4GHz), the inner dimensions of the waveguide are 0.9 x 0.4 inches, which follow the WR90 standard.

Figure 35 shows a typical setup for EM shielding measurements (in the laboratories of the Electrical and Computer Engineering Department of Concordia University), which was used for several rough measurements during the work. In the front of network analyzer the two waveguides are shown, between which the sample is placed. They are connected to a network analyzer with two highly shielded coaxial cables. The network analyzer is controlled digitally by the computer.

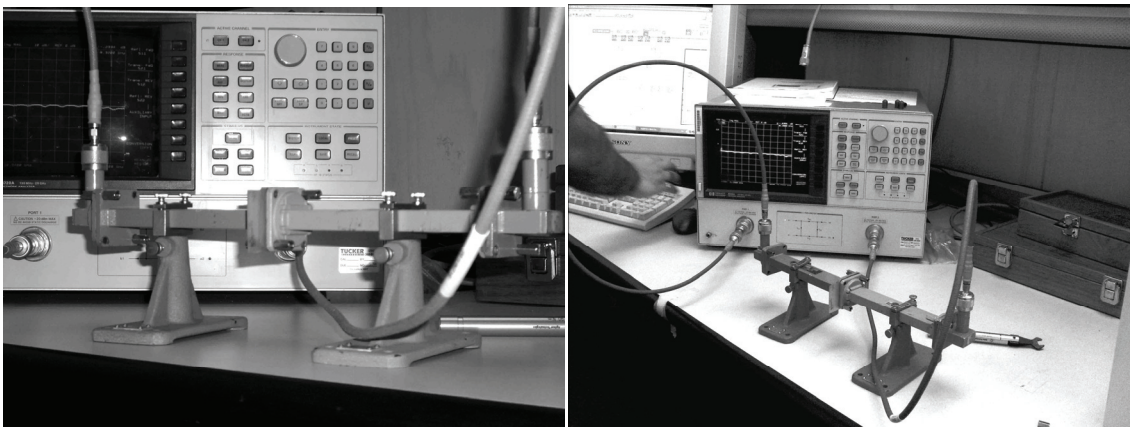

Figure 35 Typical measurement setup for EM shielding characterization

The electromagnetic shielding characterization of the nanocomposites in this work is performed at the Institute of National Measurement Standards, National Research Council (Ottawa). Because of small sample thicknesses and small particle loadings, low values for absorption and total shielding would be expected, and consequently the highest precision would be needed.

Waveguides related to the WR90 standards are used (Figure 36); the electromagnetic fields are generated and recorded by a E8364C PNA Microwave 2-port Network Analyzer (Agilent Technologies, Santa Clara, USA). The setup is calibrated in accord to a thru reflect line (TRL, MTT27-12) calibration standard [94] to cancel out the effects of cables and connectors as well as of the waveguide transition.

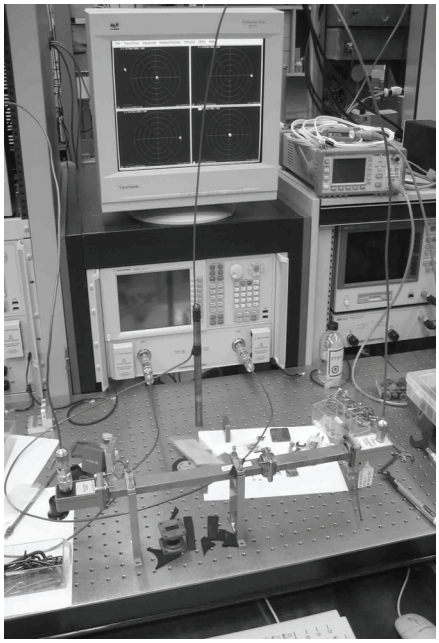

Figure 36 Experimental Setup for shielding measurements at NRC

The nanocomposite samples are placed between the two waveguide flanges as shown in Figure 36. The coaxial cables are covered with copper and are therefore highly shielded. Moreover, because of their sufficient hardness, they can be set around the test setup to prevent any type of interference between the two ports.

Throughout the test, the transmitted and reflected power density is measured through scattering parameters and recorded in relation to the incident power density, as in equations (53) and (54). Absorption would be calculated through equation (55):

$$T = |S_{21}|^2 = |S_{12}|^2 \tag{58}$$

$$R = |S_{11}|^2 = |S_{22}|^2 \tag{59}$$

$$A = 1 - R - T \tag{60}$$

Measuring intervals are every 0.05GHz, giving 85 data points for the considered frequency range of 8.2GHz to 12.4GHz. The measuring precision of the power density ratio is 10^{-9}.

To raise the precision of measurements, reflections and transmissions are recorded in forward and reverse measurements. Therefore, the incident electromagnetic field is penetrating the composite shield from both sides, and data is recorded separately. The average of both measurements of the samples is taken into account to remove deviations of particle concentration in the composite sample.

3.2 Thermal Analysis

There are many different methods that can potentially be used for thermal analysis:

- Differential scanning calorimetry (DSC)
- Dynamic mechanical analysis
- Thermomechanical analysis
- Thermogravimetric analysis (TGA)
- Differential thermal analysis
- Dilatometry
- Optical dilatometry
- Dielectric thermal analysis
- Thermo-optical analysis

In this work, two methods of DSC and TGA are used for the thermal characterization of nanocomposites. The goal is to check to see if adding the particles

changes the thermal properties of the polymer phase. The main goal in this thesis is to verify the electromagnetic performance of nanocomposites with metallic nanoparticles. However, it is particularly important to test on thermal properties and to assure that even if there are some changes, they are negligible.

Thermogravimetric analysis (TGA) is a technique that weights continuously the weight of the sample as a function of temperature (and/or as a function of time) with a controlled temperature program (Figure 37). Controlled temperature can mean the following [95]:

- Heating and/or cooling at a linear rate
- Isothermal measurements
- Combinations of heating, cooling and isothermal stages
- Other, more modern approaches, in which the temperature profile is modified according to the behavior of the sample.

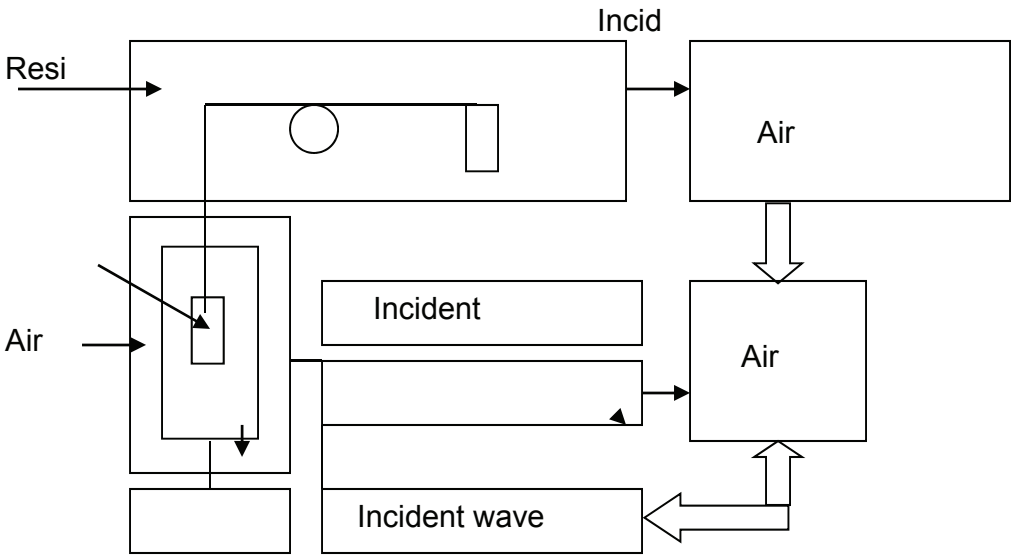

Figure 37 Schema of Thermogravimetric Analysis (TGA)

Instrument (heating rate, furnace atmosphere and flow rate, geometry of the pan and furnace, and the material of the pan) and sample (mass, particle size, sample history, packing, thermal conductivity, and heat of reaction) are factors that affect the result. If the standardization is to be done carefully, the results will be reproducible. Sources of error can be:

- Mass (effect of temperature on balance, convection and/or turbulence, viscous drag on suspension)
- Noisy or variable records can rise from: static, vibration, pressure pulses in lab, uneven gas flow.

Compared to a calorimeter that measures the heat in and out of a sample or a differential calorimeter that measures the heat of a sample relative to a reference, a differential scanning calorimeter does all of the above and additionally heats the sample with a linear temperature ramp (for endothermic, heat flows into the sample, and for exotermic, heat flows out of the sample). Differential scanning calorimetry (DSC) measures differences in the amount of heat required to increase the temperature of a sample and a reference as a function of temperature in a controlled environment. These measurements provide quantitative and qualitative information about the physical and chemical changes that involve the endothermic or exothermic processes or changes in heat capacity.

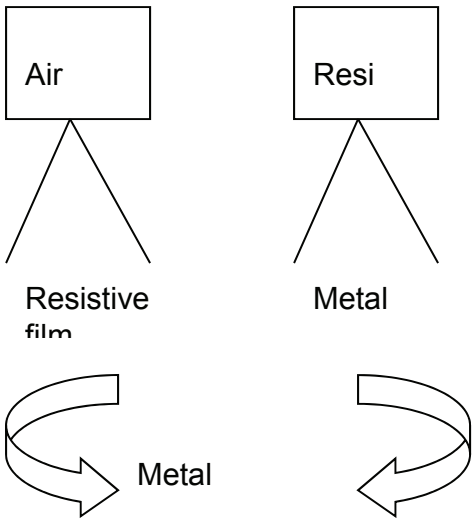

Figure 38 Differential Scanning Calorimetry (DSC)

The instrument is also able to measure glass transitions, melting and boiling points, crystallization time and temperature, percent crystallinity, the temperature of fusion and reactions, specific heat capacity, oxidative and thermal stability, rate and degree of cure, reaction kinetics, and purity. There exist the potentials for errors in calibration contamination, sample preparation (such as how the sample is loaded into the pan), residual solvents, moisture, thermal lag, heating and cooling rates, sample mass, and processing errors [96].

3.3 Mechanical Properties

Mechanical testing of polymer matrix composites (PMCs) is to obtain the parameters such as strength and stiffness. Here, our aim is to show that adding ferromagnetic particles does not have a negative effect on the mechanical properties of the polymer phase. Different mechanical tests for conventional PMCs are presented. A

selection of a test method for a polymer with embedded particles will finish this chapter. Tensile testing uses the classical coupon test geometry with two regions: the central region (gauge length) where the failure is expected to happen, and two end regions that are clamped into a grip mechanism attached to test machine.

The most popular compressive test technique is the Celanese fixture. Cylindrical in design, a small coupon is placed in a set of trapezoidal grips, encased in collars and an alignment shell. The gauge length depends on the type of material and varies between 12.7mm for longitudinal coupons and 6mm for transverse coupons.

The most common test for measuring shear delamination is the short beam shear test. A small specimen (<30mm long) is loaded into the three-point bending until a delamination forms in the center plane at one end of the coupon. This test is difficult to optimize because failure could happen by crushing under the central bending nose. Shear strength is given by three times of applied load divided by four times of coupon width times coupon thickness.

There is also the mode-I delamination in PMCs, which is measured by using the double cantilever beam (DCB) test method, rather than the compact tension test geometry used for the mode-I cracking of most other materials. The coupons are long and thin (normally 150mm x 25mm x 3mm), tabbed at one end with aluminum hinges or “T” tabs and with Teflon insert at the same end in the center plane of the specimen to represent a delamination of known length. The coupon is loaded and unloaded many times after a small increase in crack growth.

Most mode n testing is conducted using the end notch flexure (ENF) test (Mode II fracture toughness). This test uses identical coupons to the double cantilever beam (DCB)

test (minus tabs) and produces shear delamination under three-point bending. The coupon is placed under a compressive load, continuing until the crack propagates.

A very popular test is the asymmetric four points bending test (ASTM D 6272-10, Figure 39) [97]. The coupon is 80mm long; 20mm wide and around 3mm thick. Two notches, 4mm deep, are cut where shown, and application of the load will cause shear failure along the notch roots (axial splits) followed by intralaminar shearing in the center section. Strain gauges are bounded at $\pm 45^{o}$ in the coupon center, enabling accurate shear modulus measurement.

Identifying the flexural property of reinforced polymer with metallic particles and doing a comparison with an unreinforced frame of the Standard Test Method for Flexural Properties of Unreinforced and Reinforced Plastics and Electrical Insulating Materials by Four-Point Bending is been followed in this work.

During this test, the flexural property of a reinforced plastic is determined. The test method utilizes a four point loading system applied to a supported beam.

A bar (rectangular cross section) is loaded at two points (by two loading noses that same distance from adjacent support points) and rests on two supports. One third or one half of the support span would be equal to the distance between the loading noses. The ratio of 16:1 should be used for the support span-to depth.

The specimen is deflected until rupture occurs, or until the maximum strain of 5% is obtained, whichever happens first. Location of the maximum bending moment is the main difference between the 4 points and 3 points bending tests.

A calibrated testing machine that can operate at a constant rate of crosshead motion over the range indicated should be used (the error should not exceed ±1% of

maximum load expected to be measured). The stiffness of the machine should be such that the total elastic deformation of the system does not exceed 1% of the total deflection of the test specimen. The load-indicating mechanism should be free from initial lag at the cross head rate used. The loading noses and support have cylindrical surfaces. To prevent excessive indentation, the radii of the loading noses and supports should be 5.0±0.1 mm.

A calibrated device to measure the deflection of the beam at the common center of the loading span should be used. This device automatically and continuously records the deflection during the test. A micrometer for measuring the width and thickness of test specimen should be used.

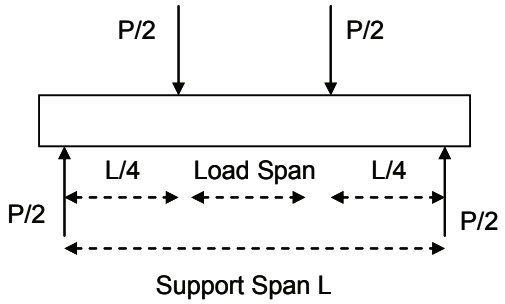

Figure 39 Loading diagram (one half of support span)

The dimensions of the sample are 1.6mm thick, 50.8mm long, and 12.7mm wide tested flatwise on a 25.4mm support span (5 samples have been tested). Regarding the conditioning, the condition is in accordance with Practice for Conditioning Plastics for Testing. Temperature and humidity tolerance are in accordance with section 7 of ASTM D618.

The test measurement is followed by the Test Methods for Physical Dimensions of Solid Plastics Specimens. The loading nose and support are aligned so that the axes of cylindrical surfaces are parallel and the load span is either one third or one half of the

support span. The specimen is centered on the supports with the long axis of the specimen perpendicular to the loading noses and supports. The load is applied to the specimen at the specified crosshead rate and takes simultaneous load-deflection data. The deflection is measured by means of a device under specimen in contact with it at the common center of the span, the device being mounted stationary relative to the specimen support. It should be noted that beyond 5% strain, these test methods are not applicable.

3.4 Verification of Fabrication Procedures

It is required to verify the composition of the fabricated samples with the aim of providing reliable facts for the electromagnetic shielding effectiveness of the fabricated nanocomposites. Here, four different techniques of analysis are presented to provide sufficient information regarding the present nanocomposites, so as to be sure that the volume fraction of metallic nanoparticles inside the composite the weight and volume of each sample is estimated correctly. With the help of both and with the knowledge of all the other component's material properties it is possible to calculate the volume fraction of the particle filler.

X-ray diffraction analysis can be helpful for determining of the type of the applied nanopowders' metallic elements. Also, it can be used to get (through the Scherrer formula) a general idea of the particle sizes embedded into the epoxy resin. Also, at the end, the explanations regarding microscope characterization (both SEM and optical), particularly to define the threshold, are presented.

3.4.1 VERIFICATION OF VOLUME FRACTION

Following the fabrication procedure, with the exception of the dispersing agent (e.g. chloroform), the rest of the materials, including the epoxy resin, curing agent, coupling agent, and metallic nanoparticles, are found in each sample of nanocomposite.

Volume fractions of metallic particles inside the samples can be determined by equation (63) stated below, which can be easily obtained by restating the linear mixing equation (62) considering density ρ_i and volume fraction x_i of each component:

$$W = V \cdot \sum_{n=1}^{i} \rho_i \cdot x_i \tag{61}$$

$$x_P = \left\{ \frac{3 \cdot \rho_{Ep}}{2 + \left(\rho_{Ep} \middle/ \rho_{CuA} \right)} - \frac{W}{V} \right\} \cdot \left\{ \frac{3 \cdot \rho_{Ep} \cdot \left[1 + 0.1 \cdot \left(\rho_P \middle/ \rho_{CA} \right) \right]}{2 + \left(\rho_{Ep} \middle/ \rho_{CuA} \right)} - 1.1 \cdot \rho_P \right\}^{-1} \tag{62}$$

where

x_p: Particle volume fraction inside composite

W: Sample weight

V: Sample volume

ρ_{Ep}: Density of Epoxy Resin

ρ_{CuA}: Density of curing agent

ρ_{CA}: Density of coupling agent

ρ_P: Density of particle's metallic bulk material

3.4.2 X-RAY DIFFRACTION

To analyze the crystal structures and atomic spacing, XRD is a popular method [98]. It is based on the interference of monochromatic X-rays and a crystalline sample. These X-rays are generated by a cathode X-ray tube, filtered to produce monochromatic radiation, collimated to concentrate, and directed towards the sample (Figure 40).

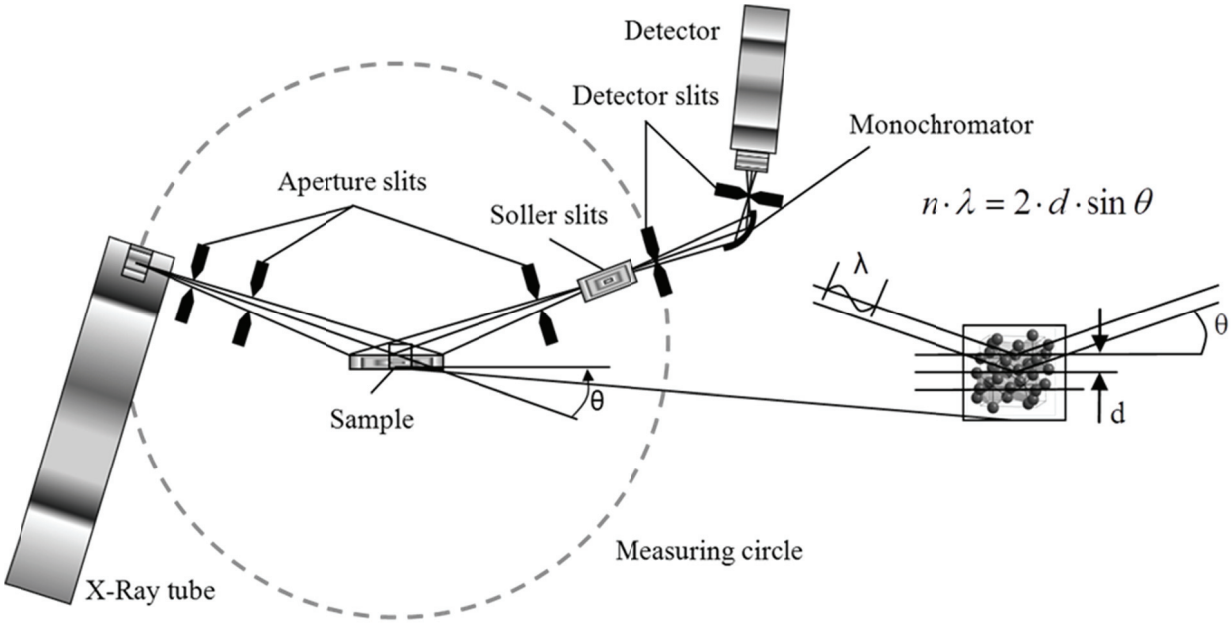

Figure 40 Principle of X-Ray diffraction setup (left), ray interference with lattice (right)

X-rays are placed between ultraviolet light and high energy gamma rays in the electromagnetic spectrum. The wavelength range is between 0.01nm and 10nm (the order of distances between molecules and crystal lattice constants). The analysis is performed in measuring the distances between scattering lattice planes and plane X-ray waves. For an incident ray at an angle of θ with the crystal planes (at distance d apart from each other), the path difference between the incoming and the reflected ray is given by $2 \cdot d \cdot \sin\theta$. The formula to find the maxima of the corresponding interference pattern is known as Bragg's law [99]:

$$n \cdot \lambda = 2 \cdot d \cdot \sin\theta \tag{63}$$

If Bragg's equation (63) is satisfied, a peak will be observed. By comparing the obtained peaks in the XRD pattern to database information about crystalline structures, the existent material can be determined.

Even if in general materials are analyzed in XRD as a powder on a glass slide, for this work, the fabricated nanocomposite samples would be directly applied to the test setup, and the obtained XRD patterns would be compared to the database provided in "Crystal Structures 1" by R.W.G Wyckoff [100].

XRD characterizations are being investigated at Thermodynamics of Materials Research Lab (TMG) at Concordia University.

3.5 Microscope Characterization

The nanocomposite samples are characterized using a scanning electron microscope (SEM) and transmission electron microscope (TEM). SEM is used to investigate the topographic of samples at very high magnifications. The magnifications are more than 3 x 10^6 x. During SEM analysis, a beam of electrons is focused on a spot volume of specimen. The energy of the electron beam varies from a few keV to 50 keV, and two condenser lenses would be focused into a beam with a very small spot size. The beam passes through the objective lens, where pairs of coils deflect the beam either linearly or over a rectangular area of the sample surface. When the primary electron beam strikes the surface of the sample, it is scattered by atoms in sample. During the scattering, the primary beam spreads efficiently and fills a teardrop-shaped volume (interaction

volume, extends about 1-5 μm into the surface). Secondary electrons are released from interactions in this region, then detected, converted to a voltage, and amplified to generate an image.

Transmission electron microscopy is a technique whereby a beam of electrons is transmitted through a very thin sample, and interacts with the sample as it passes through. The interaction of the electrons transmitted through the sample forms an image. This image is magnified and then focused onto a fluorescent screen or detected by a CCD camera. The imaging capability of TEM has a significantly higher resolution than that of light microscope, because of the small wavelength of the electrons.

Chapter 4 Test Results

In this chapter, the effects of the type and size of particles, volume fraction, fabrication process on electromagnetic shielding and absorption are investigated. Also, the most promising particles are selected and introduced into the carbon fiber composites. Calculations using the theoretical models are performed, and the results are compared with experimental data. The results of thermal (DSC, TGA) and mechanical characterizations are presented. The possibilities of using alloy particles as well as particles with a protection layer of carbon are studied, and the results are presented in Appendix C.

4.1 Nanocomposite EM Measurement

In this chapter, the experimental data showing the effect of the type of nanoparticles (iron, nickel, cobalt, and iron oxide) and the particle sizes (iron and nickel) on EMS are presented. Also, the impact of increasing the particle loading of iron and Fe_3O_4 nanoparticles is provided.

Here, the graphs represent the measured power density for absorption (A) and total shielding (*total*) in relation to the incident power density. Later, more detailed graphs representing dB units are given. The values of total shielding are obtained by the transmitted power (T); absorption is obtained by transmitted and reflected (R) power in relation to the incident power:

$$total = \frac{P_{totalShield}}{P_{incident}} = 1 - \frac{P_{trasnmitted}}{P_{incident}} = 1 - T \tag{64}$$

$$A = \frac{P_{absorbed}}{P_{incident}} = 1 - \frac{P_{reflected}}{P_{incident}} - \frac{P_{transmitted}}{P_{incident}} = 1 - R - T \tag{65}$$

The effect of reflection can be seen as the difference between absorption and total shielding. The X-band (8.2GHz to 12.4GHz) is considered as the frequency band in this work.

The effects of the different materials on EMS are given in Figure 41. Fe_3O_4 nanoparticles (dotted lines) have the lowest absorption capability in measured range of frequencies. Around 5% of field power is absorbed up to about 11.25GHz. However it shows a major growth, up to 23% at the end of frequency range. In general, it is behind the other materials in terms of absorption. Simultaneously, the samples with Fe_3O_4 particles get a very low reflection of electromagnetic waves (~5%). Most likely, this is due to the low conductivity of the iron oxide (6 times less than that of iron).

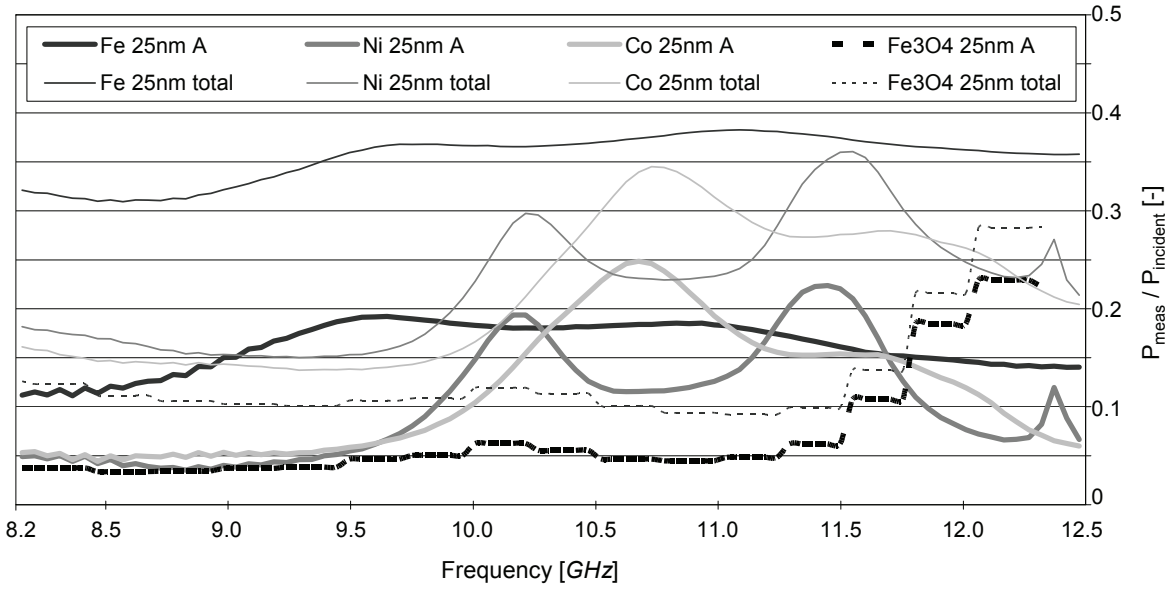

Figure 41 Effect of type of material on absorption and total shielding

The samples with nickel and cobalt embedded particles show a low absorption up to around 9.5GHz. Similarly, increases of 25% at 10.7GHz for cobalt and 22% at 11.4GHz for nickel is observed at higher frequencies. Unsteady behavior for both materials is monitored. The absorption of the nickel samples decreases from (19% at 10.2GHz) and (at 11.4GHz) to 12% and 7%. The absorption of the cobalt sample reduces (after the single peak) to 15% at 11.5GHz and to 6% at 12.4GHz. Total shielding of both samples generally follows the curves for absorption, but at a higher level of about an additional 8% to 15%, which represents the reflection part of total shielding. Most likely, natural resonances of the nanoparticles are the reason for the variation over the frequency for both materials.

Compared to the others, the iron particles show a more steady absorption curve. Set off at a higher level (12%), the absorption increases up to 19% at 9.5GHz. It remains on this value until 11.0GHz, following by a reduction to 14% at 12.4GHz. Even if the absorption does not attain the peaks of cobalt and nickel, it remains more constant and, as a result, at a higher level. Also, the total shielding is higher than others, varying from 33% up to 38%. The reflection varies from 17% (at 9.2GHz) to 22% (at 12.3GHz).

The effect of particle size for iron particles on absorption and total shielding are shown in Figure 42. All of three different sizes reach a level of absorption of about 20%; only the frequency at which this value is obtained primarily varies. The smallest iron particles of 25nm generate absorption of 19% at 9.6GHz, for particles of 50nm size at 10.8GHz and for the biggest particles (75nm) at 11.4GHz. All three iron particles present smooth behavior of absorption without particulate peaks compared to the others.

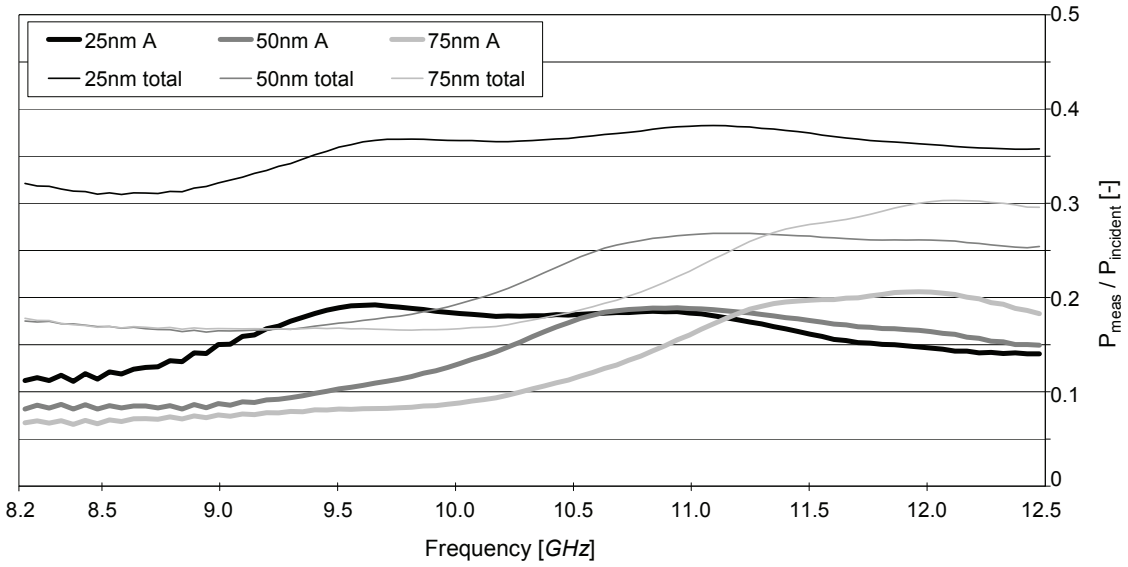

Figure 42 Effect of size on absorption and total shielding of Iron nanoparticle

Even if the small iron nanoparticles (25nm) expose the best general absorption capability, they demonstrate the highest reflection of 17% up to 22%, which is comparatively higher than the absorption. This effect is not essentially required, as the high reflection can be provided by the carbon mesh inside PMCs. For iron particles of 50nm and 75nm, reflection is restricted to 7% (at 10.3GHz) and 10% (at 12.4GHz).

The comparisons of different sizes for nickel particles expose an unsteady performance in terms of absorption and shielding, particularly compared to iron particles. Figure 43 gives the absorption and shielding for nickel particle with sizes of smaller, equal or greater than 15nm.

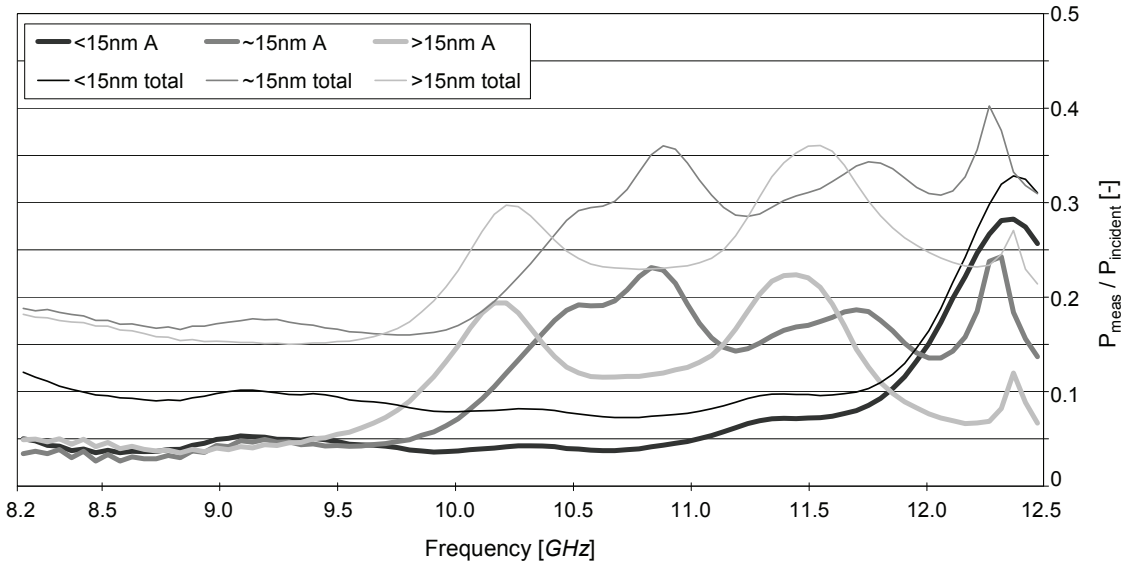

Figure 43 Effect of size on absorption and total shielding for Nickel nanoparticle

Then they generate the highest absorption of around 28% at 12.3GHz, the particles smaller than 15nm experience a shortage of absorbance between 8.2GHz to 11.7GHz. The curve tendency is like the absorption of Fe_3O_4 particles with the size of 25nm (Figure 41), but total shielding is lower. The reflection decreases from 8% (at 8.2GHz) to 1.5% at 12GHz.

For nickel particles of 15nm or larger, the absorption curves experience several peaks at different frequencies, but no consistent trend is observed. For particles of ~15nm, peaks are observed at 10.8GHz (23%), 11.7GHz (18%) and 12.3GHz (24%). Also, three peaks occur for particles larger than 15nm, given at 10.2GHz (19%), 11.4GHz (22%) and 12.4GHz (12%). Reflections differ between 8% (at 10.3GHz) and 17% (at 11.8GHz) for both kinds of samples, and consequently are lower than the absorption portion. Total shielding exposes peaks at the same frequencies as the absorption curves with the highest values of 40% at 12.3GHz for particles around 15nm in size and 36% at 11.4GHz for particles larger than 15nm.

Even if all nickel particles high values of absorption and total shielding are attained, general curve tendencies are not completely fulfilling, as considerable reductions are observed between the different peaks. Apparently, particles are not able to provide a constant absorption and total shielding over the range of frequencies in this work.

To complete the picture of the shielding mechanism, the impacts of particle loading in the composites are demonstrated for iron and Fe_3O_4 particles. In Figure 44 the change of absorption and total shielding for increasing of particle volume fraction from 4% to 20% for iron particles in a size of 50nm can be observed. Increasing the fraction of particles to above the percolation threshold exposes an improvement of absorption of around 15%, which is around two times the values for 4% volume fraction. As the reflection part of the shielding is higher for augmented volume fraction—17% to 21% comparing to 6.2% to 9.5%—the total shielding of these samples terminates from 44% (at 8.8GHz) up to over 50% (at 11.5GHz to 12.4GHz).

However, even if the total shielding, as with the absorption, can be increased considerably, the enhancement of shielding by around 100% is related to particle loading five times higher than before. This relates to an increase of around 80% of the sample weight, and wipes out the weight-saving benefit of a composite material (Appendix B).

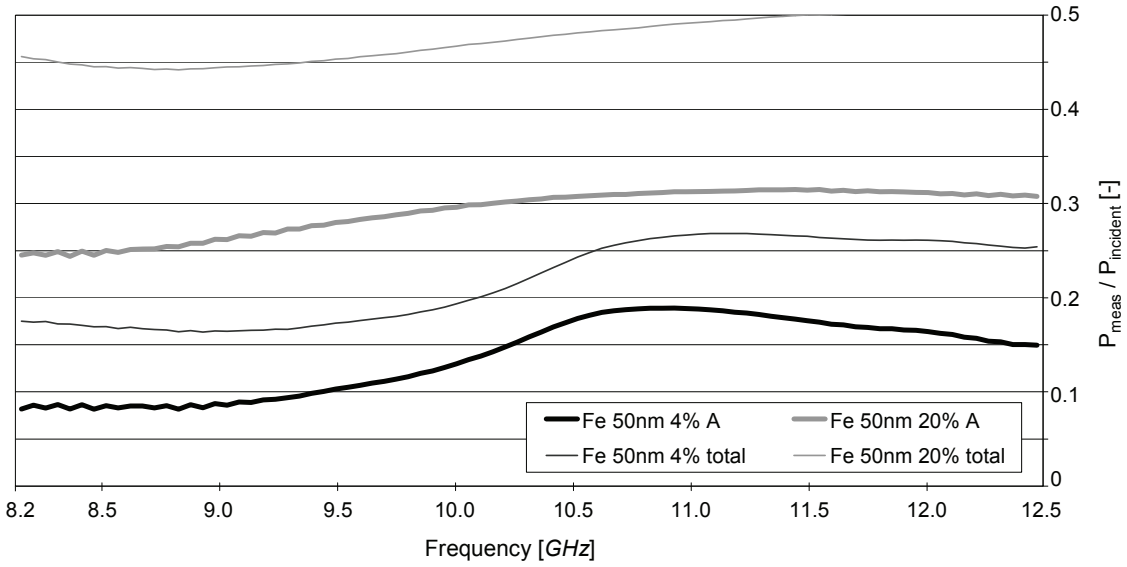

Figure 44 Effect of particle loading on absorption and total shielding for Iron nanoparticle

In Figure 44, the effect of particle volume fraction of Fe_3O_4 is shown. The highest value of absorption is only a little improved from 23% at 12.1GHz to 26% at 11.6GHz with an increase of the volume fraction from 4% to 20%. The main difference is attained by a four times higher absorption for the frequencies lower than 11.5GHz (around 20% as opposed to 5%). The reflection part of shielding is improved by just 6-7%, which is around two times more.

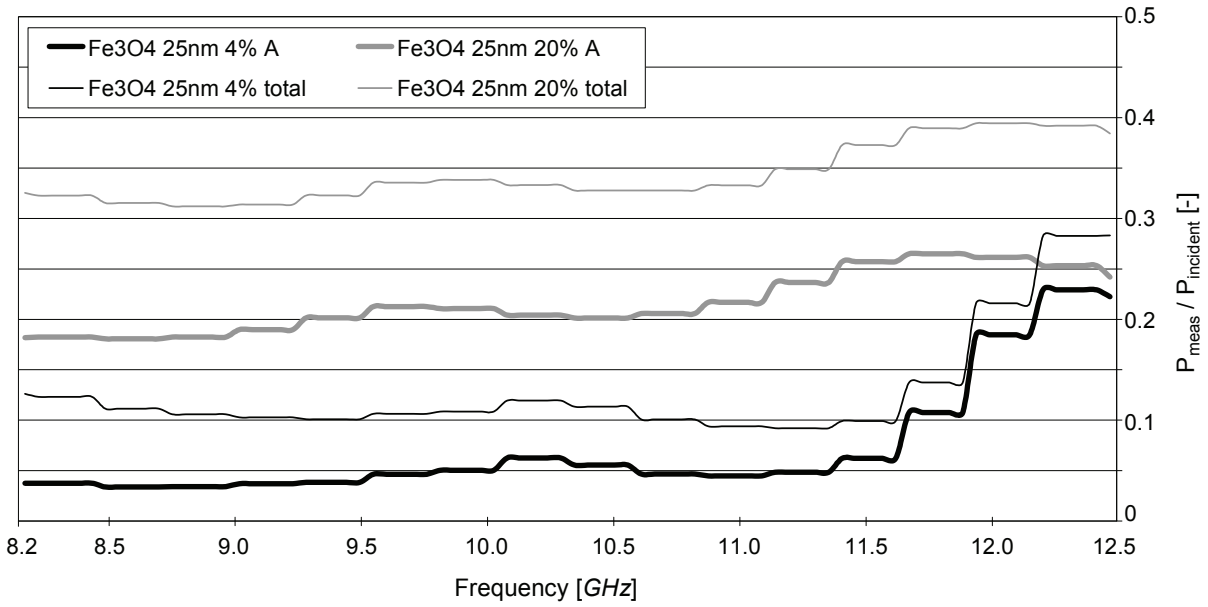

Figure 45 Effect of loading on absorption and total shielding for Fe_3O_4 nanoparticle

Even though increasing of the volume fraction of Fe_3O_4 particles in the composite directly relates to a considerable improvement in absorption and at the same time raises the reflection, the same level of absorption and shielding can be obtained with only 4% volume fraction of iron particles (see Figure 45). The increasing of Fe_3O_4 particles to 20% brings up 40% addition of weight comparing to 4% iron loading.

Comparing all above materials for application in aerospace structures, apparently iron particles have the most stable and predictable shielding and absorption behavior. Cobalt and nickel particles get lower absorption, but with several peaks that are principally followed by sharp declines. Iron oxide cannot offer the same level of shielding as others and an increase of filler volume fraction to reveal adequate absorption would cause too much weight of the composite.

Changing the particle size of nickel does not affect significantly the shielding. But for iron, changing the particle size influences the frequency at which the high level of absorption is attained and on the reflection part of the shielding. The smallest particles of

25nm get the highest reflection, which is not needed in terms of eliminating of re-reflection of electromagnetic fields inside the cabin. The particles of 50nm demonstrate the lowest reflection, but at the same time provide a higher absorption than particles of 75nm. Also, it should be considered that the high reactivity of the smallest particles of 25nm needs extra efforts in manipulation to prevent any oxidization and agglomeration. As a result, iron particles of 50nm offer an acceptable level of absorption and shielding, have a high capacity for application to manufacturing procedures, and are the most promising particles for following the research in this work. In Figure 46, the total shielding and absorption level of both revised fabrication processes (1 and 2 explained in chapter 2) are presented. Modifications of fabrication process do not have a significant effect on absorption portion of shielding.

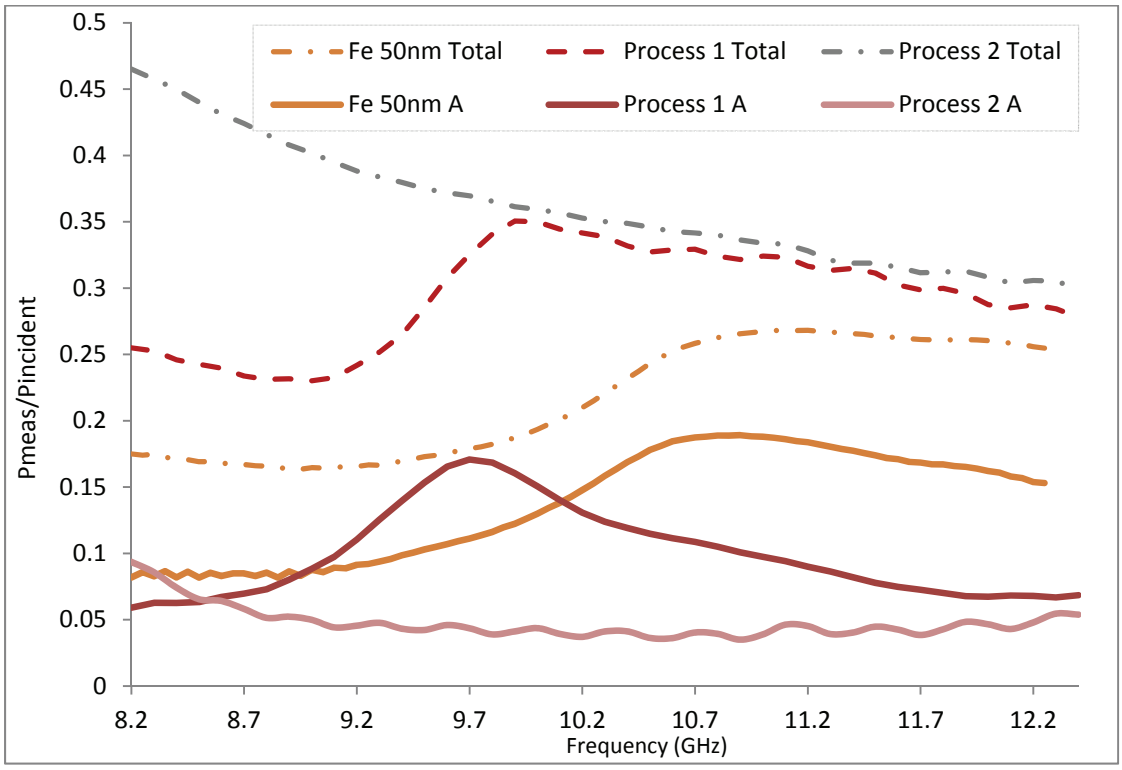

Figure 46 EM comparison of conventional and modified methods of fabrication

4.2 Nanocomposite Thermal Analysis

The addition of filler in polymer influences the performance of matrix. This is known and popular in industry. However, there are many factors, such as the size and shape of particles, composition, and interactions at the NPs/matrix interfaces that can affect the effectiveness. Still, some trends can be observed. The nanoparticles generally increase the glass transition temperature for amorphous polymers and promote good interaction between filler/matrix, which is the case when using an epoxy and a coupling agent. Thermal stability and decomposition temperature tend, however, to be decreased by addition of metallic filler [101].

4.2.1 DIFFERENTIAL SCANNING CALORIMETRY

It appears on DSC curves (see Figure 47) that the addition of the nanofillers at 4vol% does not significantly change the glass transition temperature (Tg) of the studied materials. The most important exposed curve is the one for cobalt filler, which has a Tg of 2.5°C lower than pure epoxy. It is essential to mention that the mixture of epoxy and NPs needs to be as efficient as pure resin. It's particularly important that adding the mentioned percentage of these types of particles does not change extremely the thermal behavior of polymer. As potentially these particles will be used in the polymer phase of composite and ideally they should not change the thermal behavior of composite.

The variation in specific heat capacity (C) due to filler loading compared to the reference sample of pure epoxy has to be estimated. This estimation is given in Table 2.

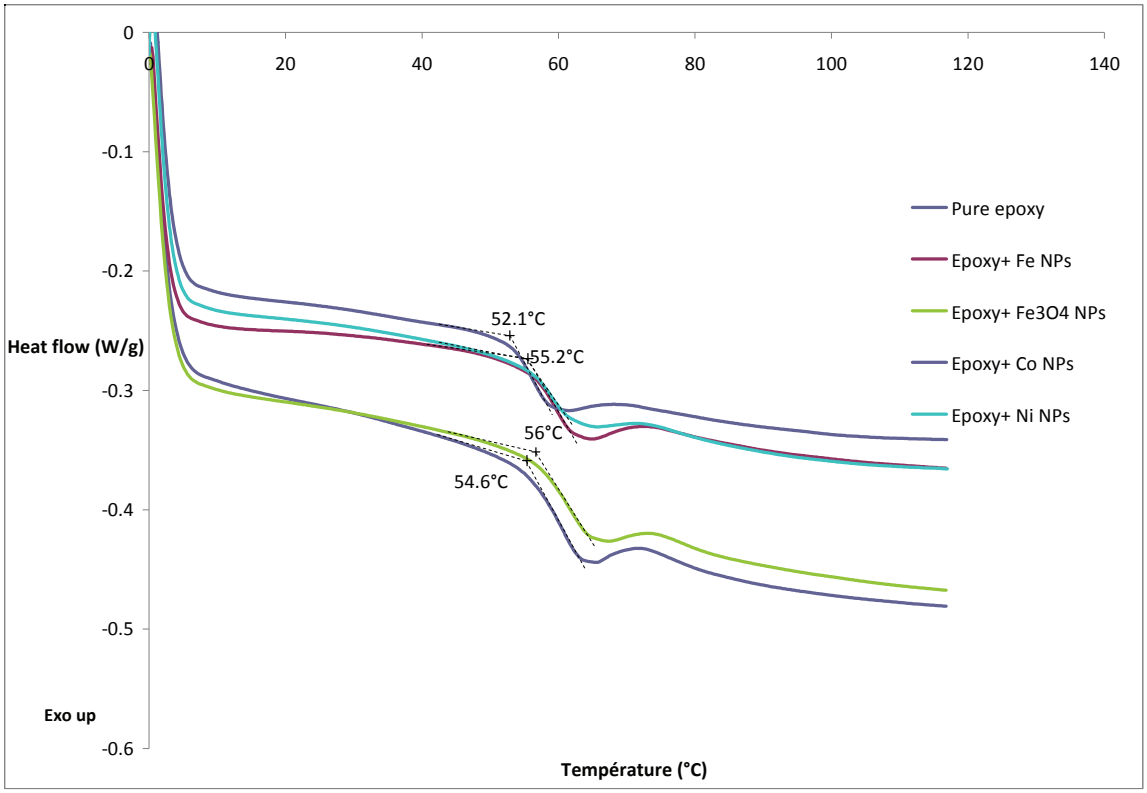

Figure 47 DSC curves of nanocomposites and pure epoxy

Table 6 Thermal analysis using DSC

	Pure epoxy	Epoxy + Fe NPs	Epoxy + Fe_3O_4 NPs	Epoxy + Co NPs	Epoxy + Ni NPs
Tg onset (°C)	54.6	55.2	56	52.1	55.2
Specific heat capacity (J/kg/K) à 40°C	2005	1567	1982	1457	1543
C_{sample}/C_{ref} (%)	100	78	99	73	77

It can be seen that the curves of pure epoxy and epoxy with Fe_3O_4 NPs are relatively close. However, the curves of the samples with Fe, Co and Ni NPs are below 20%, and they increase more slowly than pure epoxy. The specific heat capacity loss can potentially be a safety hazard, as in similar conditions, the material would take less time to reach critical temperatures (e.g. combustion and decomposition points). In persistence of this work, the flammability tests have to be performed as well.

4.2.2 THERMAL GRAVIMETRIC ANALYSIS (TGA)

TGA curves (Figure 48) show the decomposition temperatures (Td). Difference in the comparison to the pure epoxy sample is negligible. The most significant change belongs to cobalt, with reduction of 16°C compared to pure epoxy. The difference between the weight of a sample with fillers and pure epoxy is relatively close to the weight fraction of added NPs to samples (just for Fe, Ni and Co fillers). The difference for Fe_3O_4 is not explainable. Decomposition of polymer is a complex phenomenon that includes many reactions that are difficult to analyze. The TGA curve for the composite with cobalt has three inflection points, suggesting three different decomposition mechanisms.

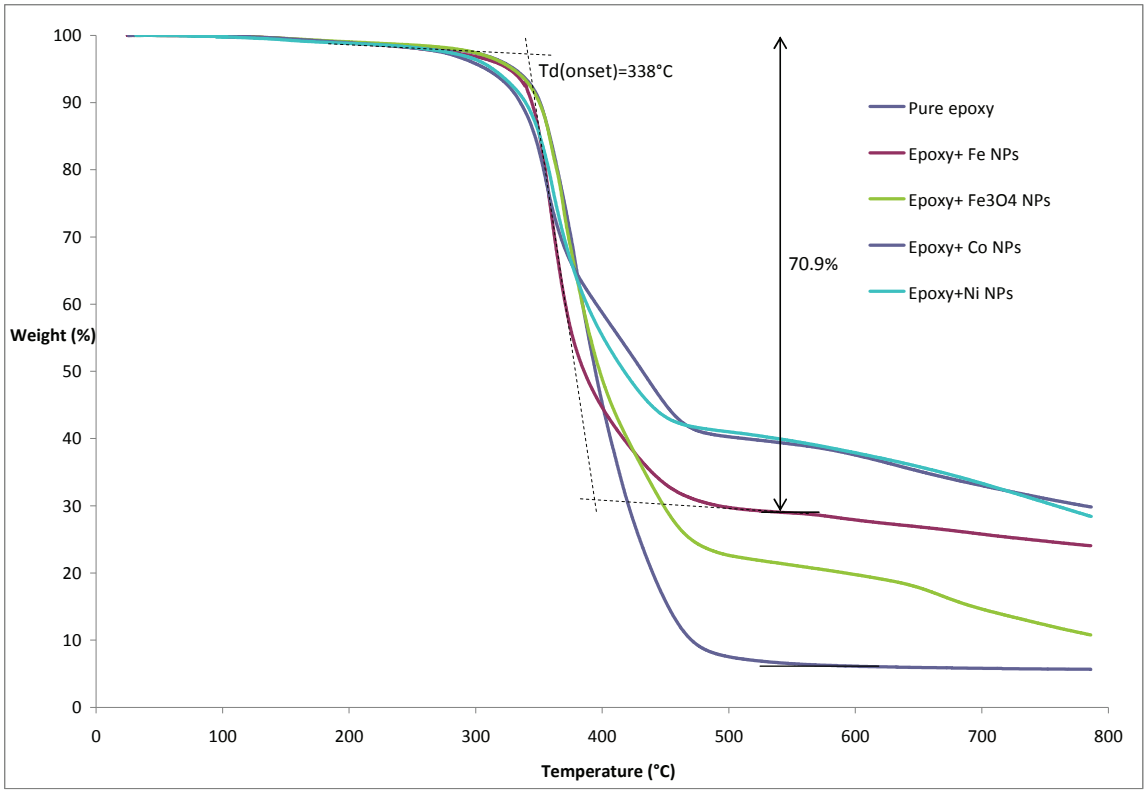

Figure 48 TGA curves of nanocomposites and pure epoxy

Table 7 Degradation behavior of nanocomposites and pure epoxy

	Td onset (°C)	*Weight loss (%)*	*Δweight at 780°C (%)*	*NPs weight (%)*	*IPDT (°C)*
Fe	338	69.7	19.8	23.5	887
Fe3O4	342	77.0	6.5	16.8	695
Pure epoxy	345	92.6	0	0	469
Cobalt	329	58.4	25.8	25.2	1224
Nickel	332	57.7	23.8	25.2	1165

The Integral Procedure Decomposition Temperature (IPDT) proposed by Doyle [102] is used here for estimating the thermal stability of polymeric materials. The IPDT can be calculated from the whole curve by using the following equation:

$$IPDT(^{o}C) = A^{*}K^{*}(T_f - T_i) + T_i \tag{66}$$

where A^* is the area ratio of total experiments divided by total TGA thermogram, K^* is the coefficient of A, T_f is the final temperature and T_i the initial temperature of the TGA experiment. The results of these calculations can be seen in Figure 52.

$$A^{*} = \frac{S_1 + S_2}{S_1 + S_2 + S_2} \text{ and } K^{*} = \frac{S_1 + S_2}{S_1} \tag{67}$$

Schematic representation of S1, S2 and S3 for A* and K* are given by C.L. Chiang et al. [103].

The IPDT increases significantly with the addition of metallic fillers. The value for pure epoxy is 469°C which is consistent with literature. The IPDT for Fe_3O_4, Fe, Ni and Co increases by 48%, 89%, 148%, and 161% respectively. All sample epoxies have the same NPs volume fraction (4%), but due to density differences, the weight percentage is different for each sample. There are 16.8, 23.5 and 25.2 wt% for Fe_3O_4, iron, nickel and cobalt fillers respectively. It seems that there is a correlation between weight of added NPs and thermal stability (IPDT), because metallic particles do not decompose at this temperature (Figure 49).

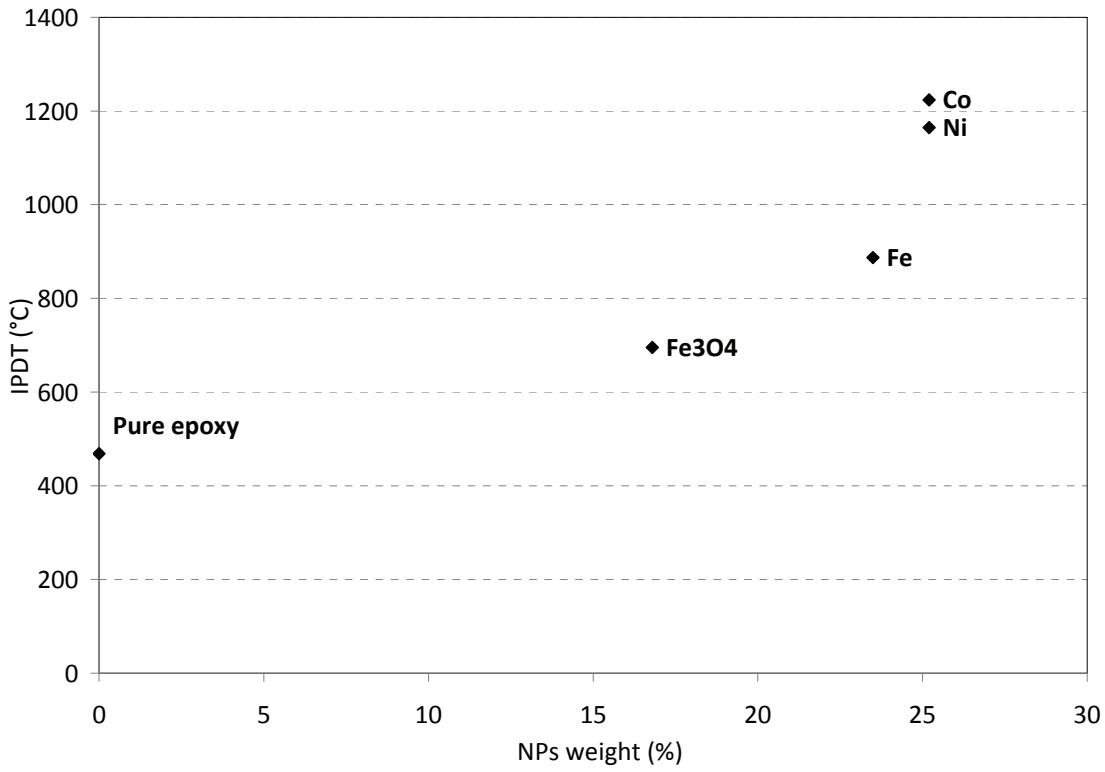

Figure 49 Correlation between charge weight and IPDT

The difference between weight post-decomposition and weight fraction causes a high IPDT value for nickel and cobalt filler, and so a higher thermal stability.

4.3 Nanocomposite Mechanical Testing

The four points bending test is performed to characterize the EM shields from a mechanical point of view. This test is proposed to study the flexural properties of unreinforced and reinforced plastics and electrical insulating materials. In Figure 50, a picture of the setup for 4 points bending is shown. To perform this test, only a universal testing machine and four point flexural test fixture is needed. Bending tests involve the measurement of ductility of a sample. Or, it may involve bending a material until the

material experiences fracture, and determining both the load and deflection required to initiative the break limit. The result of test is presented in Figure 51.

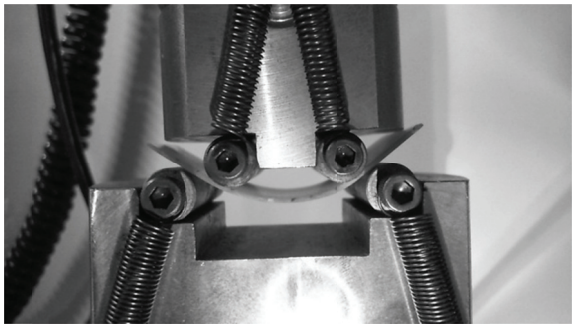

Figure 50 4 points bending setup

In following graph of extension (mm) versus stress (MPa), the curves follow almost the same curvature as Epoxy. Only the sample with iron oxide broke. In the case of iron, which is the selected particle in this work, no breakage occurred.

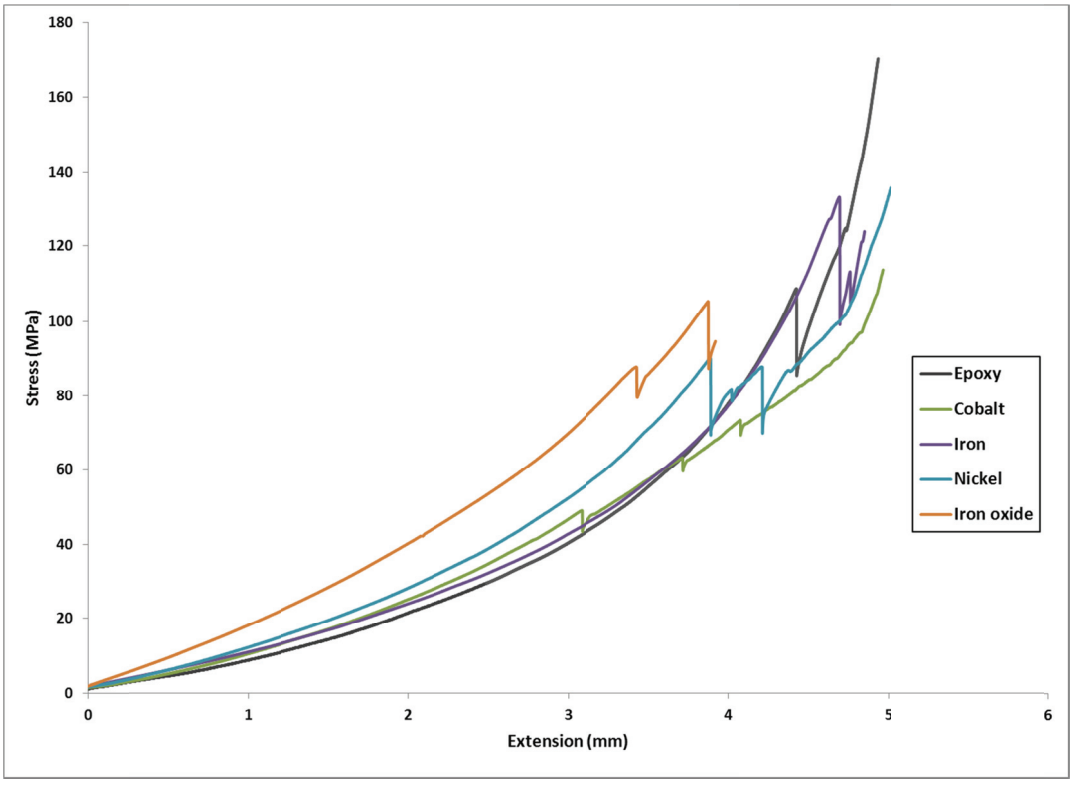

Figure 51 Mechanical testing result for 4 points bending test

4.4 Verification of Fabrication Procedures

It is required to verify the composition of the fabricated samples with the aim of providing reliable facts for electromagnetic shielding effectiveness of the fabricated nanocomposites. Here, three different techniques of analysis are presented to provide sufficient information about the present nanocomposites. To be certain about the volume fraction of metallic nanoparticles inside the composite, the weight and volume of each sample is estimated. With the help of both and with the knowledge of all the other component's material properties it is possible to calculate the volume fraction of the particle filler. X-ray diffraction analysis can be helpful for determining the type of the applied nanopowders' metallic elements. Also it could be used to get (through the Scherrer formula) a general idea of the particle sizes embedded into the epoxy resin.

4.4.1 VERIFICATION OF THE VOLUME FRACTION

Following the fabrication procedure, with the exception of dispersing agent (e.g. chloroform), the rest of the materials, including the epoxy resin, curing agent, coupling agent, and metallic nanoparticles, are found in each sample of nanocomposite.

Equation (62) presumes a homogeneous composite without any embedded air bubble (which should be avoidedby the application of the vacuum mixer). The various material properties are listed in Table 8 and Table 9:

Table 8 Densities of matrix components

	Epoxy resin (EPON RESIN 828RS)	Curing agent EPIKURE 3046	Coupling agent 3-APTES
Density [g/cm³]	1.16	0.95	0.93

Table 9 Densities of metallic bulk materials

	Iron Fe	Iron Oxide Fe_3O_4	Nickel Ni	Cobalt Co
Density [g/cm³]	7.87	5.18	8.91	8.89

The nanoparticle's volume fraction can be calculated by the three samples of each type that are analyzed. The weight is measured with a scale with the precision of *0.1mg*, the volume is determined manually with a digital caliper with the precision of *0.01mm*. The received average values are given in Table 10 and Table 11.

Table 10 Volume fraction of particles inside nanocomposites (1)

	Fe				Fe_3O_4	
Particle size [nm]	20	40-60	40-60	60-80	20-30	20-30
Av. volume fraction [%]	4.12	4.18	18.96	3.91	4.40	19.88

Table 11 Volume fraction of particles inside nanocomposites (2)

	Ni				Co	Epoxy
Particle size [nm]	<15	~15	>15	20	25-30	-
Av. volume fraction [%]	4.08	4.00	4.05	3.92	3.96	-0.51

The average particle volume fraction inside the nanocomposites is in general about 4%. However, the analysis of the pure epoxy samples leads to the statement that the accuracy of measurement is limited and the acquired results can only represent a coarse estimation of particle loading. However, volume fraction values happen in an expected variation, both for low (~4%) and high (~20%) particle loadings.

4.4.2 VERIFICATION OF MATERIAL THROUGH XRD PATTERN

Five different samples are analyzed:

- Composite with iron (Fe) particle (40-60nm) filler at 4% vol. fraction
- Composite with iron oxide (Fe_3O_4) particle (20-30nm) filler at 4% vol. fraction
- Composite with cobalt (Co) particle (25-30nm) filler at 4% volume fraction
- Composite with nickel (Ni) particle (<15nm) filler at 4% volume fraction
- Sample of pure epoxy resin

The XRD pattern of a nanocomposite sample with iron particle is shown in Figure 52. The labeled peak marks are extracted from the American Mineralogist Crystal Structure Database [104, 105].

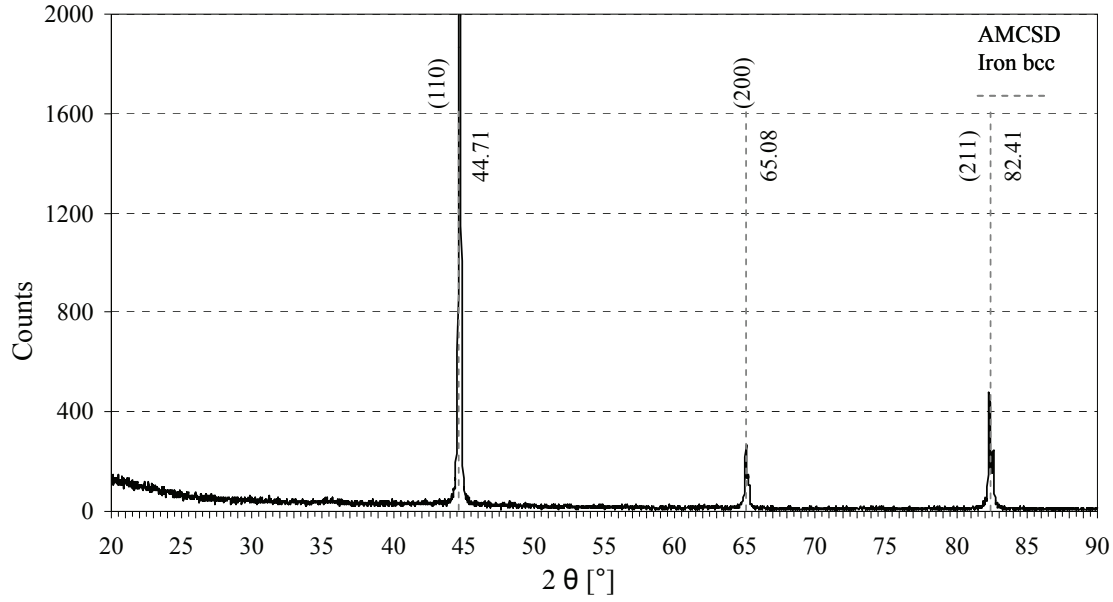

Figure 52 XRD pattern of nanocomposite sample with iron (Fe) particles

For the analyzed sample, the pattern peaks fit very well with the characteristic of a body centered cubic crystalline structure of the iron lattice. Thus, it can be ensured that the material of nanoparticle is actually iron (Fe) as expected. The XRD pattern for samples with Iron oxide (Fe_3O_4) and cobalt (Co) nanoparticles are provided in Figures 53 and 54. Both analyses confirm the expected metallic materials. The cobalt metal occurs in a cubic closest packed crystalline structure and likewise does not show any oxide appearance.

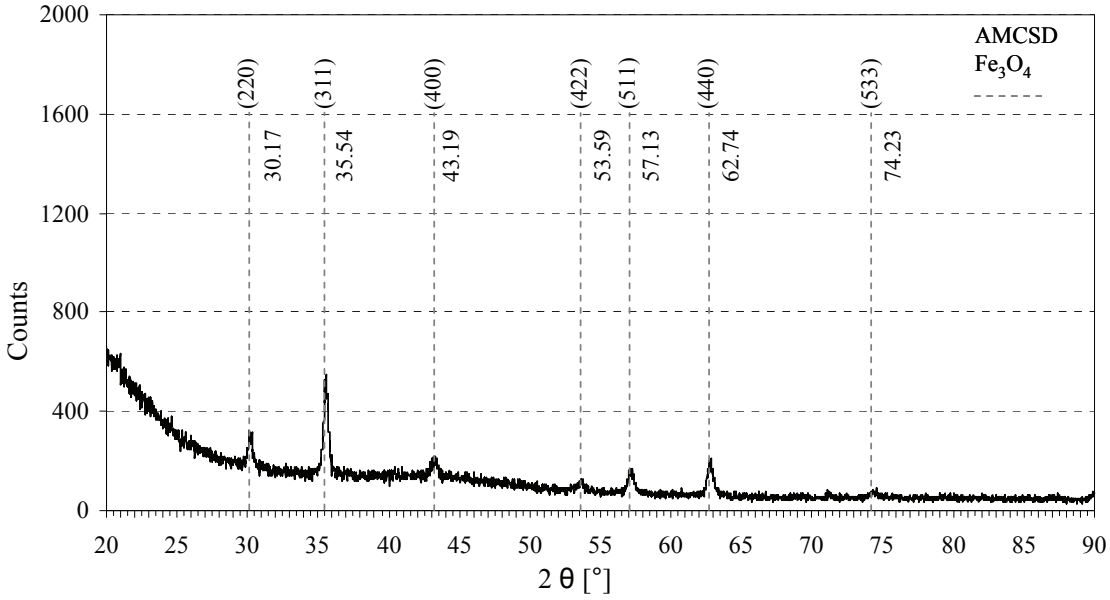

Figure 53 XRD pattern of nanocomposite sample with iron oxide (Fe3O4) particles

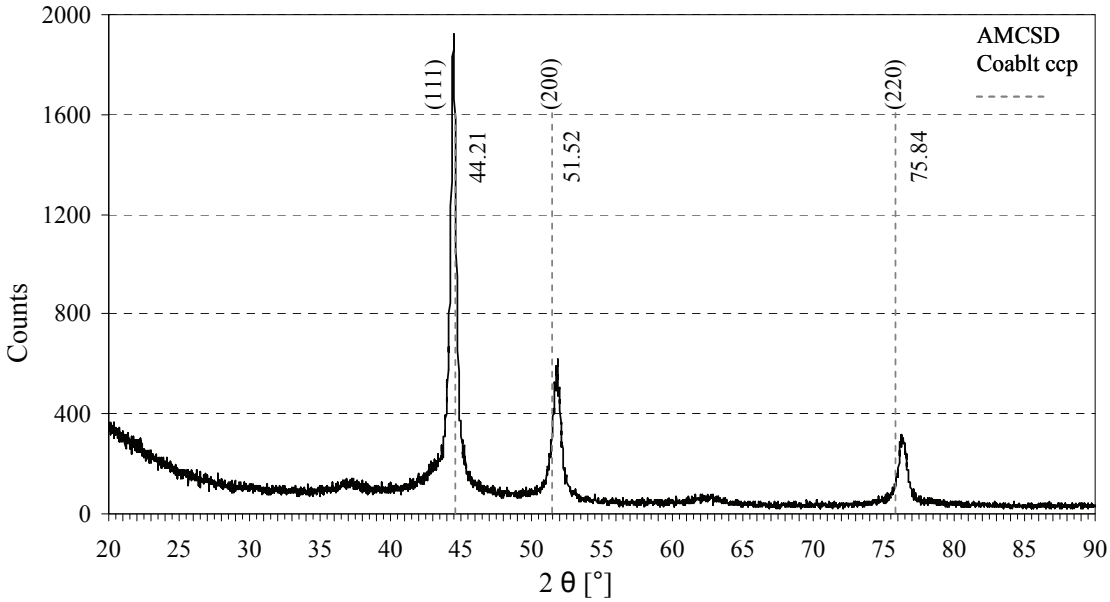

Figure 54 XRD pattern of nanocomposite sample with cobalt (Co) particles

The proof of nickel (Ni) metallic material in the accordant nanocomposite sample, as well in a closest cubic packed structure, is shown in Figure 55. By means of this pattern the influence of the epoxy resin matrix material can be shown similarly. The

hump at small values for θ is related to the amorphous structure of the polymer. Although it is not formed in the same manner for all considered samples due to feasible occurrence at lower θ angles than traced, the XRD pattern of pure epoxy resin in Figure 56 shows the general influence by the matrix component.

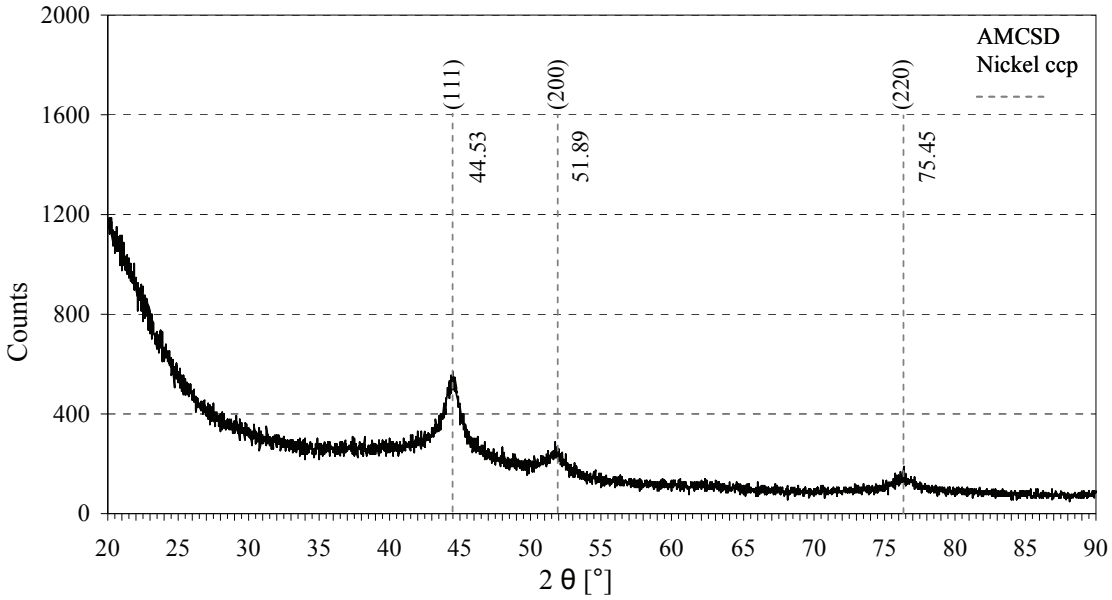

Figure 55 XRD pattern of nanocomposite sample with nickel (Ni) particles

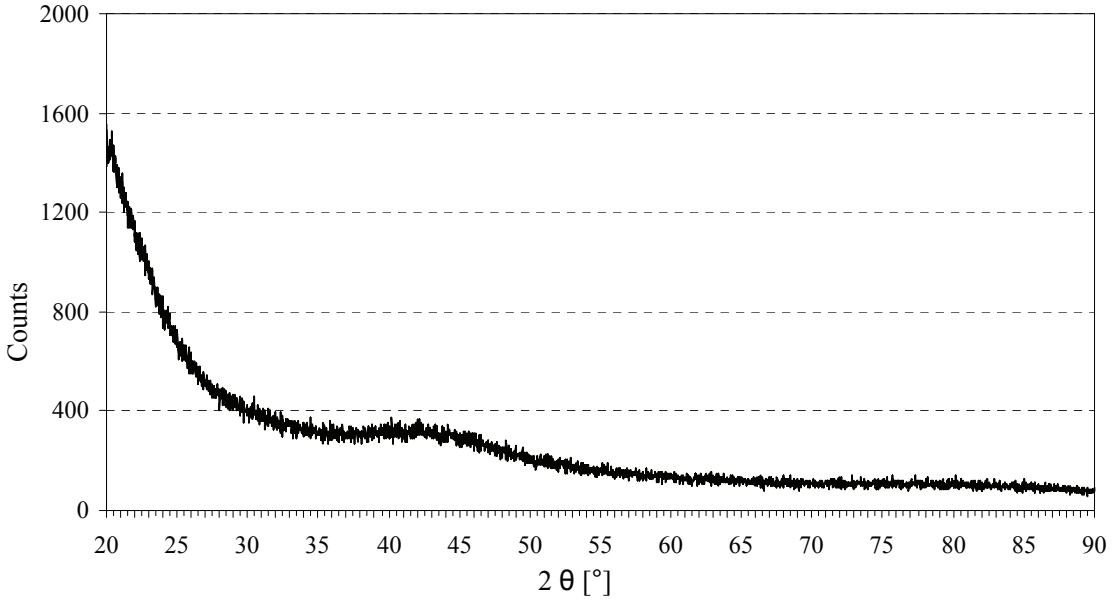

Figure 56 XRD pattern of pure epoxy resin sample without particles

4.4.3 VERIFICATION OF PARTICLE SIZES THROUGH SCHERRER FORMULA

Size determination of the particles embedded in the nanocomposites is mandatory to complete the verification of the fabricated samples. Based on the diffraction peak's width of XRD patterns, the dimensions of nanoparticles are calculated using the Scherrer equation. Strictly, the Scherrer method calculates the size of crystallites instead of the size of particle [106]. Large particles can include several crystallites. However, it is typical that nanometer-sized particles contains only one crystallite. Consequently, the size of crystallites in nanometer-sized particles as calculated by the Scherrer relation also indirectly reveal the size of particle itself. Small crystallites have a restricted number of reflection planes, and the diffraction peaks are a result of constructive interference of X-rays reflected by these, therefore the width of diffraction peaks relate to the crystallite/particle size.

$$d = \frac{K \cdot \lambda}{(2\theta_2 - 2\theta_1) \cdot \cos(\theta_{\mathrm{Im}\,ax})} \tag{68}$$

Equation (68) gives the Scherrer formula for the particle diameter d, the derivation based on Bragg's law and wave interference. K is a dimensionless constant that might range from *0.89* to *1.39* depending on the geometry of the scattering objects. For a perfect two-dimensional lattice, numerical calculations yield the lower constraint of *0.89* for K [107]. A cubic three-dimensional crystal is best described by $K=0.94$, while analytical calculations for a perfectly spherical object yield $K=1.33$ [108]. Assuming spherical particles inside the nanocomposites, K is set to *1.33*.

λ is the wavelength of the incident X-ray, in this case *0.15405nm* according to the test setup applied. The determination of the three different diffraction angles θ_1, θ_2, and

θ_{Imax} of equation (68) is demonstrated in Figure 57. Thus, using the example of the XRD pattern of the cobalt nanocomposite and considering the first diffraction peak in particular, $2\theta_1$ and $2\theta_2$ give the diffraction peak width at the half maximum of intensity, also called the full width at half maximum (FWHM). Through the entity of amorphous matrix structure, the maximum intensity (I_{max}) cannot be considered directly but must be related to the background diffraction intensity of the polymer (I_{min}). However, the peak's highest value leads to θ_{Imax}.

Equation (68) provides the identification of particle size through the determination of these three specific diffraction angles. The calculation is performed for the four different nanocomposite samples, including the metallic particle filler listed above.

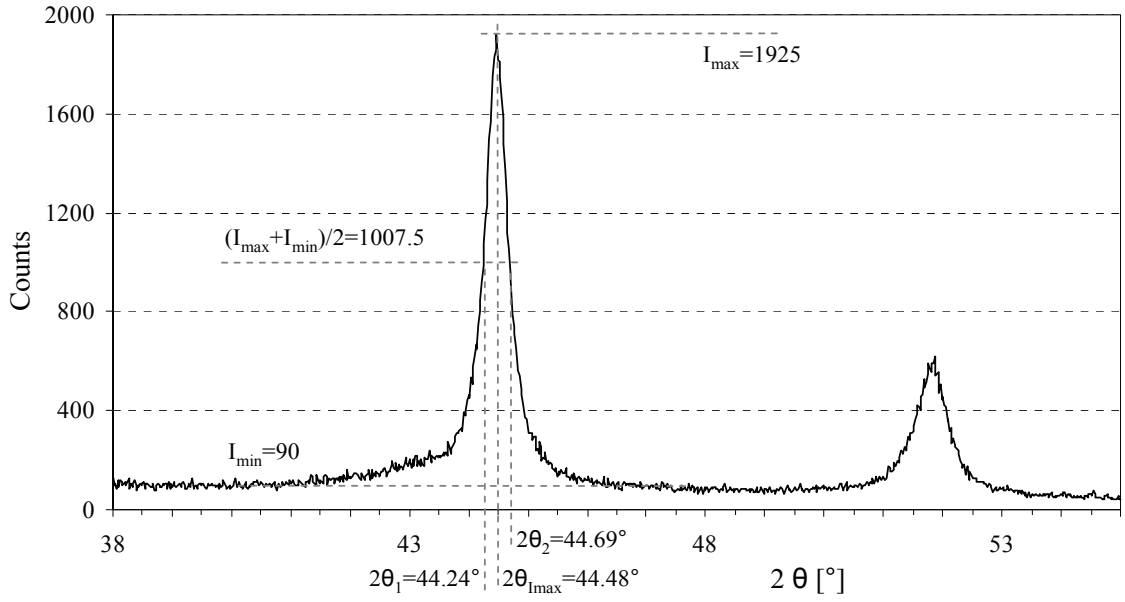

Figure 57 First peak shape of cobalt (Co) sample and related parameters for particle size calculation through Scherrer formula

Table 12 provides the determined values for the particle size of particle loadings. Aside from a small variation for the iron particles that is comparatively low, all the particle sizes fit to the information given by the particle supplier. The imprecision of the iron

particle's size calculation can also be explained by the limitations of Scherrer formula with nano scale particles. The calculation is meant to provide adequate results up to a size of *0.1-0.2μm* [109], the size of *60nm* may induce the first appearance of deviation.

Table 12 Calculation of particle sizes through Scherrer formula

	Iron Fe	Iron Oxide Fe_3O_4	Nickel Ni	Cobalt Co
$2\theta_1$ [°]	44.64	35.34	43.81	44.24
$2\theta_2$ [°]	44.85	35.77	45.88	44.69
$2\theta_{Imax}$ [°]	44.72	35.52	44.46	44.48
Expect. particle size [nm]	40-60	20-30	<15	25-30
Particle size [nm]	60.45	28.67	6.13	28.18

4.5 Nanocomposite Microscope Analysis

4.5.1 ELECTRON MICROSCOPE

To be sure that fabricated samples do not contain defects (e.g. air inclusions caused by stirring and/or lack of homogeneity), before performing the thermal analysis, the samples are examined under the SEM and the conventional optical microscopy.

Because of very low conductivity of the samples (cause concentration of electrical charges) observation with Electron Microscopy is not straight forward (Figure 58).

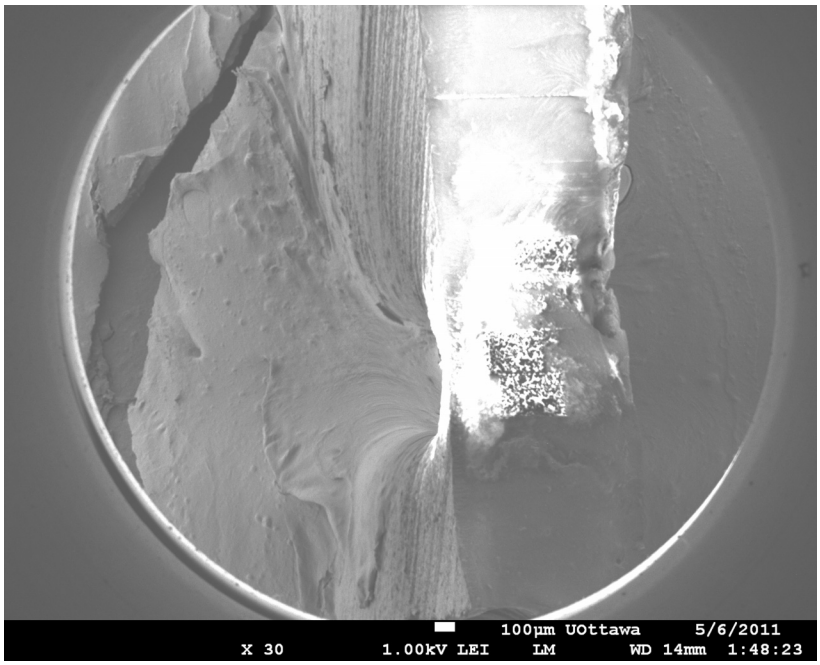

Figure 58 SEM photograph of sample with Fe NPs (x30)

Despite this problem, the areas with particles are shown visibly. However, the accumulation of electric charge on the surface prevented the use of EDS to measure the composition of the particles. The observed size of around 50nm is consistent with the iron particles (40-60nm).

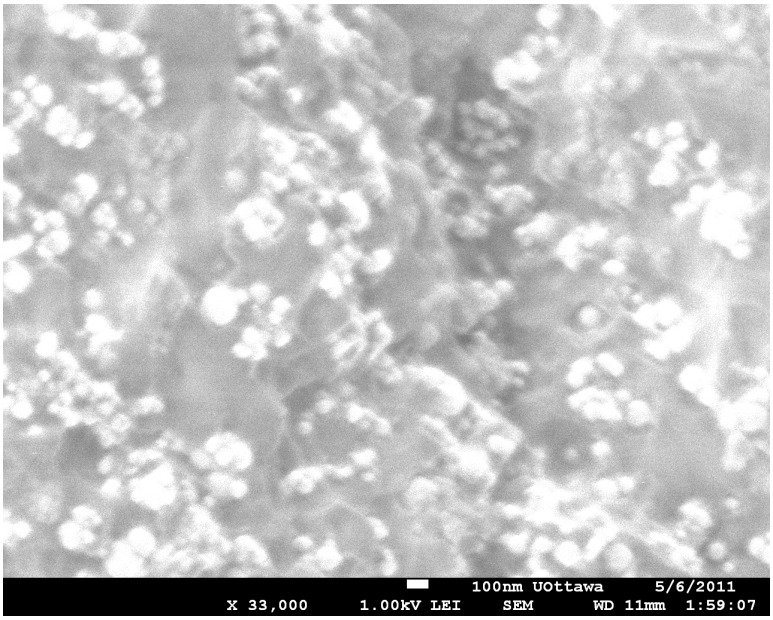

Figure 59 Nanometric dispersion of Iron NPs

SEM gives an acceptable local view on samples (Figure 59). However having an overall view of the sample would be useful as well. To do so, the following method of optical microscopy (as a physical method of analysis) is performed. This method can be used easily by industry because of simplicity and low cost.

4.5.2 OPTICAL MICROSCOPY (AS A PHYSICAL METHOD OF ANALYSIS)

Optical observations on the iron NP sample revealed some bright clusters with a size between 30µm to 0.5µm (limit of resolution in Figure 60). Clearly this kind of filler changes the polymer properties because of high magnetic properties due to diameter of spherical particles [110, 111]. Using the image processing software of "Image" gives the possibility of estimating the area fraction of clusters (see Figure 61).

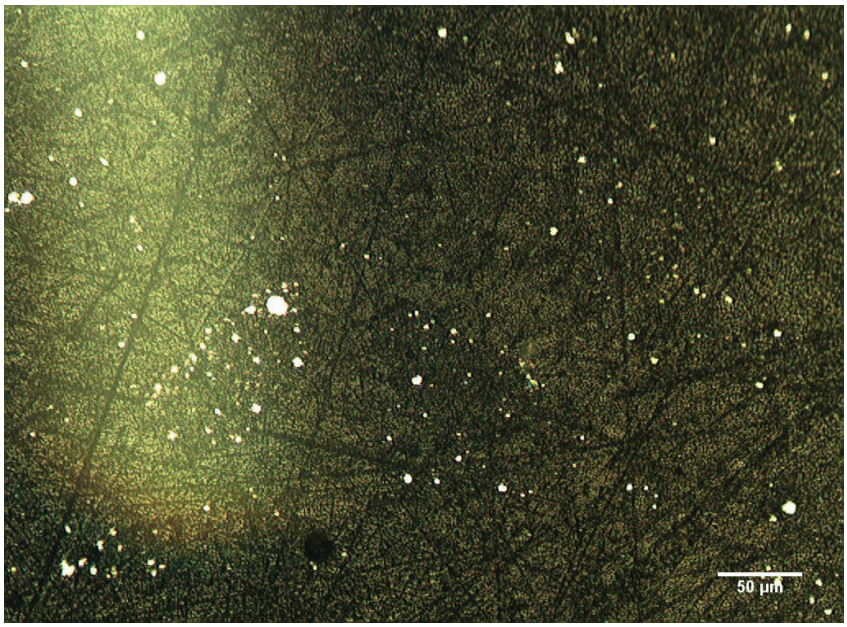

Figure 60 Micrometric dispersion of Fe NPs

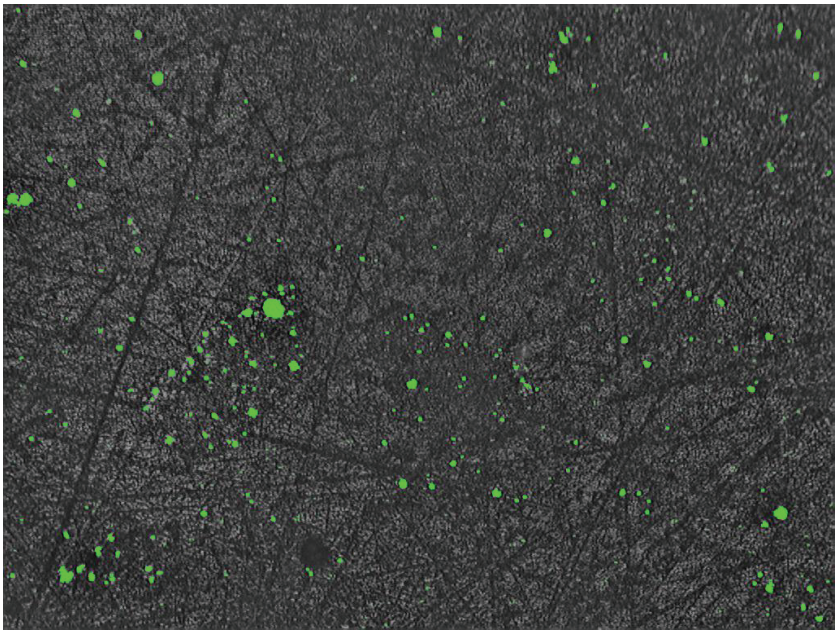

Figure 61 Selection of areas by threshold

Image processing software works particularly well for samples containing Fe filler. There is a high contrast between the polymer matrix and the clusters of NPs (white areas). The image processing is based on the use of a grey value threshold. The sections

of the image, which have a grey scale value below the threshold, are all selected by the software. Consequently, the selections, which are not of a minimum size, are discarded; those sections parts are assumed polymer and not particle. Here, the minimum taken area is $0.79\mu m^2$ (the diameter of the smallest visible cluster taken by optical microscope is around 0.5μm). Around 0.8% of the image is occupied by the white areas. If the white areas are just composed of nanoparticles, it would mean 20% of amount of added Iron NPs is agglomerated.

As 20% of the nanoparticles are situated in non-disperse clumps, it is clear that the dispersion should still be improved. Such an improvement would lead to enhanced shielding effectiveness due to a greater number of functional particles.

4.6 Comparison of calculation models and experimental data

After demonstration of the electromagnetic results, the theoretical models can be verified that according the level at which they are able to predict the electromagnetic compartment of nanocomposites with metallic nanoparticles.

To create the analytical estimation of shielding effectiveness, the effective properties must be generated, that can be done by the mixing models presented in Chapter 2. Neelakanta formula (equations (41) to (44)) is used to calculate the effective permittivity ε_{eff} and conductivity σ_{eff}. Bruggeman's formula given in equation (45,46,47) is also used to estimate the effective material permeability μ_{eff}. The needed parameters for estimation are presented in Table 13.

Table 13 Parameter for analytical estimation

	Fe	*Ni*	*Co*	Fe_3O_4	*Epoxy*	μ_0 ; σ_{Copper} ; ε_0
μ_r	5000	600	250	25	-	$4 \cdot \pi \cdot 10^{-9}\ H/m$
$\sigma\ [S/m]$	$1.041 \cdot 10^7$	$1.443 \cdot 10^7$	$1.603 \cdot 10^7$	25	10^{-14}	$56.6 \cdot 10^6$
ε_r					3.8	$8.85 \cdot 10^{-12}\ F/m$

Equations (30) to (33), common approach, Schelkunoff theory (equation (37)), Colaneri and Shaklette model (equation (36)) and classical good conductor approximation (equations (34) are investigated. As the volume resistivity which is not available is needed for the Simon formalism, this model was excluded. Also, the contribution of multiple reflections is neglected in this formalism; although this simplification would be applicable for only very high amounts of shielding.

In Figure 62, the experimental electromagnetic characterizations data of particles are given in dB units. This facilitates the comparison with models that give the results of shielding effectiveness (SE) in dB units. Iron particles in epoxy resin have the highest overall SE gaining values of around 2.2dB. For both nickel and cobalt, SEs are lower and less stable over the range of frequencies. The iron oxide has the lowest SE with a peak of 1.5dB and having the value of 0.5dB over its range of frequencies.

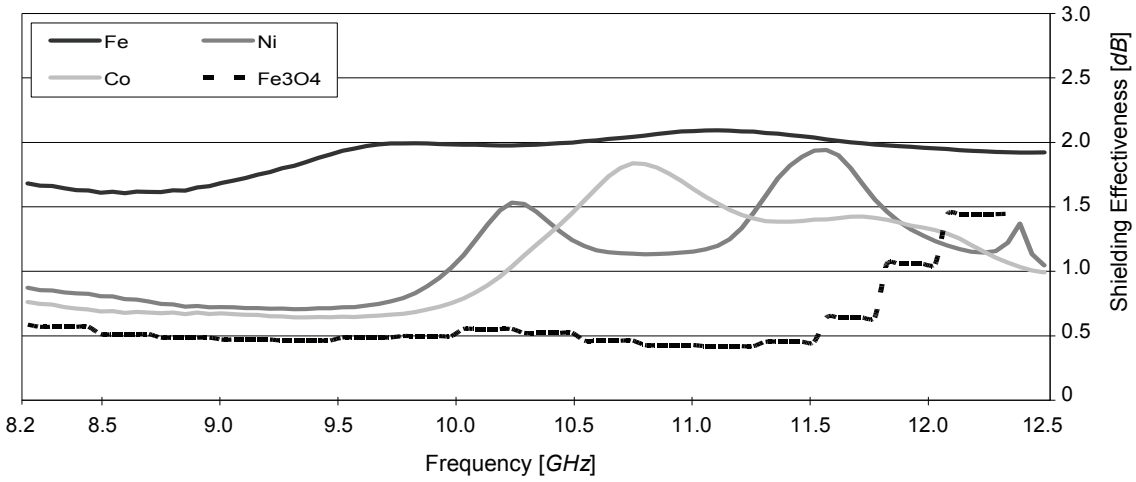

Figure 62 Shielding Effectiveness of different nanocomposites

In Figure 63 the results of the common approach for theoretical calculations of shielding effectiveness are presented. It is shown that the predicted SE are much higher than the experimental data. Based on this model, nickel, cobalt and iron nanocomposites would expose SEs between 50dB and 55dB. Iron oxide fillers should have a lower SE (about 25dB). Though absorption part A of shielding (equation 31) is determined very low at around 2dB and multiple reflections B has a major influence, reflection part R is predicted considerably higher than how it occurs in reality. As a result, this theoretical model is not able to predict the SE of the thin samples with very low loading.

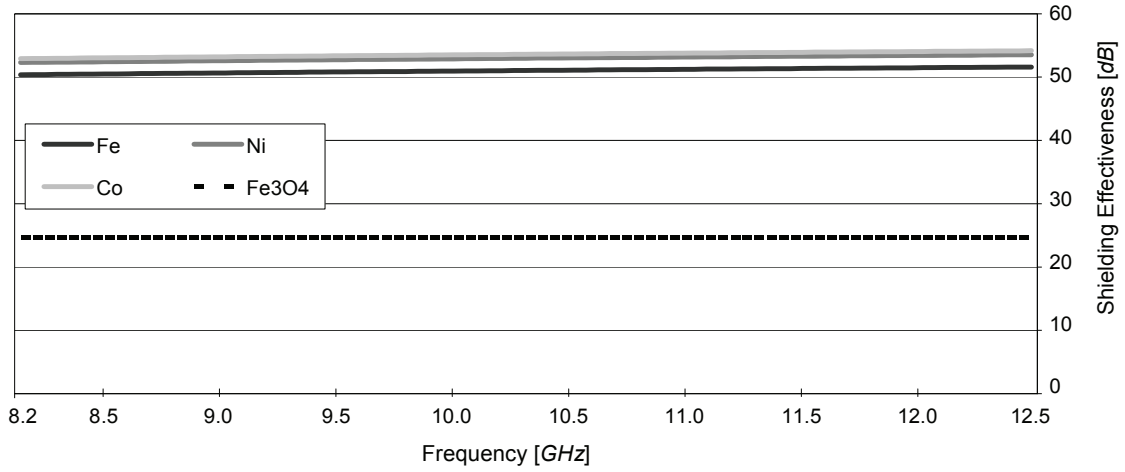

Figure 63 Theoretical Shielding Effectiveness results by Common Approach

Schelkunoff and Colaneri give the same results. The predicted shielding effectiveness is much higher compared to the experimental data. Schelkunoff model expects SE up to 52dB (Figure 64), Colaneri gives SE up to 36dB (Figure 64).

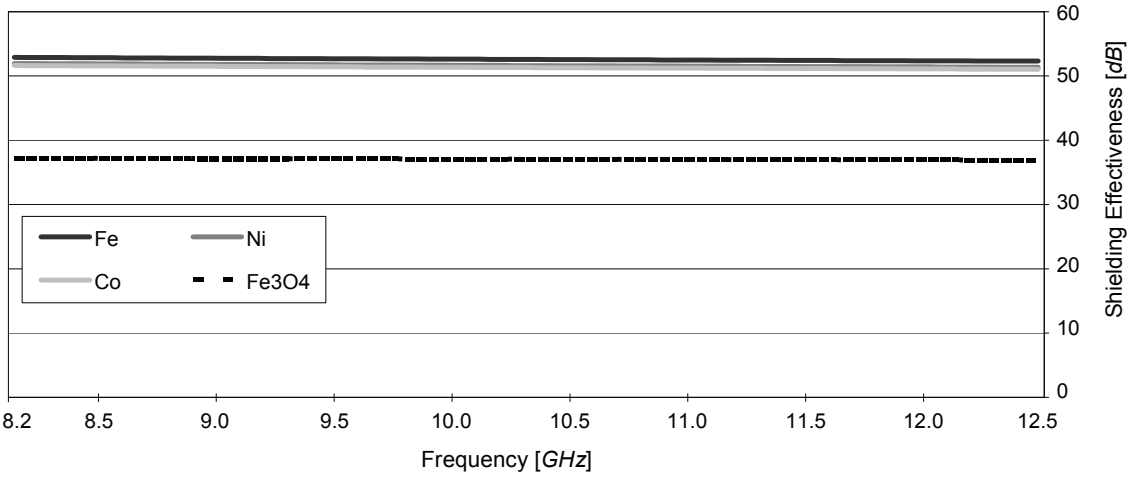

Figure 64 Theoretical Shielding Effectiveness by Schelkunoff model

However for Fe_3O_4, the Colaneri and Shaklette model predicts values quite close for SE, at about *2* to 3dB. It seems to take into account the much lower conductivity and permeability of the iron oxide. But still, it is not able to predict the SE of others. Classical good conductor approximation is not presented as it expects even higher SE values. Most

likely, the range of frequencies is too high and the skin depth is too small for the constraint of precision to be attained for that model.

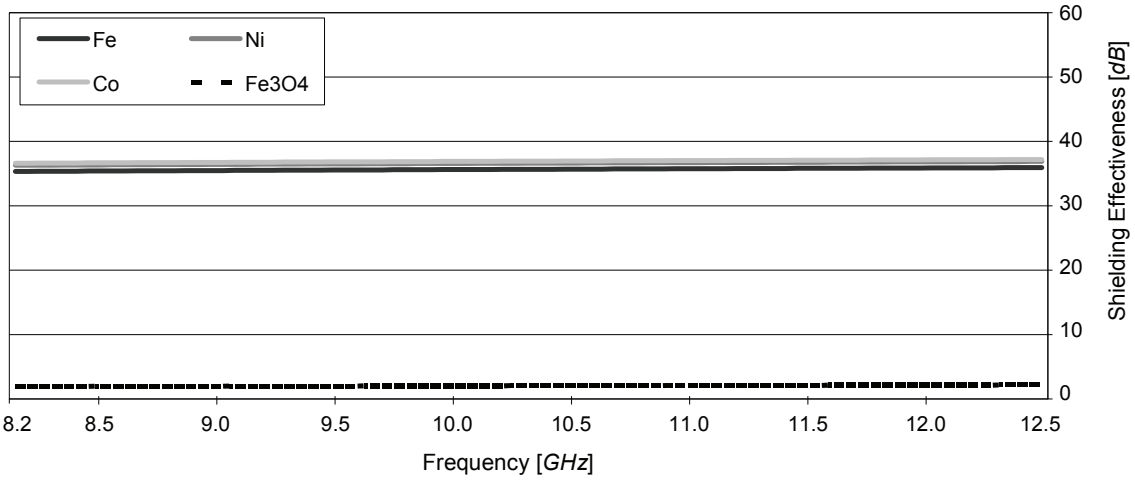

Figure 65 Theoretical Shielding Effectiveness obtained by Colaneri and Shaklette

In general, it is shown that the presented models are not able to predict the shielding effectiveness. As already mentioned the accurate computation of SE with theoretical equations is considered as being a problem and requires more research. In this research, the thickness of samples and loading of particles could be too small. Consequently, SE would be too low to be predicted by the described theoretical models.

4.7 Introducing of Nanoparticles into Carbon Fiber Composites

Introducing of metallic nanoparticles into composite structures that can potentially be used in aerospace applications with the aim of improving absorption is the aim of this chapter. Considering the work that is done to identify the optimum particle for improving EM absorption, here iron particles of 50nm are incorporated into a composite material including a carbon fiber mesh.

Here, the description of composition and fabrication of the carbon fiber composite as well as a results of electromagnetic characterization on absorption, reflection, and total shielding effectiveness are presented.

Fibers are embedded into polymer matrix system to improve the mechanical properties of composites. The fibers offer the high stiffness and the high load capacity of that material; and the role of epoxy resin is to be a support matrix to maintain the fibers in the proper direction and to protect them from environmental effects. Carbon fibers demonstrate high EM reflection. Interaction of fibers with metallic particles in a composite material is an important issue for analysis. Improvement of both total shielding effectiveness and the absorption of electromagnetic energy is expected.

Different fibers (e.g. fiber glass, Kevlar fibers, ceramic fibers, and even natural fibers) are used dependent on the field of application. Strength, stiffness, temperature and humidity behavior, heat expansion, and matrix material compatibility are just some of the selection criteria. From an economical point of view, glass fibers are applied in low loaded structures even if their mechanical properties are weak. However, for high end structures, carbon fiber is usually utilized; it possesses a 5 times higher Young's modulus, a higher tensile strength tolerance, and at the same time has 30% less weight. Thus, carbon has some advantages over other fibers. So here, carbon fibers are embedded into PMC. The polymer phase of PMC would contain metallic nanoparticles for EM shielding. HexTow™ AS4 3000 (from Hexcel) is the common carbon fiber for aerospace applications that is used in this work.

Because of the many advantages, such as economical manufacturing, electromagnetic shielding, and particularly absorption, iron particles of 50nm are selected

to be incorporated into PMCs. As a result, these particles are mixed to a carbon fiber/epoxy resin composite and tested to check on shielding and absorption enhancement.

Exactly the same process as nanocomposite fabrication is used here to mix the particles with the polymer phase. The product is casted into a mold with a layer of carbon fiber within.

As already explained, using 4% volume fraction of metallic nanoparticles would not create the percolation threshold. Considering the fact that the carbon mesh itself takes some space in the composite, the volume fraction of particles is increased to 7% of the epoxy resin component to keep the overall volume fraction. The thickness of sample is 2.2mm, and the composite has a sandwich structure with two epoxy layers on the top and bottom of a layer of carbon fibers. Table 14 presents the matrix composition of the carbon fiber nanocomposite:

Table 14 Composition of matrix material for Carbon Fiber Nanocomposite

	Particles	Chloroform	Coupling Agent	Epoxy	Curing Agent
Weight [g]	2.6	9.77	0.26	2.75	1.38

The reference sample matrix does not contain the particle (just epoxy resin and curing agent). The dimensions of the samples are 50mm x 60mm x 2.2mm and are casted in a silicone rubber mold. In the first step, a layer of epoxy is poured into the mold. As a second step, carbon mesh is placed. And finally, as the third step, another layer of epoxy is poured.

PMC with carbon fiber and metallic particles (b) and reference samples of PMC without metallic particles (a) are shown in Figure 66. According to the applied waveguide flange, after the curing process, the samples are drilled and the side edges are grazed mechanically. By the introduction of iron particles into the composite, the sample takes a black appearance and the carbon mesh inside would not be observable comparing to the reference sample that is shown in Figure 66.

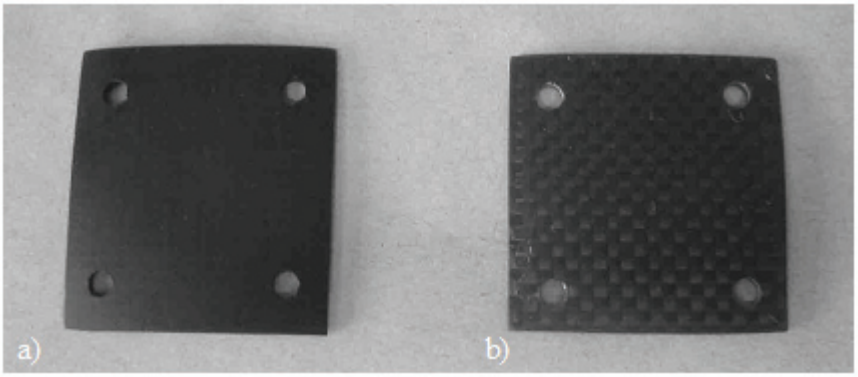

Figure 66 PMC with Carbon Fiber and metallic particles (a) and PMC with just Carbon Fiber Composite (b)

4.7.1 EFFECTS OF NANOPARTICLES ON CARBON FIBER COMPOSITES

Following the same test plan as previously explained, PMCs with carbon fiber and with/without nanoparticles are tested for electromagnetic shielding. The provided data exposes the average of forward and reverse measurements to balance the effects of asymmetry, particularly regarding the carbon layer position within the sample thickness. For a better understanding of the engaged mechanism, the absorption and reflection parts of the shielding are presented individually. To provide a general idea of the EM enhancement generated by the embedding of metallic particles, the absorption, reflection,

and particularly the total shielding effectiveness (SE) of the carbon fiber (nano-) composites are given in *dB* units. Not only is the general shielding effectiveness needed, but also the elevated absorption level is needed to solve the problem of internal reflections. In Figure 67, the electromagnetic test data for the ratio of absorbed or reflected to incident power penetrating the sample are shown. Referring to values of transmitted power ratio in the range of 10^{-4} to 10^{-6}, the total shielding of both samples is very close to 1 and therefore not shown in this figure. In the legends of all figure, 'CarbonMesh' would be the carbon fiber composite material without particle filler, 'CarbonMesh+NanoFe' would be the carbon fiber composite with embedded Iron (*Fe*) particle.

Over the considered range of frequencies (X-band), the reflection and absorption of both samples follow opposing paths. Increasing of absorption is attained by a reduction of reflection and vice versa. The absorbed electromagnetic power of the carbon fiber composite including metallic nanoparticle filler (in the following CFNC - carbon fiber nanocomposite) is detected at around 29% at 8.2GHz increasing approximately linearly to 48% at 12.4GHz. At the same time the reflection part of shielding decreases from 71% (at 8.2GHz) to 52% (at 12.4 GHz) in a similar linear course. The absorption has nearly an identical percentage on total shielding as reflection for the highest mentioned frequency, even if this value is only 29% for the lowest frequency. Then, in increasing frequency, the mechanism of absorption becomes more and more crucial. A very unsteady path over the frequency range is demonstrated for both absorption and reflection of the PMC with carbon fiber. The absorption starts from 10% at 8.2GHz and rises up to a peak of 51% at

10.5GHz, even more than the absorption of PMC with carbon fiber and nanoparticles between 10.1GHz and 10.8GHz.

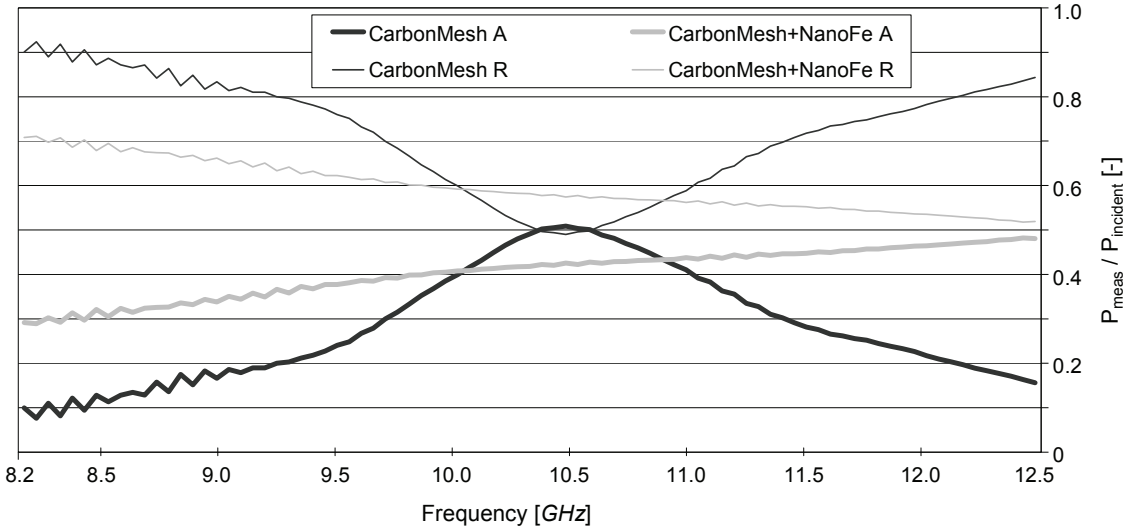

Figure 67 Absorption and reflection for Carbon Fiber Composites with/without particles

However, after that peak, the values fall instantly, down to 15% at 12.4GHz. Contrary to the tendency of absorption, the reflection for PMC with carbon fiber attains a considerable minimum at 10.5GHz of only 49% of field power reflected. Except for the low peak, the reflection of the PMC with carbon fibers is normally higher than for the PMC with carbon fibers and metallic particles, demonstrating the highest levels on the X-band's frequency limits at 8.2GHz (90%) and 12.4GHz (84%).

In Figure 67 and 68, a better picture of the mechanism responsible for shielding for both reflection and absorption in dB is illustrated. Absorption of PMC with carbon fiber with and without particles is shown in Figure 67. As it is demonstrated, absorption for samples with metallic nanoparticles differs from 1.5dB (8.2GHz) to around 3dB at 12.4GHz. A higher level of smoothness of the curve related to PMC with particles comparing to one without is observed. Also, except the peak of PMC without particles at 10.5GHz (over 3dB), the overall level of absorption of PMC with particles is extensively

higher, and demonstrates a considerably more stable performance without any fluctuations over the entire X-band. In addition, the absorption increases for higher frequencies, which is needed mainly for the shortage of shielding effectiveness in higher frequencies of conventional method of shielding with metal mesh.

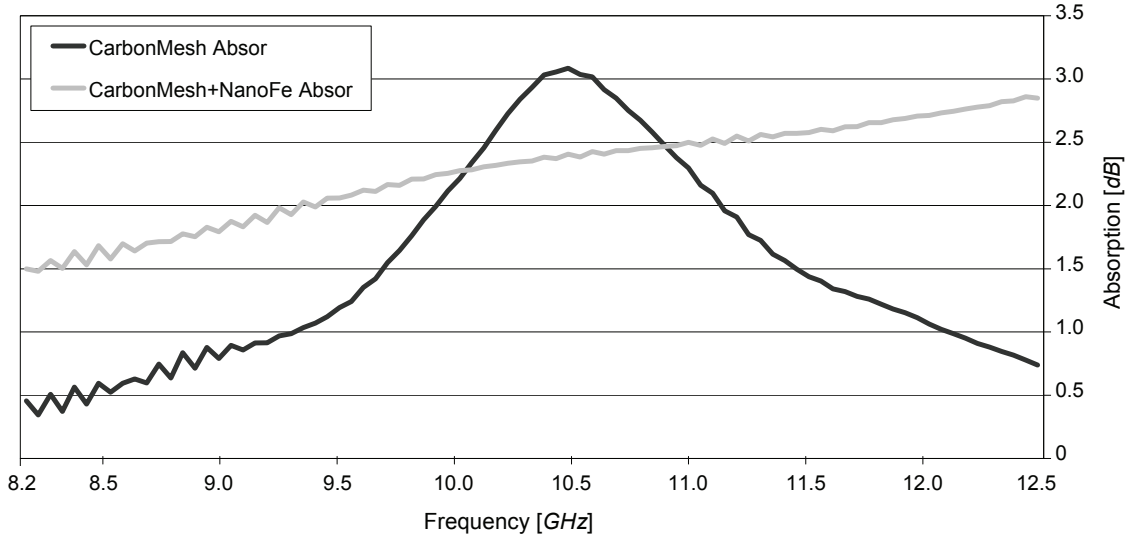

Figure 68 Absorption for Carbon Fiber (Nano-) Composites in dB

Also, there is an ambiguity regarding the emergence of the absorption peak rising up for the composite without particles at about 10.5GHz, which is probably due to the drop-off for reflection values down to 2.9dB (Figure 68). This drop-off reduces the general reflection of the PMC without particles considerably (marked at about 10dB at 8.2GHz and again 8dB at 12.4GHz). On the other hand, a straight-lined trend of the reflection of PMC with particles reduces from a high at 8.2GHz (5.4dB) to the low at 12.4GHz (3.2dB).

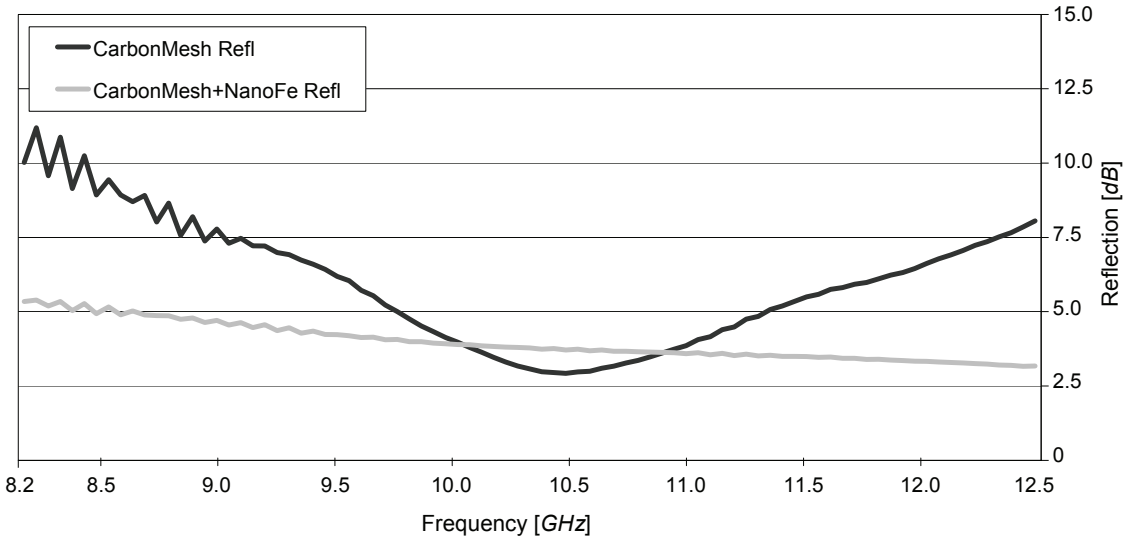

Figure 69 Reflection for Carbon Fiber (Nano-) Composites in dB

Considering the need of preventing any re-reflection inside cabin and improving the level of absorption as much as possible, the lower general level of reflection of PMC with carbon and particles would be evaluated positively (Figure 69). The SE of PMC with particles is, besides the frequency between 8.2GHz and 8.4GHz, higher for the whole X-band. Beginning at 51dB at 8.2GHz and having an overall high at 8.5GHz (53dB), the total SE for the PMC with carbon fiber and particles attains a very smooth trend over the frequency range without any drop-offs or peaks. A steady-going reduction is exposed until the low of 43dB at the highest mentioned frequency (12.4GHz).

Contrarily, the PMC without metallic particle attains a sharp reduction in SE from 66dB to 41dB in the first 0.7GHz of the frequency range and yet demonstrates a fall to only 30dB at 10.1GHz. Even if it rises again (up to 38dB at 11.7GHz) for the second half of the X-band, it no longer attains the values of the PMC with particles, which in turn is able to flatten the convexity in SE of the PMC mainly in the middle section of the X-band and to provide a more continuously constant shielding.

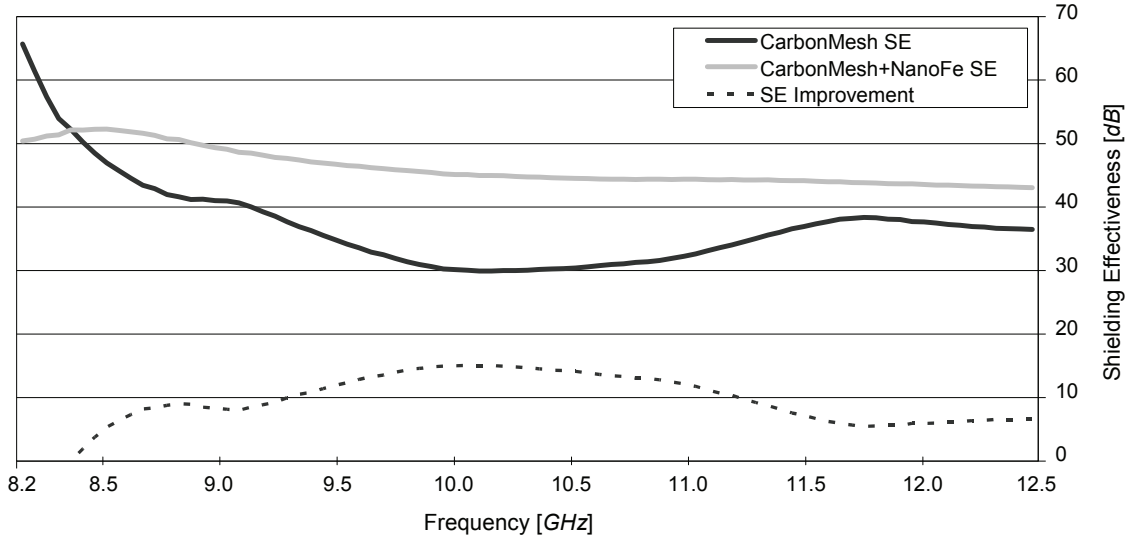

Figure 70 Total Shielding Effectiveness for Carbon Fiber (Nano-) Composites

The dotted line in Figure 70 demonstrates the SE enhancement through the embedding of iron particles to the carbon fiber composite which has a high of *15dB* at *10.1GHz*. Also it is shown that an increasing is permitted for almost the whole range of frequencies of the X-band.

Chapter 5 Conclusion

To conclude this thesis, a review of the work is presented that consists of the research that is performed and the results that are attained. Suggestions for further research on the subject are given as well.

5.1 Summary of the work

Because of the expected progress of electronic technology, the electromagnetic interference generated by each different communication, entertainment, and surveillance technology create a perturbed environment for the functioning of an aircraft. The onboard and offboard electromagnetic sources interfere with the systems (e.g. navigation) of aircraft. Due to the high conductivity, metallic aircraft face these electromagnetic (EM) fields as semi Faraday cages, and consequently are able to provide an acceptable level of shielding to reflect and absorb the radiation. But polymer matrix composites (PMCs) are not able to provide such a high shielding, and as a result are very susceptible to EM fields. To overcome this deficiency, metal meshes (in different forms: e.g. expanded copper foil) are selected as the practical method of protection for PMCs. However, in addition to the weight issue, complexity in fabrication, and corrosion behavior, major reduction of the effectiveness at high frequencies is observed. Metallic nanoparticles have a great potential to fill this shortcoming.

A comparative investigation of the different metallic nanoparticles (with the highest magnetic loss) was performed. Finding an optimal combination of type and size of particle for electromagnetic shielding in higher frequencies (X-band) has been

followed as the main goal of this work. The focus has been directed to the high absorption capacity of ferromagnetic metallic nanoparticles with high magnetic loss. Cobalt, iron, nickel and iron oxide are the main particles that are considered in this work. The influence of different particle sizes related to single domain appearance of ferromagnetic particles was considered. Super paramagnetic regimes due to high sensitivity to temperature have been avoided.

Iron nanoparticles with size of 25nm were found to demonstrate the highest absorption capacity of all analyzed materials. However, due to their high simultaneous reflection of electromagnetic fields, which are not guaranteed, iron particles with size of 50nm were selected as the optimum particle for shielding. As a result, iron particles with a size of 50nm were chosen to be embedded in PMCs with carbon fibers. Compared to 25nm, advantages like less reflection, the equal levels of absorption, and simplicity in manipulation are encouraging factors for the use 50nm for shielding.

By using ferromagnetic nanoparticles, total shielding effectiveness increases up to 15dB in a carbon fiber composite (increasing from 30dB without particles to 45dB with particles). The enhancement is considered for the whole X-band (range frequency from 8.4GHz to 12.4GHz). The augmentation is caused by reduction in reflection and an increase of the absorption part of shielding. This aspect of the mentioned particle has a great potential for facing the electromagnetic interferences generated by onboard passenger electronic devices.

Also, microscope results show an acceptable level of uniformity in fabricated samples. The fraction of agglomerated particles (in the case of iron) is estimated to be around 20% for dimensions between 0.5µm to 30µm. These agglomerations do not

necessarily represent the waste of particles that do not contribute to the performance of absorption. If four point electrical conductivity measurements are performed, it can be confirmed that the prepared sample does not increase the conductivity.

Thermal analysis confirms that the using of metallic NPs (Fe, Ni, Co, Fe3O4) in epoxy resin nearly do not change the thermal behavior of the polymer. Glass transition and degradation temperature are fairly close to pure epoxy for most of samples (with the exception of cobalt). However, thermal stability can be increased with the high amount of char yield due to the weight fraction of metallic particles. Specific heat capacities of epoxy resin with iron, nickel, and cobalt are lower than pure resin. As a result, the introductions of selected iron particles with a size of 50nm improve thermal stability and do not change the thermal properties like glass transition and degradation temperature of pure epoxy. Based on the four points bending test, the mechanical properties of pure epoxy is not changed by adding iron nanoparticles (with the exception of iron oxide). Further mechanical tests must be performed to give a better understanding of mechanical compartments of nanocomposites particularly, with iron particles.

Considering all the above characterizations in terms of electromagnetic, thermal analysis, mechanical testing and microscopy investigation, it can be claimed that Iron nanoparticles (with size of 50nm) are the best candidate to be used onboard for electromagnetic shielding of composite aircrafts.

5.2 Further directions

In this thesis, the effect of different metallic nanoparticles in improving the electromagnetic shielding of Polymer Matrix Composites (PMCs) is shown for the range

of frequencies covered by the X-band. Iron particles with a size of 50nm are shown to have the best electromagnetic, thermal, and mechanical properties. Also, the effect of adding metallic particles for lower frequencies up to a few GHz is given in Appendix A. More investigation with the direction proposed in this work should be performed in L-band (1-2 GHz, for long range air traffic control and surveillance), S-band (2-4GHz, moderate range surveillance, terminal air traffic, long range weather, and marine radar) and finally C-band (4-8 GHz, satellite transponders, and long range tracking). Additional experiments based on varying particle loadings and comparing the effects to the embedding of conventional methods of shielding in composites can be performed to give a better understanding of electromagnetic shielding through metallic nanocomposites.

To continue this work, there are five possible tasks that could be performed: (1) theoretical investigation on shielding with nanocomposites; (2) manufacturing of nanocomposite; (3) structural analysis of the nanocomposites; (4) numerical simulations of nanocomposites; (5) characterization of nanocomposites.

References

[1] E. F. Knott, J. F. Shaffer, M. T. Tully, Radar Cross Section, 2nd edition, SciTech Publishing, New York (2004)

[2] Montrose, M. I., EMC and the Printed Circuit Board. New York: Institute of Electrical and Electronics Engineers, (1999)

[3] M.A. Shooman, Study of occurrence rates of electromagnetic interference (EMI) to aircraft with a focus on HIRF (external) high intensity radiated fields, NASA contractor report 194895, (1994)

[4] S.V. Koppen et al, Electromagnetic Interference Assessment of CDMA and GSM Wireless Phones to aircraft navigation radios, NASA Technical Reports Server (2002)

[5] R.W. Borek, Electromagnetic Interference/ Electromagnetic Compatibility, SPARTA, Inc., RTO-AG-300-V14

[6] K. J. Moeller, K. L. Dudley, C. C. Quach, S. V. Koppen, In-Flight Characterization of the Electromagnetic Environment Inside an Airliner, NASA/TP-2001-210831, 2001

[7] T.X. Nguyen, J.J. Mielnik, Small Aircraft RF Interference Path Loss Measurements, NASA/TP-2007-214891 (2007)

[8] www.aviationbusinessindex.com/listings.asp?make=LEARJET&model=35A

[9] C.s A. Grosvenor, R. Johnk, D. Novotny, D. Camell, G. Koepke, N. Canales, Electromagnetic Penetration Studies for Three Different Aircraft, IEEE 978-1-4244-4267-6, 2009

[10] X.C. Tong, Advanced Materials and Design for Electromagnetic Interference Shielding, CRC Press (2009)

[11] J.W. Gooch, J.K. Daher, Electromagnetic Shielding and Corrosion Protection for Aerospace Vehicles, Springer (2007)

[12] M.H. Al-Saleh, Electromagnetic interference shielding mechanisms of CNT/polymer composites, Carbon 47 (2009)

[13] J.B. Jackson, Classical electromagnetic, John Wiley & Sons, New York, 3rd edition (1999)

[14] J.W. Gooch, J.K. Daher, Electromagnetic Shielding and Corrosion Protection for Aerospace Vehicles, Springer (2007)

[15] N.C. Das, Electromagnetic interference shielding of carbon nanotube/ethylene vinyl acetate composites, J Material Science 43 (2008)

[16] S. Rea et al., Shielding Effectiveness of Woven Carbon Fiber Composite Materials for Aerospace Applications, 16th European EMC Conference (2005)

[17] D.R. White, M. Mardiguian, A Handbook Series on Electromagnetic Interference and Compatibility - Electromagnetic Shielding, Control Technologies, Inc. (1988)

[18] H. Ebneth, et al., Metallized carbon fibers and composite materials containing these fibers, US Patent 4,481,249 (1984)

[19] D.H. McClenahan, J. A. Plumer Graphite fiber reinforced laminate structure capable of withstanding lightning strikes, US Patent 4,448,838 (1984)

[20] P. Dixon, May. Dampening cavity resonance using absorber material. RF Design, pp. 16–20. http://rfdesign.com/mag/0405rfdf1.pdf (2004)

[21] Sony. Sony's electromagnetic wave absorber reduces EMC and SAR problem. http://www.sony.net/Products/SC-HP/cx_news/vol25/pdf/emcstw.pdf (2008)

[22] J. T.Gear, August. Microwave absorbers manage military electronics RF interference. RF Design, pp. 6–9. http://rfdesign.com/mag/08deff1.pdf (2004)

[23] Saville, P. 2005. A review of optimization techniques for layered radar absorbing materials (Technical memorandum 2005-003). Defence R&D Canada. http://pubs.drdc.gc.ca/ PDFS/unc57/p523186.pdf

[24] F. Mayer, High frequency broadband absorption structures, US Patent 5,872,534. (1999)

[25] W. H. Emerson, Electromagnetic wave absorbers and anechoic chambers through the years, IEEE Transactions on Antennas and Propagation 21(4): 484–490 (1973)

[26] Halpern, O., M. H. J. Johnson, and R.W. Wright, Isotropic absorbing layers. US Patent 2,951,247 (1960)

[27] Jones, A. K., and E. R. Wooding, A multilayer microwave absorber. IEEE Transactions on Antennas and Propagation 12(4): 508–509 (1964)

[28] P. Toneguzzo, G. Viau, O. Archer, F. Guillet, E. Bruneton, F. Fievet Vincent, F. Fievet, CoNi and FeCoNi fine particles prepared by the polyol process: Physico-

chemical characterization and dynamic magnetic properties, Journal of Material Science, 35, 3767-3784 (2000)

[29] Soshin Chikasumi, "Physics of Magnetism" John Wiley and Sons, (1964).

[30] B. D. Cullity, Introduction to Magnetic Materials, Addison-Wesley Publishing, (1972).

[31] Nicola A. Spaldn, Magnetic Materials: Fundamentals and Device Applications, Cambridge University Press, (2003)

[32] William D. Callister, Jr., Material Science and Engineering: An Introduction, John Wiley & Sons, 2000.

[33] Robert C. O' Handley, Modern Magnetic Materials: Principles and Applications, Wiley & Sons, 2000.

[34] J.C. Anderson, Magnetism and Magnetic Materials, Chapman and Hall Ltd. (1968).

[35] Kenneth J. Klabunde, Nanoscale Materials in Chemistry, John & Sons, Inc. (2001).

[36] X. Batlle, A. Labarta, Finite-size effects in fine particles: magnetic and transport properties J. Phys. D, 35, R15 (2002)

[37] C. Kittel, Excitation of spin waves in a ferromagnet by a uniform RF field, Phys. Rev., 110 (6), 1295-1297 (1958)

[38] C. Kittel, On the theory of ferromagnetic resonance absorption, Phys. Rev. 37 (2), 155-161 (1948)

[39] C. E. Patton, Dynamic process in magnetic thin films domain wall motion and ferromagnetic resonance, PhD thesis, Cal Tech (1967)

[40] D.R.J. White, Electromagnetic shielding materials and performance, Don White Consultants, Inc. (1980)

[41] W.G. Duff, Fundamental of electromagnetic compatibility, A handbook series of electromagnetic interference and compatibility, vol. 1 (1988)

[42] N.C. Das et al., Electromagnetic interference shielding effectiveness of carbon black and carbon filled EVA and NR based composites, Composites: Part A 31 (2000)

[43] C. J. von Klemperer, Composite electromagnetic interference shielding materials for aerospace applications, Composite Structures 91 (2009)

[44] S. Yang et al., Electromagnetic interference shielding effectiveness of carbon nanofiber-LCP composites, Composites: Part A 36 (2005)

[45] J. L. Wojkiewicz et al., Electromagnetic shielding properties of polyaniline composites, Synthetic Metal (2003)

[46] Bruggeman, DAG Dielectric constant and conductivity of mixtures of isotropic materials Annals of Physics, 24 , 636 – 679 (1935)

[47] M. Y. Koledintseva et al., A Maxwell Garnett Model for dielectric mixtures containing conducting particles at optical frequencies, Progress in Electromagnetic research, Pier 63 (2006)

[48] P.S. Neelakanta, Handbook of electromagnetic materials: monolithic and composite versions and their applications, CRC-Press (1995)

[49] M. Y. Koledintseva et al., Modeling of ferrite-based materials for shielding enclosures, Journal of Magnetism and Magnetic Materials 321 (2009)

[50] M. Y. Koledintseva et al., Modeling of shielding composite materials and structures for microwave frequencies, Progress in Electromagnetic Research, PIER 15 (2009)

[51] S. Chikazumi et al., Physics of magnetic fluids, Journal of Magnetism and Magnetic Materials 65 (1987)

[52] A.-H. Lu et al.; Angew, Nanoengineering of a magnetically separable hydrogenation catalyst, Chem. Int. Ed. 43 (2004)

[53] A. K. Gupta, M. Gupta, Synthesis and surface engineering of iron oxide nanoparticles for biomedical applications, Biomaterials vol. 26 (2005)

[54] S. Mornet et al., Magnetic nanoparticle design for medical applications, Prog. Solid State Chem. vol 34 (2006)

[55] A.C. Pierre, Introduction to Sol–Gel Processing, Kluwer Academic Publishers, Boston, (1998)

[56] M. Jalali, R. Wuthrich, Electromagnetic Shielding of Composite Materials Using Electrochemical Discharge Nanoparticles, EUROEM, Switzerland (2008)

[57] H. Fizeau, L. Foucault. Recherches sur l'intensité de la lumière émise par le

charbon dans l'expérience de davy. Annales de Chimie et de Physique XI, 3:97, (1844)

[58] Ch. Guilpin and J. Garbaz-Olivier, J. Chim. Phys. Phys-Chim. Biol. 75, p. 723. (1978)

[59] H. Vogt and J. Thonstad, J. Appl. Electrochem. 32 (2002), p. 241

[60] M. Jalali, P. Maillard, R. Wüthrich, Towards a Better Understanding of Glass Gravity-Feed Micro-hole Drilling with Electrochemical Discharges, Journal of Micromechanics and Microengineering (2009)

[61] H. Gleiter, Prog. Mater. Sci. 33, 223 (1989)

[62] T. Yamamoto, J. Mazumder, Nanostruct. Mater. 7, 305 (1996)

[63] Y. Champion, J. Bigot, Nanostruct. Mater. 10, 1097 (1998)

[64] W. Chang, G. Skandan, S.C. Danforth, B.H. Kear, Nanostruct. Mater. 4, 507. (1994)

[65] J. Karthikeyan, C.C. Berndt J. Tikkanen, J. Y. Wang, A.H. King, H. Herman, Nanostruct. Mater. 8, 61 (1997).

[66] G. L. Messing, S. C. Zhang, G. V. Jayanthi, J. Am. Ceram. Soc. 76, 2707 (1993)

[67] Reinmann R, Akram M, Temporal investigation of a fast spark discharge in chemically inert gases. J Phys D: Appl Phys 30:1125–113, (1997)

[68] Reinmann R, Akram M, Temporal investigation of a fast spark discharge in chemically inert gases. J Phys D: Appl Phys 30:1125–113 (1997)

[69] http://www.unionprocess.com

[70] Journal of Alloys and Compounds Volume 397, Issues 1-2, 19 July, Pages 276-281 (2005)

[71] M. Jalali, A.G. Terpstra, R. Wuthrich, Fabrication of Metallic Nanoparticles through Waste of Micro-EDM, EUSPEN, San Sebastian, Spain (2009)

[72] J. L. Dormann et al., Magnetic relaxation in fineparticle systems, Adv. Chem. Phys., vol. 98 (1997)

[73] J. L. Dormann et al., Magnetic relaxation in fineparticle systems, Adv. Chem. Phys., vol. 98 (1997)

[74] S.V. Koppen et al., Electromagnetic Interference Assessment of CDMA and GSM Wireless Phones to aircraft navigation radios, NASA Technical Reports Server (2002)

[75] M. Q. Zhang, H. M. Zeng; Olabisi O, Conducting thermoplastics composites, Handbook of thermoplastics. New York: Marcel Dekker, Inc. (1997)

[76] Gonon P, Boudefel A. Electrical properties of epoxy/silver nanocomposites. J Appl Phys (2006)

[77] Y. Longa et al., Electrical and magnetic properties of polyaniline/Fe3O4 nanostructures, Physica B 370 (2005)

[78] D. I. Tee et al., Effect of silane-based coupling agent on the properties of silver nanoparticles filled epoxy composites, Composites Science and Technology 67 (2007)

[79] M. Z. Wu et al., Microwave absorption properties of the core-shell-type iron and nickel nanoparticles, Appl. Phys. Lett. 80 (2002)

[80] S. Singha; M. J. Thomas, Dielectric Properties of Epoxy Nanocomposites, IEEE Transactions on Dielectrics and Electrical Insulation Vol. 15, No. 1 (2008)

[81] J. A. Catrysseet al., Correlation between Shielding Effectiveness Measurements and Alternative Methods for Characterization of Shielding Materials, IEEE Trans EMC, vol. 35, no. 4 (1993)

[82] Standard Test Method for Measuring the Electromagnetic Shielding Effectiveness of Planar Materials, ASTM D-4935-99.

[83] Y. K. Hong et al. , Method and apparatus to measure electromagnetic interference shielding efficiency and its shielding characteristics in broadband frequency ranges, Review of scientific instruments, vol. 74, no. 2 (2003)

[84] M.S. Sarto, A. Tamburrano, Innovative Test Method for the Shielding Effectiveness Measurement of Conductive Thin Films in a Wide Frequency Range, IEEE Trans. EMC, vol. 48, no. 2, (2006)

[85] M. Badic et al., Electromagnetic Characterization of Conductive Magnetic/Non-Magnetic Shielding Materials, IEEE Trans. EMC, vol. 1 (2005)

[86] http://www.fischercc.com/Secondary_Pages/Instrumentation/TEM_ Cells.htm

[87] Military Standard Attenuation Measurement for enclosures, Electromagnetic Shielding, for electronic test purposes, MIL-STD-285

[88] P. Wilson, M. Ma, A study of Techniques for measuring the Electromagnetic Shielding Effectiveness of Materials, National Bureau of Standards Technical Note 1095 (1986)

[89] Y. Yang et al., Novel Carbon Nanotube-Polystyrene Foam Composites for Electromagnetic Interference Shielding, Nano Letters vol. 5, No. 11 (2005)

[90] T. Kuphaldt, Lessons in Electric Circuits, vol. 2, Sixth Edition (2007)

[91] M. Robinson et al., Shielding effectiveness of a rectangular enclosure with a rectangular aperture, Electronics Letters vol. 32, no. 17 (1996)

[92] "http://www.eia.org", Electronic Industries Association (USA)

[93] Thru-Reflect-Line: An improved technique for calibrating the dual six-port automatic network analyzer", IEEE Transactions on Microwave theory and Technique, vol. MTT27-12, no. 12 (1979)

[94] W. T. Coffey, D. S. F. Crothers, J. L. Dormann, Y. P. Kamykov, W. Wernsdorfer, Thermally activated relaxation time of a single domain ferromagnetic particle subjected to a uniform field at an oblique angle to the easy axis: Comparison with experimental observation, Physical Review Letters, Vol. 80, pp. 5655-5658 (1998)

[95] Bernhard Wunderlich, Thermal Analysis, Academic Press (1990)

[96] Calorimetry and Thermal Analysis of Polymers, by V. B. F. Mathot, Hanser (1993)

[97] ASTM D6272−10 Standard Test Method for Flexural Properties of Unreinforced and Reinforced Plastics and Electrical Insulating Materials by Four-Point Bending1

[98] J. Als-Nielsen, D. McMorrow, Elements of Modern X-Ray Physics, Wiley (2001)

[99] D. M. Moore, R. C. Reynolds, X-ray Diffraction and the Identification and Analysis of Clay Minerals, Oxford University Press (1997)

[100] R.W.G Wyckoff, Crystal Structures 1, Interscience Publishers (1963)

[101] Jordan J., Jacob K. I., Tannenbaum R., Sharaf M.A., Jasiuk I., Experimental trends in polymer nanocomposites - a review, Mater. Sci. Eng., 393, 1-11 (2005)

[102] Zhu J., Wei S., Ryu J., Sun L., Luo Z., Guo Z., Epoxy Nanocomposites Reinforced with Core-Shell Structured Fe@FeO Nanoparticles: Fabrication and Property Analysis, ACS Applied Materials & Interfaces, 2, 2100-2107. (2010)

[103] Chiang C. L., Chang R. C., Chiu Y. C., Thermal stability and degradation kinetics of novel organic/inorganic epoxy hybrid containing nitrogen/silicon/phosphorus by sol–gel method, , Thermochim Acta 453 (2) , pp. 97–104 (2007)

[104] R.W.G Wyckoff, Crystal Structures 1, Interscience Publishers (1963)

[105] American Mineralogist Crystal Structure Database (AMCSD), http://rruff.geo.arizona.edu/AMS/amcsd.php

[106] M. Abdullah, Derivation of Scherrer Relation Using an Approach in Basic Physics Course, J. Nano Saintek. Vol. 1 No. 1, (2008)

[107] R. Kainhofer, One way to get the Scherrer formula for size broadening, TU Vienna, (2000)

[108] A. L. Patterson, The scherrer formula for X-ray particle size determination, Physical Review Online Archive (1939)

[109] E. Vallat-Sauvain, Evolution of the microstructure in microcrystalline silicon prepared by very high frequency glow-discharge using hydrogen dilution, J. Appl. Phys. 87 (2000)

[110] Wu L. Z., Ding J., Jiang H. B., Chen L. F., Ong C. K., Particle size influence to the microwave properties of iron based magnetic particulate composites, , Journal of Magnetism and Magnetic Materials, 285, pp. 233-39 (2005)

[111] Goya G. F. , Lima E. Jr., Arelaro A. D. , Torres T. , Rechenberg H. R. , Rossi L., Marquina C., Ibarra M. R., Magnetic Hyperthermia With Fe3O4 Nanoparticles: The Influence of Particle Size on Energy Absorption, IEEE Trans. Magn., vol. 44, pp. 4444 (2008)

[112] S. Schwyn, E. Garwin, A. Schmidt-Ott, Technical Note, Aerosol Generation by Spark Discharge, J.Aerosol Sci., Vol. 19, No. 5, pp. 639-642 (1988)

Appendix A

Here, the possibility of using metallic nanoparticles to improve the conductivity, and as a result, the electromagnetic reflection, of polymer matrix composites (PMCs) is discussed. For the range of frequency 30MHz-1.5GHz, the standard method of ASTM 4935 can be chosen to test the samples for their EM shielding effectiveness mainly in terms of reflection. It is important to compare materials tested using the shielding effectiveness test under the same conditions. Conditions such as angle of incidence and polarization of waves are often omitted or are not known, but are essential factors in influencing the results. Shielding with particles can be applied through different methods (e.g. mixing by polymer phase, using in a paint on surface of PMCs or deposition on fibers). Here, the possibility of deposition of particles on fibers by different methods of particle production is discussed.

By following the method of electrochemical discharge ECD, the obtained liquid at the end of process should be poured on carbon fibers and left to be dried. As a result, the clusters of metallic particles are deposited on carbon fibers. Here, the steps of shielding by ECD are explained (Figure 71):

1. following discharge process of ECD
2. pouring the obtained liquid of ECD on the carbon mesh which would be used in the composite.

3. drying the sample to attain the carbon mesh with the clusters of metallic particles.

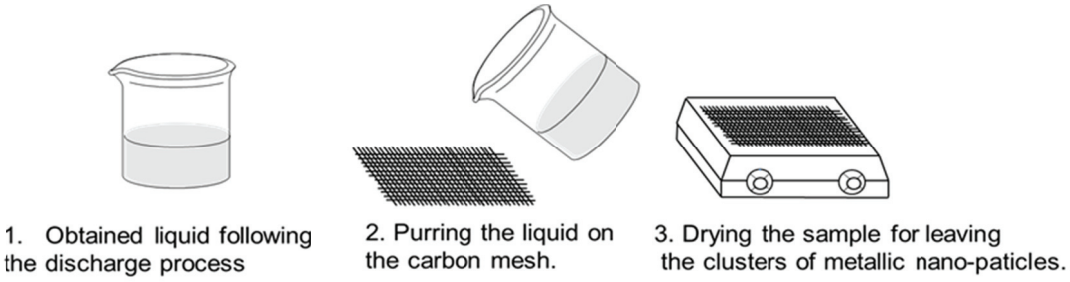

Figure 71 Main steps to deposit metallic nanoaprticles on carbon fiber

Carbon fiber with deposited metallic nanoparticles is cut into the needed dimensions for ASTM 4935 and used in the conventional process of composite fabrication. Here, a simple structure of a sandwich is fabricated inside silicon rubber mold (as shown in Figure 72): epoxy/carbon fiber/epoxy. ECD is not the only method that can be used for direct deposition of nanoparticles on carbon fibers. Spark Discharge Generation can also be used for this purpose. By placing the carbon fibers in exposed flange, the particles would be accumulated automatically on the fibers creating the clusters of nanoparticles, and consequently increasing the conductivity and providing very high reflection (Figure 73).

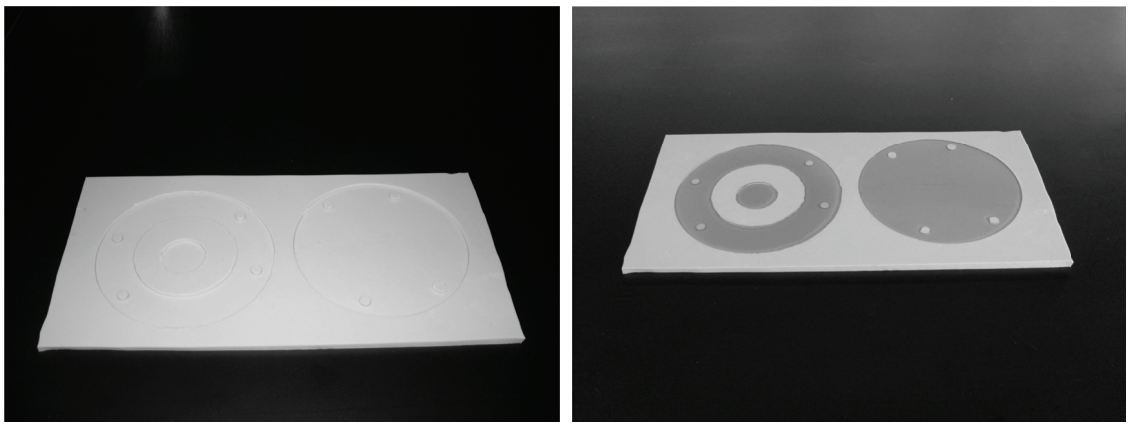

Figure 72 (left) Fabricated mold for ASTM 4935 (right) Mold filled by fabricated sample (epoxy)

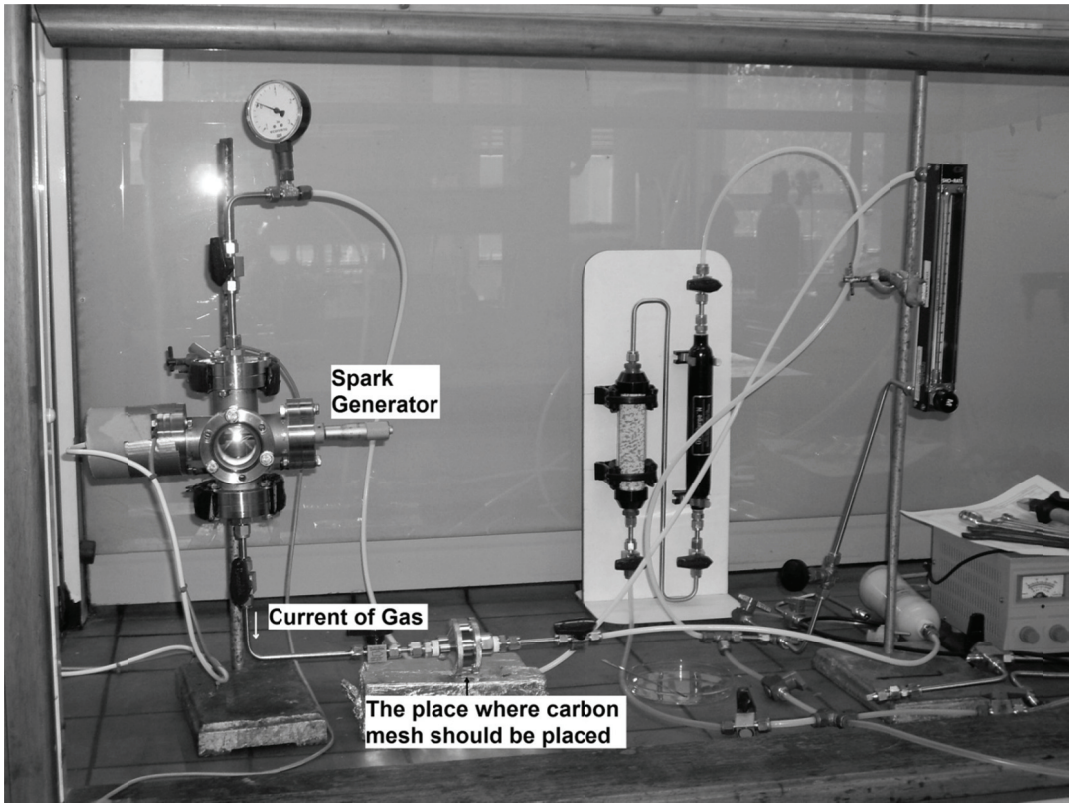

Figure 73 Spark Discharge Generation Test Setup [112]

Also at the final step of chemical production of metallic nanoparticles, instead of drying the liquid to get the particles, the liquid can be sprayed on the carbon fiber, and the deposition of clusters of metallic nanoparticles on fibers will occur (Figure 74).

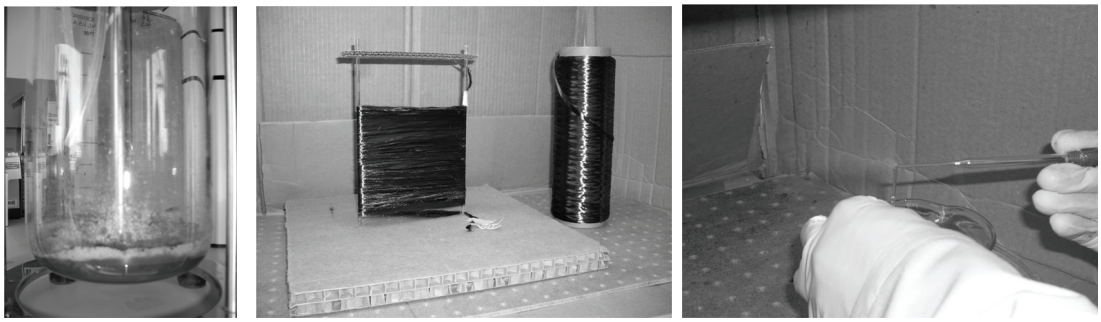

Figure 74 (left): the obtained liquid at the end of the chemical production of metallic nanoparticles, (middle): prepared installation for deposition of liquid containing particles, (right) spraying the liquid containing particles toward carbon fibers.

The final product of composite containing (epoxy/carbon fiber/epoxy) with its expected dimensions is shown in Figure 75.

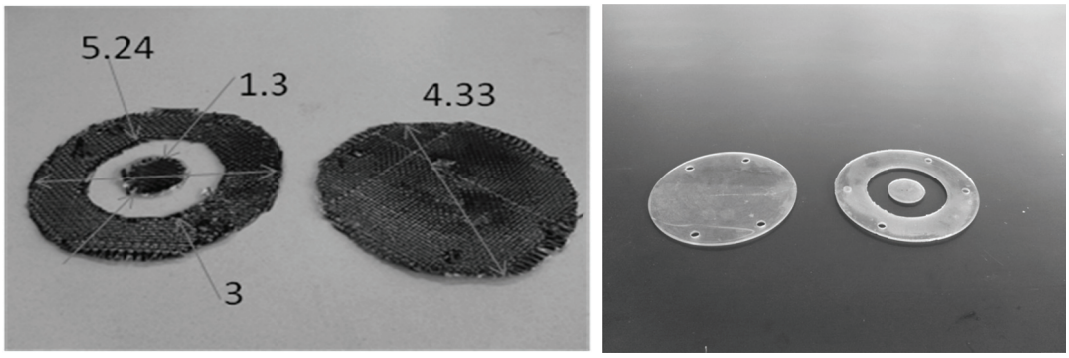

Figure 75 (left) Dimensions for reference and load disks (inch) of (epoxy/carbon/epoxy)

Shielding effectiveness is calculated by subtracting the average of the three load samples from the reference sample. SE has a negative values if less power is received with the material present than when it is absent. The uncertainty in measurement can be a function of thematerial, losses throughout transmission line path, dynamic range of the measurement system, and the accuracy of the equipment. To perform our experiments, a network analyzer (e.g. HP 8752), shielded cables, a Faraday cage, and test fixture support are used (Figure 76). This test measures the net or total SE caused by reflection and absorption.

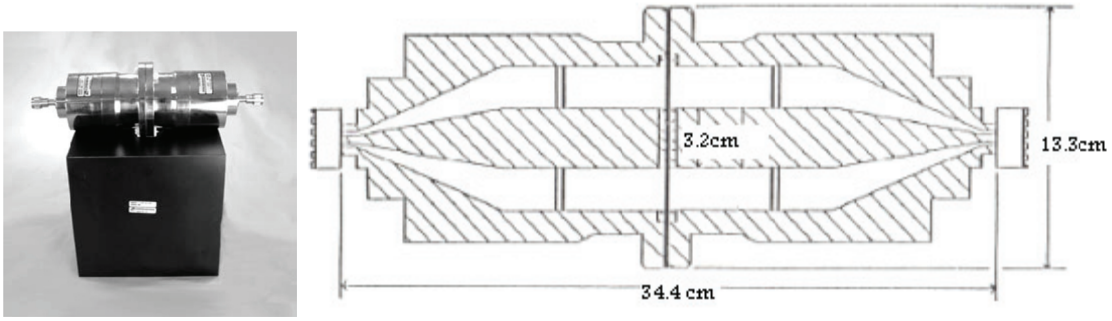

Figure 76 Cross Sectional View of Transmission Test Apparatus

The network Analyzer would be able to generate a sinusoidal signal over the desired portion of the frequency range of 30 MHz to 1.5 GHz. A50-ohm output impedance is needed to minimize reflections due to mismatches. Cables and connectors are devices for connecting power between specific components without causing interference with other components. The cables should have a50-ohm characteristic impedance. Impedance is the degree to which an electronic component impedes the flow of current (it is a frequency dependent quantity and is generally called resistance). Also double-shielded cables should be used, because they provide lower leakage than single shielded cables. No connectors should be used, because the distance between the test apparatus and analyzer is small.

The reference and load specimens must be the same material and thickness. The load sample can be larger than the outer dimension of the holder, but the reference cannot be. The thickness is the most important dimension in shielding determination. For the most accurate and repeatable SE measurements, reference specimens and load samples should have the same thickness.

In Figure 77, the results of the improvement of 10dB by using the nickel nanoparticles synthesized by electrochemical discharges for EM shielding (deposited on carbon mesh) are shown. Integrating the particle production with the EM shielding of the composite would save on cost and increase the performance.

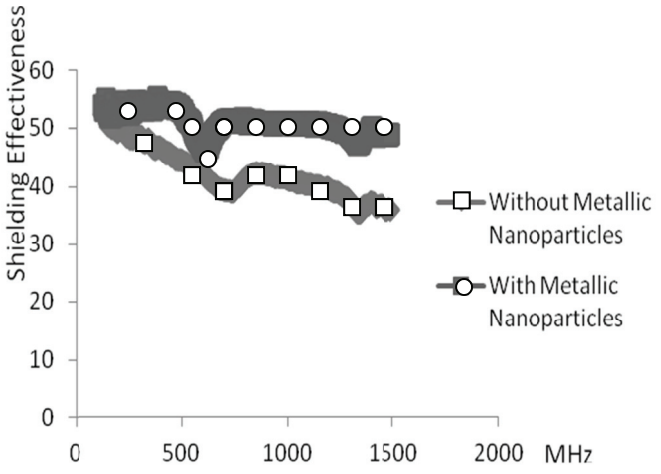

Figure 77 EM shielding effectiveness following ASTM 4935

Appendix B

Here, the estimation of particle volume fraction is presented.

Table 15 Complete data of particle volume fraction determination

	Iron										
particle size [nm]	20			40-60		40-60			60-80		
sample No.	2	4	1	1	2	1	4	2	3	2	4
weight [g]	2,91	2,89	2,78	4,36	2,33	2,99	2,85	2,94	2,74	2,78	2,73
volume [cm³]	2,15	2,09	2,10	1,89	0,98	2,23	2,11	2,13	2,03	2,09	2,04
vol. fract. of particles [%]	4,12	4,56	3,68	18,43	19,49	3,93	4,08	4,53	4,07	3,77	3,89
av. vol. fract. of particl. [%]	4,12			18,96		4,18			3,91		

	Fe3O4						Cobalt (ccp)			Pure Epoxy		
particle size [nm]	20-30			20-30			25-30			-		
sample No.	3	2	1	1	2	3	4	3	1	4	2	1
weight [g]	2,84	2,87	2,74	3,83	4,29	3,61	2,91	2,62	2,07	2,45	2,39	2,536
volume [cm³]	2,26	2,28	2,19	1,91	2,33	2,02	2,12	1,89	1,49	2,27	2,22	2,35
vol. fract. of particles [%]	4,43	4,48	4,29	23,06	18,96	17,63	3,83	4,01	4,04	1,01	-3,32	0,77
av. vol. fract. of particl. [%]	4,40			19,88			3,96			-0,51		

	Nickel											
particle size [nm]	20			<15			15			>15		
sample No.	3	2	1	1	5	2	5	4	2	5	2	1
weight [g]	2,63	2,57	2,71	2,71	2,59	2,97	2,86	2,83	2,85	2,74	2,94	2,51
volume [cm³]	1,91	1,88	1,94	1,96	1,86	2,12	2,08	2,03	2,05	1,97	2,09	1,83
vol. fract. of particles [%]	3,88	3,75	4,14	3,95	4,08	4,19	3,85	4,10	4,05	4,06	4,27	3,81
av. vol. fract. of particl. [%]	3,92			4,08			4,00			4,05		

Appendix C

Two kinds of nanoparticles (iron-nickel alloy and carbon-coated iron with an iron core and thin protection layer of carbon) are investigated. The size remains the same as conventional iron particles of 50nm. Iron-nickel nanoparticles, APTES, and iron coated nanoparticles are purchased from Sigma-Aldrich™. The rest of the chemicals are bought from Hexion™.

Here is the list of materials that are used for fabrication of samples with above particles:

- chloroform: used as a dispersing agent to ensure the spreading of the particles
- APTES (or 3-aminopropyl triethoxysilane), a coupling agent that is used to ensure a great blend between the particles and the resin
- EPIKURE 3046 as a curing agent, a hardener which reacts with the heat from the oven during the baking
- EPON resin 828RS which is the main component of the sample matrix

The above materials are mixed in an adequate mixture for fabrication of samples. For EM characterization, the samples should have the dimensions of 6cm x 4cm x 0.1cm (with volume of 2.4cm^3). Particle volume represents 4% of the sample volume, applied chloroform in a volume ration solvent/sample of 1/10 and employed APTES represents 1/10 of the nanoparticles weight. The weight of the epoxy resin has to be twice the

weight of the employed EPIKURE. The quantity of resin or EPIKURE is calculated by following equation:

$$V_t = V_{NPs} + V_{epo} + V_{cur} + V_{coup}$$

$$V_t - V_{NPs} - V_{coup} = (m_{epo}/d_{epo}) + (1/2) \times (m_{epo}/d_{cur})$$

$$M_{epo} = (V_t - V_{NPs} - V_{coup}) \times (2d_{cur} \times d_{epo}) / (2d_{cur} + d_{epo})$$

with V_t = *Total Volume* m_{epo} = *Epoxy weight*

V_{NPs} = *Nanoparticles volume* d_{epo} = *Epoxy density*

V_{epo} = *Epoxy volume* d_{cur} = *Curing agent density*

V_{cur} = *Curing agent volume* V_{coup} = *Coupling agent volume*

In the following tables, the densities of the used chemicals (in g/cm^3) as well as the quantities of the used chemical to manufacture the samples are given (all in gram).

Table 16 Densities of the quantities of materials for fabrication of nanocomposites

Iron-Nickel	Carbon coated Iron	Epoxy	EPIKURE	APTES	Chloroform
8.34	7.87	1.16	0.95	0.93	1.48

	Particles	Chloroform	APTES	Epoxy	EPIKURE
Iron-nickel	0.8g	0.36g	0.08g	1.6g	0.8g
Carbon coated	0.76g	0.36g	0.08g	1.62g	0.81g

Particles and chloroform are placed in a glass beaker. The mixture is positioned for 30s in an ultrasonic bath (a more effective method of stirring compared to mechanical, Figure 78).

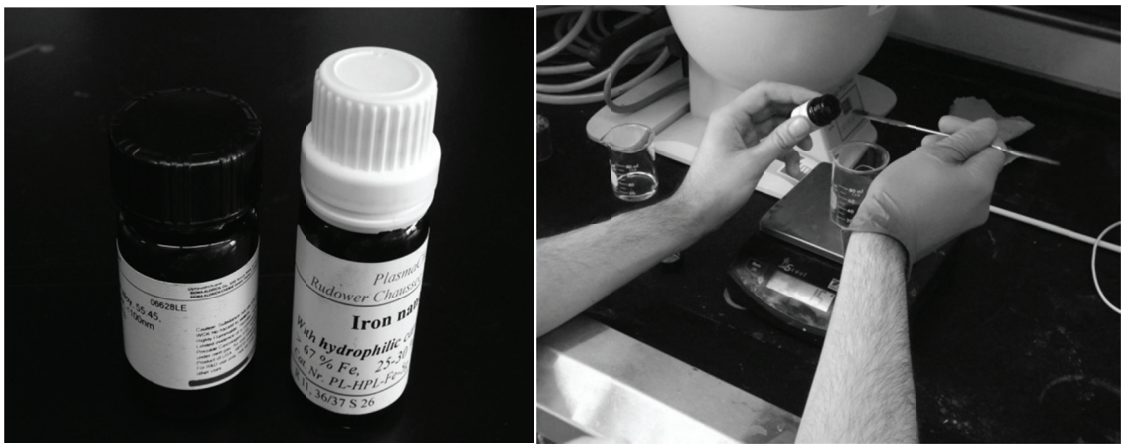

Figure 78 (left) Nickel-Iron particles and carbon coated Iron particles (right) manipulating the powder of metallic particles

The mixture is added to the coupling agent of APTES and the Epoxy resin (Figure 79). Due to the adhesive property of the resin, this new mixture is placed in a mechanical stirring at 700rpm for 10 minutes.

Figure 79 From left-to-right, APTES, Epoxy resin and Curing agent

In next step, the curing agent EPIKURE is added. The mixture undergoes another mechanical stirring for 10 minutes at 700rpm before being placed in an ultrasonic bath for 10 minutes (Figure 80).

Figure 80 (from left-to-right): Mechanical stirrer, Vacuum mixer, Mold containing samples

The mixture is transferred from the glass beaker to a plastic one. This new beaker is placed in a vacuum mixer which is a mixer allowing a great efficiency of blending and ensure the evaporation of the chloroform and the aspiration of the related gas. In the last step, the mixture is placed into the mold for approximately 24 hours in order to totally degas. After putting the mold into the oven, it is heated up from the room temperature to 80°C at a rate of 5°C/min. Once this temperature has been reached, the post curing process can operate for 2 hours. The temperature again immediately increases to 125°C for 3 hours (post curing process). After these 5 hours of baking, the mold can be released from the oven to be cooled before removing the samples with caution. It could be a great idea to put little weights on the edges of the mold to avoid the samples being curved when removing them from the oven. The results of both iron-nickel and iron particles with a coated layer of carbon are presented in Figure 81. The comparison with conventional particles of iron (with 50nm) is given in this figure. As the result, alloying

or using the coating layer does not improve the performance of particles in terms of electromagnetic absorption.

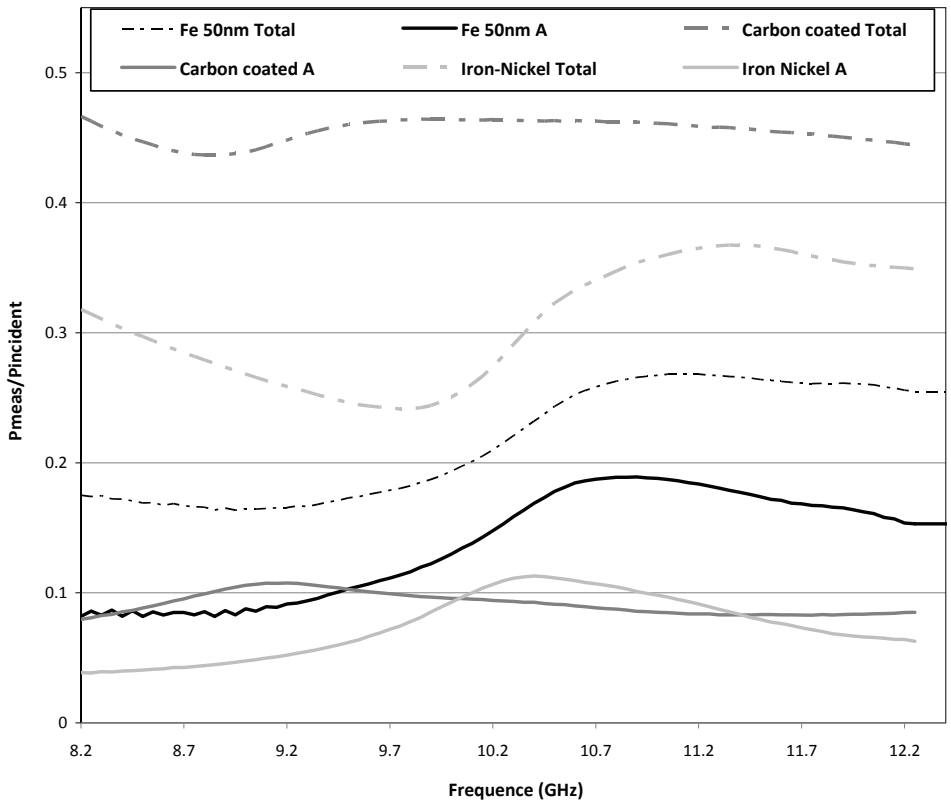

Figure 81 Comparison between the conventional 50nm of Iron particles with Iron-Nickel alloy and Iron with Carbon protection layer